EUSKAL HERRIKO UNIBERTSITATEA

eman ta zabal zazu



SOME ASPECTS OF TUNNELING SPECTROSCOPY AND ELECTRON AND PHOTON EMISSION IN SOLIDS

A thesis submitted to the University of the Basque Country to obtain the degree of Doctor in Physics

by

JOSE M. PITARKE DE LA TORRE

Leioa, July 1990

The investigation work constituting this thesis is partially published in the following publications:

- J.M. Pitarke, P.M. Echenique & R.H. Ritchie, *Electron density fluctuations induced by ion clusters in solids*, Nucl. Instrum. Methods B **40/41** 333-339 (1989),
- J.M. Pitarke, P.M. Echenique & F. Flores, *Apparent barrier height for tunneling electrons in STM*, Surf. Sci. **217** 267-275 (1989),
- J.M. Pitarke, F. Flores & P.M. Echenique, *Tunneling spectroscopy: Surface geometry and interface potential effects*, Surf. Sci. **234** 1-16 (1990),
- J.M. Pitarke, R.H. Ritchie & P.M. Echenique, *Radiative electron capture by channeled ions*, accepted for publication in Phys. Rev. B,
- J.M. Pitarke, P.M. Echenique & R.H. Ritchie, *Dependence of knock-on collision electron emission on the orientation of swift diclusters in solids*, to be published,
- J.M. Pitarke & P.M. Echenique, *Multiple scattering effects on electron emission by swift diclusters in solids*, to be published,

and in the following proceedings:

- J.M. Pitarke & P.M. Echenique, *Potential barrier for tunneling electrons in STM*, Proceedings of the 11th Werner Brandt Workshop on Penetration Phenomena of Charged Particles in Matter, Oak Ridge, Tennessee, April 14-15 (1988).
- J.M. Pitarke & R.H. Ritchie, *Radiative electron capture by channeled ions*, Proceedings of the 12th Werner Brandt Workshop on Penetration Phenomena of Charged Particles in Matter, Donostia, Basque Country, September 4-7 (1989).

I wish to express my gratitude to everyone who has helped me carrying out this work. I am especially indebted to:

Professor Pedro Miguel Etxenike, director of this work, for his expert direction thus introducing me in this field of investigation.

Professor Rufus Haynes Ritchie from the Oak Ridge National Laboratory and professor Fernando Flores from the Universidad Autónoma of Madrid, for giving to me the opportunity of discussing with them some of the results presented here.

Mr. Chris Nex from the Cavendish Laboratory, for his guidance with the numerical computations; without his help it would have been impossible to obtain some of the numerical results presented here.

Dr. Alberto Rivacoba and Dr. Juan M. Agirregabiria from the University of the Basque Country, for assistance with some of the computing required for the theoretical calculations.

The Department of Condensed Matter Physics of the University of the Basque Country, for leting me use their computer.

Dr. Jose Ramon Etxebarria from the University of the Basque Country, for his assistance in the preparation of the basque version of the manuscript.

Coworkers of the Department of Theoretical Physics and History of Science of the University of the Basque Country, for the very good atmosphere I have found working among them.

Professor Victor Ponce, for a very helpful and thorough reading of the manuscript.

CONTENTS

1. **Introduction** 1

2. **Tunneling microscope: tunneling spectroscopy** 7

2.1. Introduction 9

2.2. Tunneling current 14

WKB approximation 16

Mean barrier apprximation 17

Low-voltage range 19

High-voltage range 20

2.3. Transmission resonances 21

Image potential 28

Tunneling characteristics: s-V_a and dI/dV_a-V_a 32

2.4. Potential barrier: one-dimensional model 40

Parametrized potential barrier at a metal-vacuum-metal interface 41

Tunneling characteristics: s-V_a and dI/dV_a-V_a 46

2.5. Surface geometry: three-dimensional approach 50

Effective tunneling area 54

Tunneling characteristics: s-V_a and dI/dV_a-V_a 59

2.6. Apparent barrier height 64

General considerations 66

Mean barrier approximation 70

Exact results 76

References 84

3. **Interaction of swift diclusters with electrons in solids: knock-on electron emission** 91

3.1. Introduction 93

3.2. Electron density fluctuations 95

3.3. Scattering of electrons by swift diclusters penetrating matter:

perturbation theory approach 100

Second Born approximation 103

Initial momentum distribution of target valence electrons 110

3.4. Scattering of electrons by swift diclusters penetrating matter: non-perturbative approach 115

Appendix: Second order scattering amplitude for the potential (3.48) of a point charge 120

References 121

4. Radiative electron capture by channeled ions in solids 127

4.1. Introduction 129

4.2. REC probabilities 131

4.3. Capture of an electron from a bound state in the solid 135

Dipole approximation 136

4.4. Capture in the local density approximation 140

Plane waves 140

Coulombic waves 143

Statistical average 145

REC peak energies: Energy deficit 147

Full widths at half maximum and differential cross sections 151

Appendix: Derivation of eqs. (4.60) and (4.63) 155

References 158

5. Summary and conclusions 161

1. INTRODUCTION

One of the fundamental aims of Physics has been for many years to study the structure of matter and the individual and collective behaviour of particles constituting matter. In particular, the penetration of charged particles in matter has been one of the most important sources of information regarding the constitution of matter, and the need for interpretation of this kind of experiments has made necessary the theoretical knowledge regarding the interaction between charged particles and matter; indeed, the theoretical and experimental investigations of this problem have played a very important role in the development of modern physics and they have occupied the thoughts of some of the finest physicists of this century.

Rutherford in 1911 used alpha particles with the aim of learning from the structure of the atom, and Böhr in 1913 published a pioneering work calculating the stopping power of swift alpha particles penetrating matter. The next decade, together with the development of Quantum Mechanics, the quantum mechanical analysis of the interaction between charged particles and matter had already begun.

Since these pioneering works were developed, much theoretical and experimental work has been done regarding the interaction between ions with matter. In like manner, electrons have also been used as a source of information about the structure of matter, particularly since the invention of the electron microscope, the field emission and field ion microscope and the recently developed scanning tunneling microscope, which are all based on the particle-wave duality of matter predicted by Quantum Mechanics.

In this work some aspects of the interactions between charged particles and the electrons constituting the condensed matter are studied theoretically, and comparisons of our results with the available experimental data are made. With this purpose, we take the jellium model of the solid, that is, we treat the core of the atoms as a source of stationary positive charge background which is assumed to be uniform in density and to neutralize the negative charge of the outer electrons; therefore, there will be considered just the interactions between electrons of the solid. On the other hand, zero temperature will be considered, since the effects of room temperature on the results obtained here are negligible.

In chapter 2 the scanning tunneling microscopy experiments performed under constant conditions by other workers will be used, to study the interaction between electrons at metal

surfaces. In particular, we calculate the tunneling current between two metallic surfaces, the resonance fenomena appearing in the field emission regime is explained carefully, and then we are concerned with the theoretical calculation of the experimentally measured tunneling characteristics in order to estimate the shape of the potential barrier that electrons feel when they tunnel the vacuum region; this calculation is made for some one-dimensional models for the tip-sample interfaces, and then our full analysis of the three-dimensional models is presented, taking into account the tip-sample geometry. A theoretical analysis of the apparent barrier height at a metal-vacuum-metal interface is also presented.

Chapters 3 and 4 concern some aspects of the interactions caused by the passage of swift ions through matter. Many experiments have been performed to probe the wake potential and electronic polarization induced by the passage of fast charged particles; in particular, in a recently performed experiment knock-on collision electron emission from thin foils under bombardment by molecular swift ions has been mesured as a function of the orientation of the molecular axis of the projectile. Chapter 3 attemps to provide an interpretation of these experimental results; firstly, linear-response theory calculations of the density fluctuations at the position of the trailing ion are presented, as a function of the orientation of bombarding projectiles, and, secondly, the dependence of the knock-on collision electron yield caused by the passage of swift dimolecular ions through matter on the orientation of the moving clusters is studied theoretically, and the multiple scattering effects are approximated within the second Born approximation; then, the multiple scattering effects are studied using methods developed in the theory of low energy electron diffraction (LEED).

In chapter 4 the quantum theory of radiation is used to study processes involving the emission of photons accompanying electron capture by swift channeled ions in solids, and an interpretation of recent experimental data is presented, using a local density approximation.

In chapter 5 our conclusions are presented.

Unless otherwise stated, atomic units are used throughout. In this units system $\hbar = m_e = e^2 = 1$, where $\hbar$, m_e and e are the reduced Planck´s constant ($\hbar = h/2\pi$), the mass of the electron and the absolute value of its charge, respectively. The atomic unit of length is the Böhr radius, $a_0 = \hbar^2/m_e^2 = 0.529\text{Å}$, the atomic unit of energy is the Hartree, $1\text{Hartree} = e^2/a_0 =$

27.2eV, and the atomic unit of velocity, $v_0 = \alpha c = 2.19\text{x}10^8\ cm\ s^{-1}$, where α and c are the fine structure constant and the velocity of light, respectively.

2. TUNNELING MICROSCOPE: TUNNELING SPECTROSCOPY

2.1. Introduction

It is well known that according to Quantum Mechanics quantum objects can tunnel through classically forbidden regions of space where the particle potential energy exceeds its total energy. Therefore, elementary particles have non-zero probability of tunneling through potential barriers created by nuclear and atomic forces, as it has been shown experimentally.

Indeed, as soon as Schrödinger[1] had published his papers on Quantum Mechanics, Oppenheimer[2] and Gamow[3] used the quantum mechanical concept of tunneling to explain the autoionization of atomic hydrogen and the α particle decay process in heavy nuclei, respectively. In like manner, Fowler and Nordheim[4] explained the phenomenon of electron emission from cold metals upon the application of strong external electric fields; the invention of the field emission microscope[5] and the field-ion microscope[6] made this process a very useful experimental technique.

Since these pioneering studies, many devices have been designed using the capability of quantum objects to penetrate potential barriers. However, it has been necessary to wait for several years until vacuum barrier tunneling experiments have been performed[7-10]; finally, in 1981 Binnig and Rohrer developed methods of gently bringing a sharp tip up to a surface and controlling the tunneling current between them, and succeeded designing the scanning tunneling microscope (STM)[11-14], obtaining topographs of surfaces that showed atomic structure.

The potential barriers created by the nuclei in the interior of metals are quenched, as shown in fig. 2.1a, and valence electrons move freely in the conduction bands. At the surface the potential rises on the vacuum side forming the tunneling barrier; however, as this potential barrier is finite, the wave function of valence electrons extends into the vacuum, that is, electrons have a small but non-vanishing probability of being found just outside the metal surface. Now, if another metal is brought very close to the surface of the conducting material and an electrical voltage is applied between both metals, a tunneling current will flow across the gap between them, as shown in fig. 2.1b. Assuming that the electrodes are in equilibrium with each other, the Fermi levels of the two electrodes will be equal[15] and, thus, at zero

temperature it is necessary to apply a non-zero bias voltage between them, so as to provide empty states on the positively biased electrode for electrons tunneling from the negative electrode.

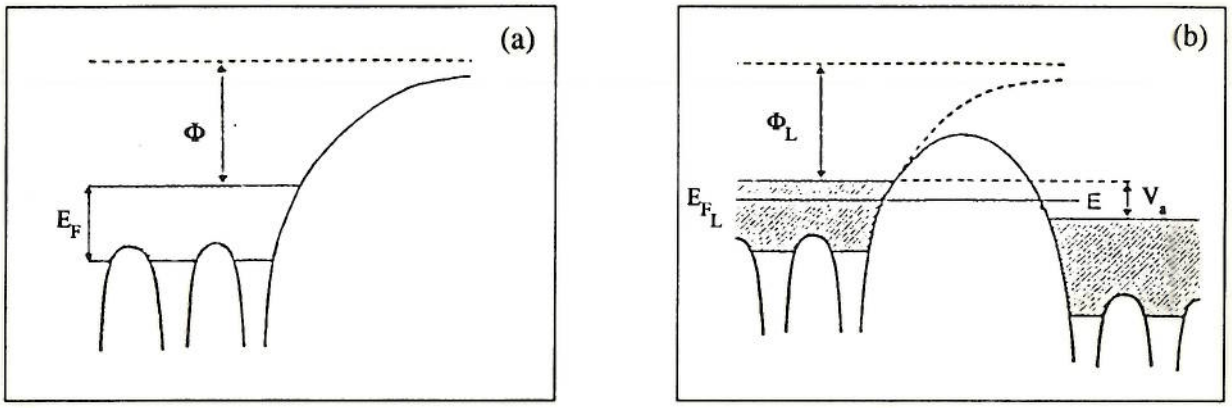


Fig. 2.1. a) Potential energy of electrons at a metallic surface; E_F and Φ represent the Fermi energy and the work function of the metal, respectively. b) Potential barrier at a metal-vacuum-metal interface; V_a represents the voltage applied between the metals, and E is the energy of a tunneling electron.

It is well known that the magnitude of the tunneling current is extremely sensitive to gap spacing; indeed, with work functions of a few electronvolts the tunneling current typically decreases by one order of magnitude for every angstrom of increase in gap spacing. Consequently, if a needle-like probe, the tip, is scanned across a sample while its distance from the surface is adjusted to keep a constant tunneling current, the recorded trajectory of the tip gives a topograph of the surface[16], as shown in fig. 2.2. Furthermore, the very high fields obtainable with vacuum tunneling at a few volts can be used to shape the tip as shown in fig. 2.3, and lateral atomic resolution may be achieved, since the tunneling effective area between sharp tips and the sample becomes very small.

In addition to the conventional use of the scanning tunneling microscope, that is, obtention of topographic images of surfaces with atomic resolution[17-19], it has been proved to be a useful tool to provide a measure of the barrier height that electrons see when tunneling between two solids and to obtain knowledge of the quantum mechanical interaction potential between tunneling electrons and surfaces, when the tip is displaced in the perpendicular direction to the surface keeping either I or V_a constant[20-24]. In particular, from the

experimental tunneling current or voltage dependence with the interelectrode separation the barrier height may be obtained as a function of separation[21-22].

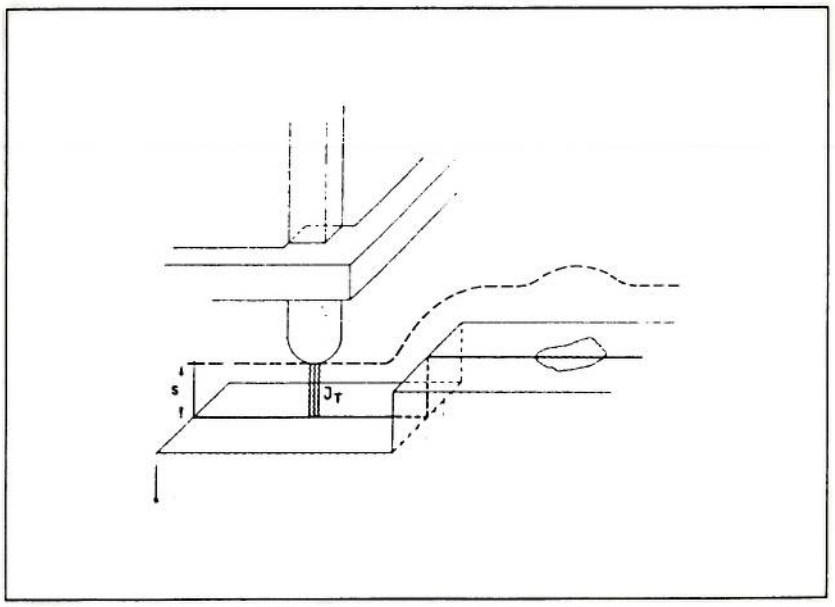


Fig. 2.2. Principle of operation of the scanning tunneling microscope (from ref. 13).

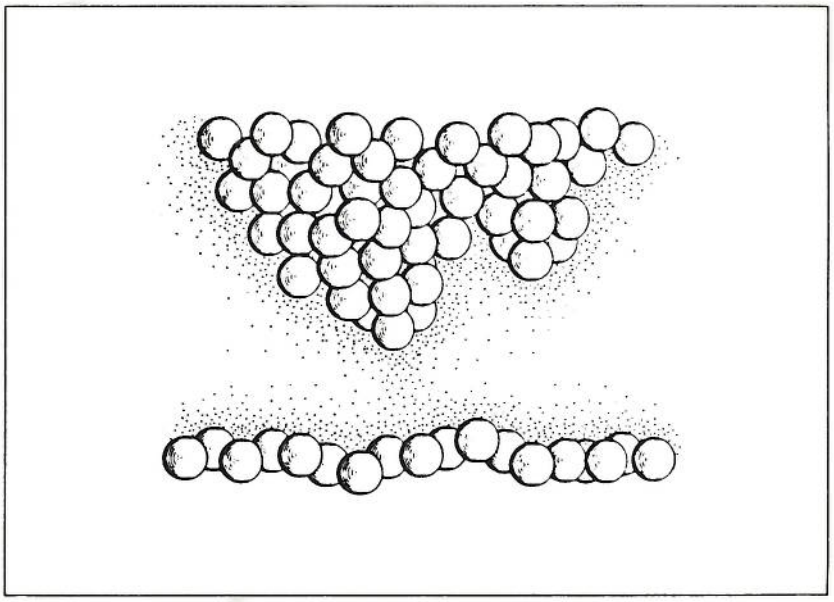


Fig. 2.3. Atoms of the tip and sample (from ref. 14).

When the applied voltage exceeds the work function of the positively biased electrode, as shown in fig. 2.4, electrons tunnel from filled states on the negative electrode into the vacuum

and are then accelerated in the positive kinetic-region into the positive electrode. For such high voltages the STM operates in the field emission mode, and the electron standing waves that are partially confined in the positive kinetic-energy region of the vacuum gap can be observed experimentally[24-27]. If this region were embedded in an infinitely high barrier, it would have bound levels, an these will broaden and turn into transmission resonances when the barrier is finite. Hence, as the voltage gets bigger additional resonant levels incorporate to the allowed energy region of tunneling electrons, and oscillations in the field emission current may be experimentally detected as bias is varied. On the other hand, the structure of these oscillations is very sensitive to the height and width of the barrier and also to its shape in the proximity of the positively biased surface, and resonant tunneling is, therefore, an obvious probe of surface potentials and the barrier that electrons feel when they tunnel a metal-vacuum-metal interface[28-30].

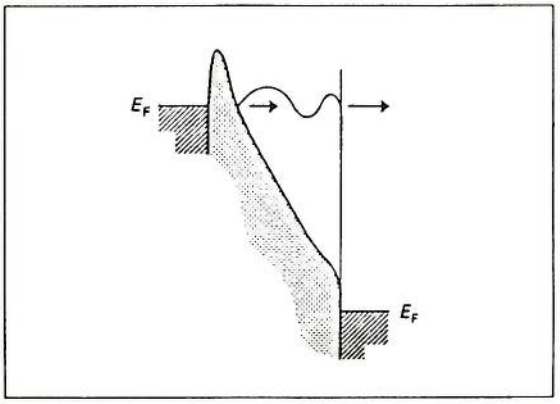


Fig. 2.4. Field emission tunneling into vacuum (from J. Gimzewski, Physics World **225** (1989)).

In section 2.2 the tunneling current between planar electrodes is derived very briefly, and the reliability of the still used WKB mean barrier approximations in calculating the current is critically examined; these are not original results, but, on the one hand, the formulas presented here are used through the whole chapter and, on the other hand, an understanding of the reliability of the mean barrier approximations is necessary to clarify the existing controversy about the contribution of the image potential to measurements of the apparent barrier height, as will be shown in section 2.6. In section 2.3 the origin of the experimentally observed

oscillations appearing in the constant current mode distance-voltage, s-V_a, and conductance-voltage, dI/dV_a-V_a characteristics is explained carefully. In section 2.4 a new 1-D model potential barrier consistent with recent theoretical work on the barrier potential which takes into account both local and non-local exchange and correlation effects is studied in detail[29-30]. In section 2.5 a 3-D analysis of the s-V_a and dI/dV_a-V_a characteristics is made and the radius of the tip is investigated[30]. In section 2.6 an analysis of the apparent barrier height in STM, defined in terms of the rate of change of the logarithm of the current or bias voltage with interelectrode separation, is made, as a function of separation, for different model potentials[31]; in particular, the existent controversy about the contribution of the image potential to measurements of the apparent barrier height is clarified and the role that the image potential plays in lowering the apparent barrier height is investigated. Finally, references are given.

2.2. Tunneling current

In order to calculate the tunneling current flowing across the gap between the tip and the sample constituting the scanning tunneling microscope, different approximate methods have been utilized. On the one hand, the transfer-hamiltonian formalism developed by Bardeen[32] has been used[33-37], especially for small voltages; in this approach tunneling is viewed as resulting from transitions between weakly overlapping unperturbed states of the two electrodes, and the tunneling current is calculated by first-order perturbation theory. Lang[38-40] has used similar methods to calculate the tunneling current in terms of the wave functions determined self-consistently for each electrode. On the other hand, tunneling currents have been calculated in the free electron gas approximation by solving the Schrödinger equation for the tip-sample interface[41-43]. Here we are interested in deducing from experimental data the shape of the surface potential, so that tunneling currents will be calculated following a free electron gas approximation.

In this section an independent-electron model of the electrodes is used and two metallic semi-infinite electrodes, L and R, with planar and parallel surfaces separated by vacuum are considered. z axis is taken to be perpendicular to both surfaces, with the L electrode occupying the $z \leq 0$ half-space.

Neglecting the interactions between tunneling electrons, the total tunneling current density is just the sum of the current density contributions from each electronic state of the metal-vacuum-metal system; therefore, accounting for the additional states produced by the two electron spin orientations, the current density flowing from L to R is given by

$$J_{L \rightarrow R} = 2 \sum_{\boldsymbol{k}} J_z(\boldsymbol{k}) \left[f(E) - f(E+V_a) \right] \quad , \tag{2.1}$$

when a positive polarity voltage is connected to electrode R. In this expression, $J_z(\boldsymbol{k})$ is the z component of the current density of electrons with momentum $\boldsymbol{k}$:

$$J_z(\boldsymbol{k}) = \frac{1}{V} D(E_z)\, k_z \quad , \tag{2.2}$$

where V is the normalization volume of the system, and $D(E_z)$, the transmission probability of

electrons with energy E_z, which may be obtained solving the one-dimensional time-independent Schrödinger equation[44]. We define E_z as the z component of the incident electron energy

$$E_z = \frac{1}{2} k_z^2 + U_L \ , \tag{2.3}$$

U_L being the bulk inner potential of the electrode L, and $f(E)$ is the Fermi-Dirac distribution

$$f(E) = \left[1 + \exp\left(\frac{E - E_F}{k_B T} \right) \right]^{-1} \ , \tag{2.4}$$

where E is the energy of the electron, E_F is the Fermi energy, k_B is Boltzman´s constant and T is the system temperature.

The volume of $\boldsymbol{k}$-space per allowed $\boldsymbol{k}$ value is $\Delta \boldsymbol{k} = (2\pi)^3/V$, so that in the limit as $\Delta \boldsymbol{k} \rightarrow 0$, i.e. $V \rightarrow \infty$, (2.1) may be rewritten as

$$J_{L \rightarrow R} = \int_{U_L}^{\infty} dE_z \, n(E_z) \, D(E_z) \ , \tag{2.5}$$

where $dE_z \, n(E_z)$ is the number of electrons crossing the surface of electrode L per unit area and unit time with the energy component in the z direction between E_z and $E_z + dE_z$, and

$$n(E_z) = \frac{1}{2\pi^2} \int_0^{\infty} dE_{\parallel} \left[f(E) - f(E + V_a) \right] \ . \tag{2.6}$$

$E_{\parallel}$ is the energy component of the incident electron in the plane perpendicular to the z axis,

$$E_{\parallel} = \frac{1}{2} \left(\boldsymbol{k} - k_z \, \boldsymbol{z} \right)^2 , \tag{2.7}$$

$\boldsymbol{z}$ being a unit vector normal to the surfaces of the electrodes.

At a temperature of 0°K, $n(E_z)$ is given by (see fig. 2.5)

$$n(E_z) = \begin{cases} \dfrac{1}{2\pi^2} V_a & , U_L \le E_z \le -\Phi_L - V_a \\ \dfrac{1}{2\pi^2} (-\Phi_L - E_z) & , -\Phi_L - V_a \le E_z \le -\Phi_L \\ 0 & , -\Phi_L \le E_z \ , \end{cases} \tag{2.8}$$

and, hence[45,46],

$$J = \frac{1}{2\pi^2}\left[V_a \int_{U_L}^{-\Phi_L - V_a} dE_z\, D(E_z) + \int_{-\Phi_L - V_a}^{-\Phi_L} dE_z\, (-\Phi_L - E_z)\, D(E_z) \right], \tag{2.9}$$

where energies are referenced to the vacuum level of the negatively biased electrode, electrode L, and Φ_L represents the work function of that electrode. Let us point out that the effect of tenperature in typical STM experiments is negligible[10].

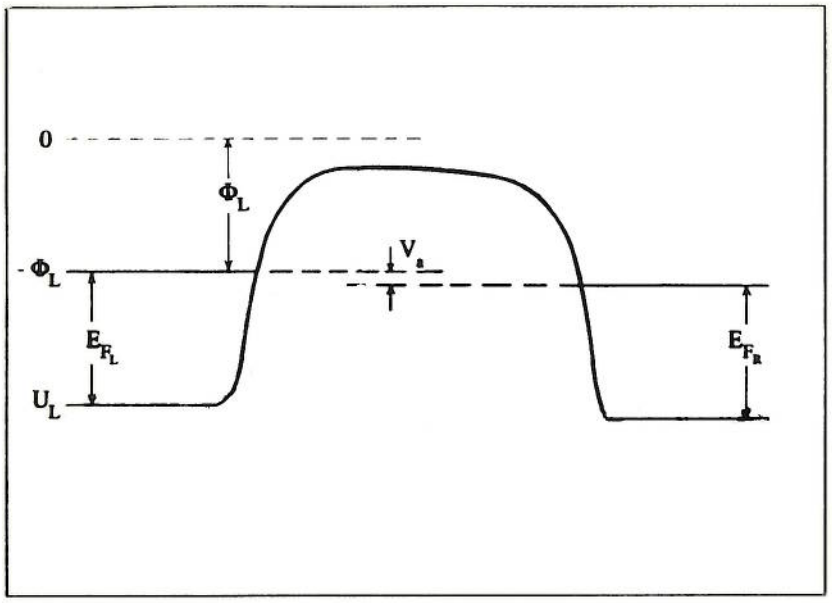


Fig. 2.5. Energy diagram for electrons tunneling a metal-vacuum-metal interface.

WKB approximation

If the Wentzel-Kramers-Brillouin (WKB) approximation for calculating transmission probabilities is used, we have the well-known formula[47]:

$$D(E_z) = \exp\left\{ -2\sqrt{2} \int_{s_1(E_z)}^{s_2(E_z)} dz \left[-\Phi_L + \varphi(z) - E_z \right]^{1/2} \right\}, \tag{2.10}$$

where $\varphi(z)$ represents the potential barrier height referenced to the Fermi level of the negatively

biased electrode, and $s_1(E_z)$ and $s_2(E_z)$ are the classical turning points at the energy E_z.

Integrating eq. (2.10) yields[45]

$$D(E_z) = \exp\left[-\alpha(E_z)\,(-\Phi_L + \bar{\Phi}(E_z) - E_z)^{1/2}\right] \quad . \tag{2.11}$$

In this expression,

$$\alpha(E_z) = 2\sqrt{2}\,\beta(E_z)\,\Delta s(E_z) \quad , \tag{2.12}$$

where

$$\beta(E_z) = 1 - \frac{1}{\Delta s(E_z)} \int_{s_1(E_z)}^{s_2(E_z)} dz\, \frac{1}{8} \left(\frac{\varphi(z) - \bar{\Phi}(E_z)}{-\Phi_L + \bar{\Phi}(E_z) - E_z} \right)^2 , \tag{2.13}$$

neglecting third order and higher order terms, and

$$\Delta s(E_z) = s_2(E_z) - s_1(E_z) \tag{2.14}$$

and

$$\bar{\Phi}(E_z) = \frac{1}{\Delta s(E_z)} \int_{s_1(E_z)}^{s_2(E_z)} dz\, \varphi(z) \quad . \tag{2.15}$$

Mean barrier approximation

Frequently, neglecting the dependence of (2.12) and (2.15) on E_z, the mean barrier approximation, MBA, is used to calculate transmission probabilities[45,48]:

$$D(E_z) = \exp\left[-\alpha\,(-\Phi_L + \bar{\Phi} - E_z)^{1/2}\right] , \tag{2.16}$$

where

$$\alpha = \alpha(-\Phi_L) = 2\sqrt{2}\;\beta(-\Phi_L)\,\Delta s(-\Phi_L) \quad , \tag{2.17}$$

and $\bar{\Phi}$, the mean barrier height above the Fermi level of the negatively biased electrode, is

$$\bar{\Phi} = \bar{\Phi}(-\Phi_L) = \frac{1}{\Delta s(-\Phi_L)} \int_{s_1(-\Phi_L)}^{s_2(-\Phi_L)} dz\, \varphi(z) \quad . \tag{2.18}$$

However, for interelectrode separations of interest in STM the dependence of $\alpha(E_z)$ and $\bar{\Phi}(E_z)$ on E_z is not negligible at all, unless the potential barrier is trapezoidal in shape, and, hence, the mean barrier approximation is not always reliable. As a matter of fact, for small separations ($s \lesssim 10\text{Å}$) this approximation overestimates the tunneling current density, as already pointed out by Miskovsky et al[49].

Substituting eq. (2.16) into eq. (2.9) and integrating gives

$$J = \frac{2}{\pi^2 \alpha^2} \left\{ \bar{\Phi} \left[1 + 3\,\alpha^{-1} \bar{\Phi}^{-1/2} + 3\,\alpha^{-2} \bar{\Phi}^{-1} \right] e^{-\alpha \bar{\Phi}^{1/2}} \right.$$

$$- (\bar{\Phi} + V_a) \left[1 + 3\,\alpha^{-1} (\bar{\Phi} + V_a)^{-1/2} + 3\,\alpha^{-2} (\bar{\Phi} + V_a)^{-1} \right] e^{-\alpha (\bar{\Phi} + V_a)^{1/2}}$$

$$\left. - \frac{1}{2} V_a \left[1 + \alpha (\bar{\Phi} + E_F)^{1/2} \right] e^{-\alpha (\bar{\Phi} + E_F)^{1/2}} \right\} , \qquad (2.19)$$

where E_F is the Fermi energy of the negatively biased electrode. For typical Fermi energies and work functions, the last term in braces is negligible compared to the first and second terms whenever $s \gtrsim 5\text{Å}$; thus, eq. (2.19) reduces to

$$J_M = \frac{2}{\pi^2 \alpha^2} \left\{ \bar{\Phi} \left[1 + 3\,\alpha^{-1} \bar{\Phi}^{-1/2} + 3\,\alpha^{-2} \bar{\Phi}^{-1} \right] e^{-\alpha \bar{\Phi}^{1/2}} \right.$$

$$\left. - (\bar{\Phi} + V_a) \left[1 + 3\,\alpha^{-1} (\bar{\Phi} + V_a)^{-1/2} + 3\,\alpha^{-2} (\bar{\Phi} + V_a)^{-1} \right] e^{-\alpha (\bar{\Phi} + V_a)^{1/2}} \right\} . \qquad (2.20)$$

Simmons, assuming that $\alpha \bar{\Phi}^{1/2} >> 1$ and $\alpha (\bar{\Phi} + V_a)^{1/2} >> 1$ suggested the following further approximation of the tunneling current density[45]:

$$J_S = \frac{2}{\pi^2 \alpha^2} \left\{ \bar{\Phi} e^{-\alpha \bar{\Phi}^{1/2}} - (\bar{\Phi} + V_a) e^{-\alpha (\bar{\Phi} + V_a)^{1/2}} \right\} ; \qquad (2.21)$$

we refer to this latter approximation as the Simmons mean barrier approximation, SBA. For typical metallic work functions of a few electronvolts, the inequalities leading to this approximation begin to fail for interelectrode separations of less than about 20Å, and the SBA approximation underestimates the tunneling current density[49].

Consequently, it is of great interest to emphasize that the continued use of the mean barrier approximations in STM can lead to serious errors in the interpretation of the

experimental results, as will be shown in section 2.6. For interelectrode separations of more than about 10Å, the application of the MBA approximation is justified, but for smaller separations eq. (2.9) should be integrated numerically after having substituted the transmission probabilities.

Low-voltage range

For very low voltages, eq. (2.20) may be rewritten as

$$J_M = \frac{2}{\pi^2 \alpha^2} \left\{ \bar{\Phi} \left[1 + 3\,\alpha^{-1} \bar{\Phi}^{-1/2} + 3\,\alpha^{-2} \bar{\Phi}^{-1} \right] \right.$$

$$\left. - (\bar{\Phi} + V_a) \left[1 + 3\,\alpha^{-1} (\bar{\Phi} + V_a)^{-1/2} + 3\,\alpha^{-2} (\bar{\Phi} + V_a)^{-1} \right] e^{-1/2\,\alpha V_a \bar{\Phi}^{-1/2}} \right\} e^{-\alpha \bar{\Phi}^{1/2}} . \quad (2.22)$$

Expanding in this expression $\exp(-1/2\,\alpha V_a\,\bar{\Phi}^{-1/2})$, and neglecting second order and higher order terms, eq. (2.22) becomes

$$J_M = \frac{1}{\pi^2 \alpha} \bar{\Phi}^{1/2} V_a \left[1 + (\alpha \bar{\Phi}^{1/2})^{-1} \right] e^{-\alpha \bar{\Phi}^{1/2}} . \quad (2.23)$$

Alternatively, for vey low voltages eq. (2.21) becomes

$$J_S = \frac{1}{\pi^2 \alpha} \bar{\Phi}^{1/2} V_a \left[1 - 2\,(\alpha\,\bar{\Phi}^{1/2})^{-1} \right] e^{-\alpha \bar{\Phi}^{1/2}} , \quad (2.24)$$

and assuming again that $\alpha\,\bar{\Phi}^{1/2} >> 1$, we have

$$J_S = \frac{1}{\pi^2 \alpha} \bar{\Phi} V_a\, e^{-\alpha \bar{\Phi}^{1/2}} . \quad (2.25)$$

On the other hand, the effective potential barrier may be defined as

$$\Phi_e^{1/2} = \frac{1}{\Delta s} \int_{s_1}^{s_2} dz\, \varphi^{1/2}(z) , \quad (2.26)$$

where

$$s_1 = s_1\,(-\Phi_L) , \quad (2.27)$$

$$s_2 = s_2(-\Phi_L) \tag{2.28}$$

and

$$\Delta s = s_2 - s_1 \quad . \tag{2.29}$$

Thus, eq. (2.23) may be rewritten in the following way:

$$J_M = \frac{1}{\pi^2 \alpha_0 \beta^2} \, \Phi_e^{1/2} \left[1 + (\alpha_0 \Phi_e^{1/2})^{-1} \right] e^{-\alpha_0 \Phi_e^{1/2}} , \tag{2.30}$$

where

$$\beta = \beta(-\Phi_L) \tag{2.31}$$

and

$$\alpha_0 = 2\sqrt{2} \, \Delta s \quad , \tag{2.32}$$

since

$$\int_{s_1}^{s_2} dz \, \varphi^{1/2}(z) = \beta \, \bar{\Phi}^{1/2} \, \Delta s \quad . \tag{2.33}$$

High-voltage range

For high voltages ($V_a > \Phi_R$), eq. (2.20) may be written as

$$J_M = \frac{2}{\pi^2 \alpha^2} \bar{\Phi} \left[1 + 3 (\alpha \bar{\Phi}^{1/2})^{-1} + 3 (\alpha \bar{\Phi}^{1/2})^{-2} \right] e^{-\alpha \bar{\Phi}^{1/2}} , \tag{2.34}$$

or, in terms of the effective potential barrier of eq. (2.26):

$$J_M = \frac{2}{\pi^2 \alpha_0^2 \beta^4} \Phi_e \left[1 + 3 (\alpha_0 \Phi_e^{1/2})^{-1} + 3 (\alpha_0 \Phi_e^{1/2})^{-2} \right] e^{-\alpha_0 \Phi_e^{1/2}} . \tag{2.35}$$

2.3. Transmission resonances

In this section and the following one two planar and parallel electrodes will be considered, as in the preceding section, and we will restrict to the case in which a voltage of a few volts is applied between both electrodes. In particular, when the applied voltage is greater than the work function of the positively biased electrode, field emission occurs and electrons tunnel from filled states on the negatively biased electrodes into vacuum and are then accelerated in the electric field between both electrodes into the positively biased electrode, as shown in fig. 2.4 in the introduction, and transmission resonances originate.

With the aim of clarifying the origin of transmission resonances and their relationship with the oscillations in the constant current mode conductance-voltage characteristics observed in STM experiments, let us consider the infinite potential barrier shown in fig. 2.6a:

$$V(z) = \begin{cases} F\,z & , z \le s \\ \infty & , s < z \end{cases} , \tag{2.36}$$

where F represents the slope of the barrier.

The time-independent Schrödinger equation of electrons in this barrier may be written, when $z \le s$, as

$$\psi''(z) + 2\left[E - F\,z\right]\psi(z) = 0 , \tag{2.37}$$

where E is the energy of the electron. The substitution

$$u = (2F^{-2})^{1/3}(F\,z - E) \tag{2.38}$$

in eq. (2.37) leads to the following equation:

$$\psi''(u) - u\,\psi(u) = 0 . \tag{2.39}$$

Two linearly independent solutions of the differential equation (2.39) are the Airy functions $Ai(u)$ and $Bi(u)$[50]; consequently, we have

$$\psi(z) = A\,Ai\left[(2F^{-2})^{1/3}(F\,z - E)\right] + B\,Bi\left[(2F^{-2})^{1/3}(F\,z - E)\right] , \tag{2.40}$$

where A and B are constants. Application of the boundary conditions leads to quantization of the energy, with the following sequence of discrete energy levels, referenced to the bottom of the barrier:

$$E_n = -(2F^{-2})^{-1/3} a_n \ , \tag{2.41}$$

corresponding to all positive integer values of the quantum number n. The quantities a_n are the zeros of the Ai Airy function:

$$a_n = -f\left[\frac{3\pi}{2}\left(n-\frac{1}{4}\right)\right], \tag{2.42}$$

and the asymptotic expansion of the function $f(x)$ is

$$f(x) = x^{2/3}\left(1+\frac{5}{48}x^{-2}-\frac{5}{36}x^{-4}+\frac{77125}{82944}x^{-6}+O(x^{-8})\right) . \tag{2.43}$$

The first three bound levels given by eq. (2.41) are represented in fig. 2.6a by dotted horizontal lines.

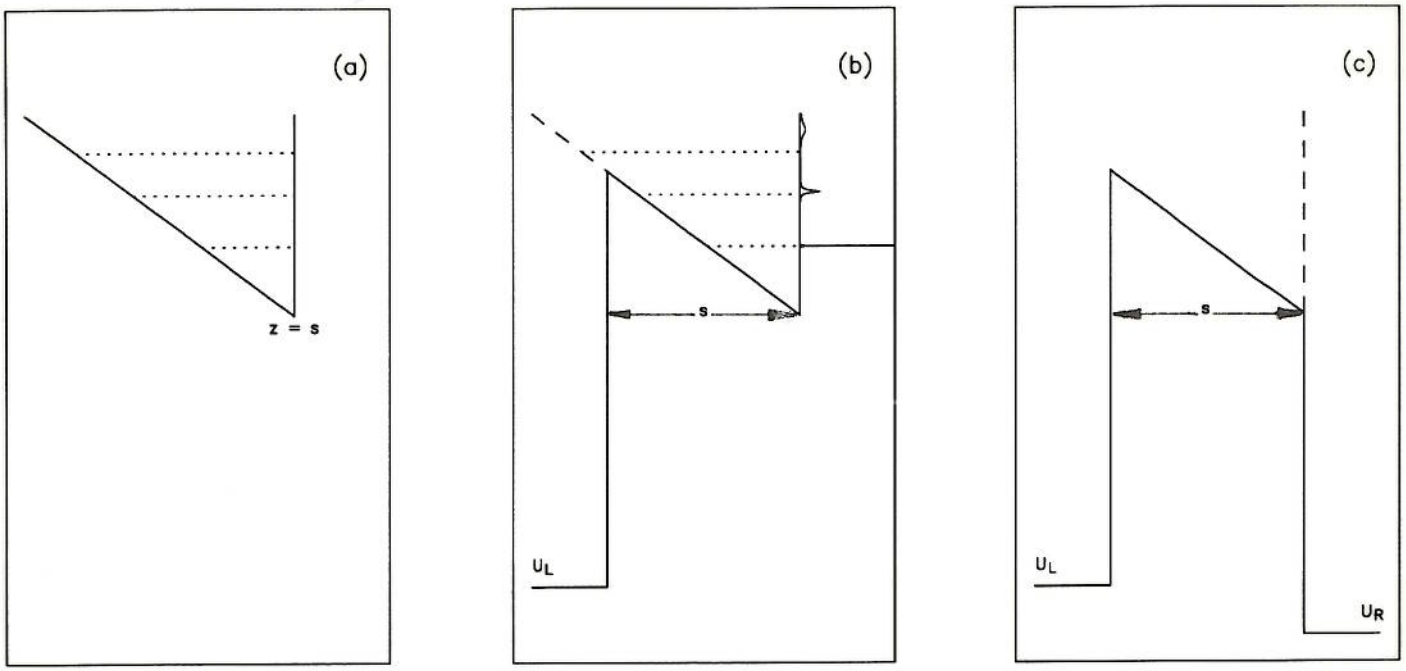


Fig. 2.6. Potential barriers: a) Infinite barrier, b) semi-infinite barrier, and c) trapezoidal barrier. In figs. 2.6a and 2.6b the bound energy levels of eq. (2.41) are shown (dotted horizontal lines), and inf fig. 2.6b the square amplitude of eq. (2.45) is also shown (solid curve).

When one of the wells of the barrier is finite, as shown in fig. 26b, the electronic waves are not completely confined in the positive-kinetic energy region. Solving the corresponding Schrödinger equation and applying the boundary conditions yield the following expression for

the electronic wave function in the sloped region of the barrier:

$$\psi(z) = A\, g\left[-(2F^{-2})^{1/3} (F z - E) \right] \quad (0 \le z \le s) \ , \tag{2.44}$$

where

$$A^2 = \frac{(2k_L)^2 \left[Ai^2(u_s) + Bi^2(u_s) \right]}{u'^2 \left[Ai'(u_0)\, Bi(u_s) - Ai(u_s)\, Bi'(u_0) \right]^2 + k_L^2 \left[Ai(u_0)\, Bi(u_s) - Ai(u_s)\, Bi(u_0) \right]^2} \tag{2.45}$$

and

$$g(x) = \sqrt{Ai^2(-x) + Bi^2(-x)}\ \sin\left[\tan^{-1}\frac{Bi(-x)}{Ai(-x)} + \tan^{-1}\frac{-Bi(u_s)}{Ai(u_s)} \right] \tag{2.46}$$

In these expressions,

$$u_0 = -(2F^{-2})^{1/3} E \ , \tag{2.47}$$

$$u_s = (2F^{-2})^{1/3} (F s - E) \ , \tag{2.48}$$

$$u' = (2F^{-2})^{1/3} F \tag{2.49}$$

and

$$k_L = \sqrt{2(E - U_L)} \ , \tag{2.50}$$

s and U_L being the parameters shown in fig. 2.6b.The square of the amplitude given by eq. (2.45) is shown as a function of energy in fig. 2.6b, together with the bound levels of the infinite barrier.

The simplest approximation to the potential barrier at a metal-vacuum-metal interface is the trapezoidal barrier shown in fig. 2.6c:

$$V(z) = \begin{cases} U_L & , \ z \le 0 \\ -(V_a + \Delta\Phi)\dfrac{z}{s} & , \ 0 \le z \le s \\ U_R & , \ s \le z \ , \end{cases} \tag{2.51}$$

referenced to the vacuum level of the electrode L, which occupies the $z \le 0$ half-space; U_L and U_R represent the bulk inner potentials of electrodes L and R, respectively, V_a is the applied voltage and $\Delta\Phi$ is the difference between work functions

$$\Delta\Phi = \Phi_L - \Phi_R \ . \tag{2.52}$$

For the barriers shown in figs. 2.6b and 2.6c non negligible amplitudes of the wave function are achieved only for energies close to the bound levels of the infinite barrier (see fig. 2.6b), because of the interference between incident and reflected electrons in the positive kinetic-energy region of the vacuum gap; hence, the originally bound levels will broaden and turn into transmission resonances when the well is embedded in the trapezoidal barrier shown in fig. 2.6c.

However, it is well known that the WKB approximation, the conventional method used to calculate the transmission coefficient across potential barriers, fails to explain the resonance fenomena[51], because the effect of the partially reflecting interface at $z = s$ is neglected. Consequently, in order to explain this phenomenon, it is necessary to solve the Schrödinger equation through the interface potential barrier. In particular, the transmission probabilities for the trapezoidal barrier can be calculated analytically by connecting the Airy functions, exact solutions of the Schrödinger equation trhough this barrier, and their derivatives at $z = 0$ and $z = s$ [52]:

$$D = \frac{k_R}{k_L} \frac{4/\pi^2}{\alpha^2+\beta^2}, \tag{2.53}$$

where

$$k_L = \sqrt{2\,(E - U_L)} \tag{2.54}$$

and

$$k_R = \sqrt{2\,(E - U_R)}\ , \tag{2.55}$$

and α and β are the following constants:

$$\alpha = k_R \left[Ai(u_0)\, Bi(u_s) - Ai(u_s)\, Bi(u_0) \right] / u' + k_L^{-1} \left[Ai'(u_0)\, Bi(u_s) - Ai'(u_s)\, Bi'(u_0) \right] u' \tag{2.56}$$

and

$$\beta = \frac{k_R}{k_L} \left[Ai(u_s)\, Bi'(u_0) - Ai'(u_0)\, Bi(u_s) \right] + \left[Ai(u_0)\, Bi'(u_s) - Ai'(u_s)\, Bi(u_0) \right] . \tag{2.57}$$

In these expressions, u_0, u_s and u' are given by eqs. (2.47), (2.48) and (2.49), respectively, and F represents the electric field between the electrodes:

$$F = -\frac{V_a + \Delta\Phi}{s} \quad . \tag{2.58}$$

Fig. 2.7 exhibits the square amplitude of the wave function of electrons in the semi-infinite barrier and, also, the transmission probability of eq. (2.53), as a function of energy, when U_L = -12.68eV, U_R = -9.8eV, V_a = 4V, s = 10Å and F = -0.438eV/Å, together with the bound levels of the infinite barrier.

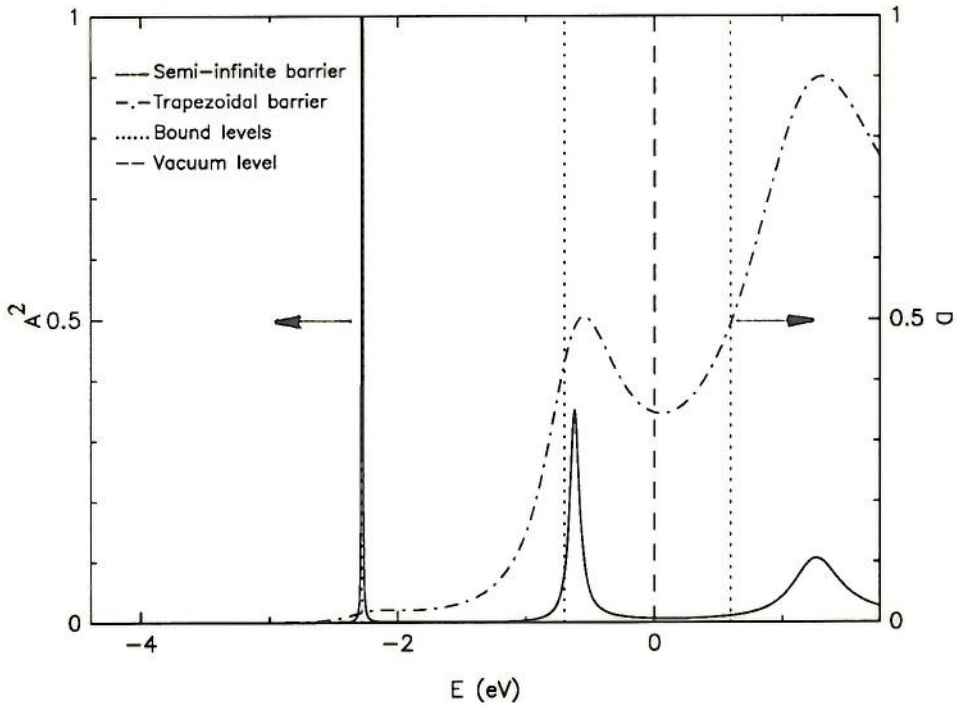


Fig. 2.7. Square amplitude of the electronic wave function corresponding to the semi-infinite barrier, as shown in fig. 2.6b, and transmission probability of electrons tunneling the trapezoidal finite barrier, as a function of energy. The bound energy levels (dotted vertical lines) of the infinite barrier and the vacuum level of the negatively biased electrode (dashed vertical line) are also shown. U_L = -12.68eV, U_R = -9.8eV, V_a = 4V, s = 10Å and F = -0.438eV/Å.

It is obvious from this figure that the peak energy positions of the amplitudes of electrons in the semi-infinite barrier coincide with the transmission resonances of electrons tunneling the trapezoidal finite barrier. The first peak energy position coincides, also, with the first bound level of the infinite barrier; however, the second and third peak energy positions differ from

the bound levels, since they are not well below the vacuum level of the negatively biased electrode, which is represented in fig. 2.7 by a dashed vertical line.

In fig. 2.8 the evolution of the peak energy positions in the transmission probability of electrons tunneling the trapezoidal barrier are shown, as a function of s, when $V_a = 0$ (fig. 2.8a), and, as a function of V_a, when $s = 20$Å (fig. 2.8b), together with the evolution of the bound levels of the infinite barrier. Notice that the energy positions of the transmission resonances for the finite barrier only differ from the bound levels when the energy is not well below the vacuum level of the negatively biased electrode, so that in the range of energies we are concerned with in STM experiments both positions exactly coincide.

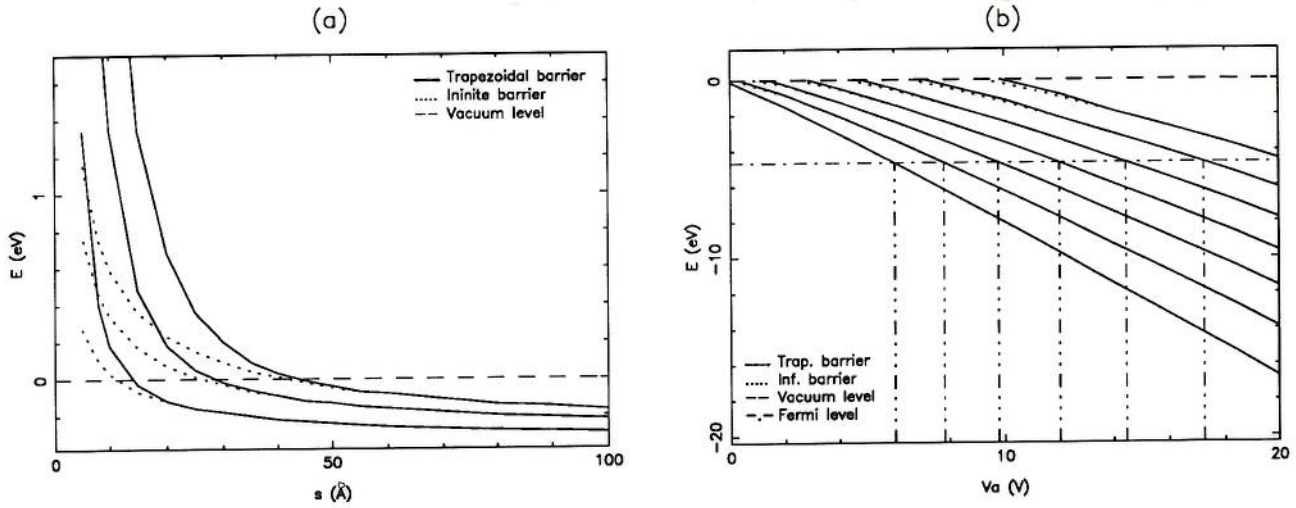


Fig. 2.8. Evolution of the peak energies in the transmission probability of electrons tunneling the trapezoidal barrier (solid curves) and the bound energy levels of the infinite barrier (dashed curves), as a function of tip-sample distance at $V_a = 0$ (fig. 2.8a), and as a function of applied voltage at $s = 20$Å (fig. 2.8b). In fig. 2.8b the values that the applied voltage has each time an additional resonant level incorporates to the allowed energy region of tunneling electrons are also represented (vertical dashed-dotted-dotted-dotted lines). In these calculations the following values of the work functions have been considered: $\Phi_L = 4.68$eV and $\Phi_R = 4.3$eV.

Transmission resonances can be experimentally observed whenever resonant levels are situated below the Fermi level of the negatively biased electrode, so that voltage must be greater than the work function of the positive electrode. Thus as the applied voltage increases maxima in the transmission probability of Fermi electrons will appear each time an additional resonant level crosses the Fermi level of the negatively biased electrode; the values of the bias

voltage for which an additional resonant level incorporates to the allowed energy region are represented in fig. 2.8b by vertical lines.

The difference between consecutive resonance energies is proportional to $F^{2/3}$; hence, it gets greater as the applied voltage increases in the constant interelectrode separation mode and the increase in the applied voltage necessary for an additional resonant level to incorporate gets greater, too, which is obvious from fig. 2.8b. Instead, if the interelectrode separation were increased as the same time as the applied voltage, keeping the electric field F constant, the increase in the applied voltage necessary for an additional resonant level to incorporate would not get greater as the applied voltage increases; moreover, it would get slightly smaller, as fig. 2.9 shows, since for a given value of F the difference between consecutive resonant energies gets smaller as n increases. Fig. 2.9 shows the evolution of the bound levels of the infinite barrier, as a function of V_a, when the inerelectrode separation is increased as the same time as V_a in order to keep the electric field constant.

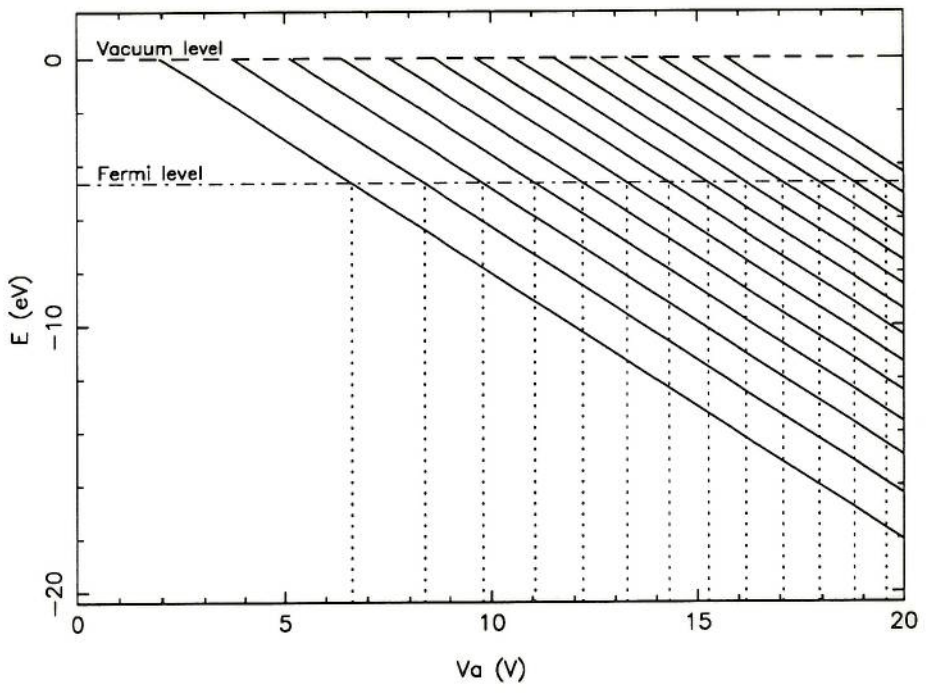


Fig. 2.9. Evolution of the bound energy levels of eq. (2.41) in the constant electric field mode for F = -0.438eV/Å, versus applied voltage. For energies below the Fermi level of the negatively bias electrode resonances of the trapezoidal barrier exactly coincide with the bound energy levels of the infinite barrier. The vertical dotted lines represent the values that the applied voltage has when an additional resonant level incorporates to the allowed energy region of tunneling electrons, as in fig. 2.8b.

Next we go a step further in the approximation for the potential barrier at a metal-vacuum-metal interface, including the contribution due to the classical image force from the electrodes, and we study the role that the image potential plays modifying the structure of the transmission resonances.

Image potential

Let us consider a point charge q located at a distance z from a conducting plane, as shown in fig. 10. The electric force acting on this charge produced by the charges induced on the conducting plane is equal to the electric force produced by an image charge $-q$ located at the same distance z at the other side of the plane [53] (see fig. 2.10a):

$$F_{\text{im}}(z) = -\frac{q^2}{(2z)^2} z \ , \tag{2.59}$$

z being a unit vector normal to the plane, and the potential energy of the point charge q is

$$V_{\text{im}}(z) = -\frac{q^2}{4z} \ . \tag{2.60}$$

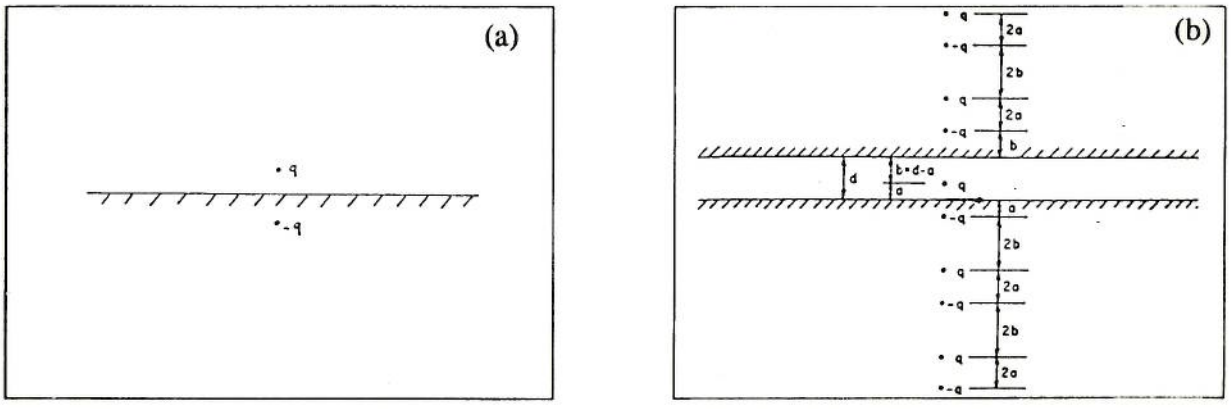


Fig. 2.10. a) A point charge q and a conducting plane; the electric force acting on charge q is equal to the electric force produced by the image charge $-q$. b) A point charge q between two parallel conducting planes; this charge leads to an infinite set of image charges of alternating signs within each conductor (from M. Zahn, *Point charge between two parallel grounded planes*, Am. J. Phys. 44 1132 (1976)).

When a point charge q is located between two parallel conducting planes, a straightforward application of the method of images leads to an infinite set of images within each conductor of alternating spacings of $2a$ and $2b$, as illustrated in fig. 10b. Thus, the classical image potential that an electron feels in the vacuum region between the electrodes can be expressed as[54]

$$V_{im}(z) = -\frac{1}{2}\left\{ \frac{1}{2z} + \sum_{n=1}^{\infty}\left[\frac{ns}{(ns)^2 - z^2} - \frac{1}{ns}\right]\right\} . \tag{2.61}$$

This expression can be rewritten, after some rearrangement, in the following way

$$V_{im}(z) = -\frac{1}{4}\left(\frac{1}{z} + \frac{1}{s-z}\right) + \frac{1}{4s}\left[\sum_{n=1}^{\infty} \frac{z/s}{n(n+z/s)} - \sum_{n=1}^{\infty} \frac{z/s}{n(n-z/s)} + \frac{1}{1-z/s}\right], \tag{2.62}$$

and taking advantage of the definition and properties of the gamma and digamma functions[55], we find

$$V_{im}(z) = -\frac{1}{4}\left(\frac{1}{z} + \frac{1}{s-z}\right) + \frac{1}{4s}\left[2\gamma + \psi\left(1+\frac{z}{s}\right) + \psi\left(2-\frac{z}{s}\right)\right], \tag{2.63}$$

or

$$V_{im}(z) = -\frac{s}{4z(s-z)} + \frac{1}{4s}\left\{ 2\gamma + s\frac{d}{dz}\left[\ln\frac{\Gamma(1+z/s)}{\Gamma(2-z/s)}\right]\right\} , \tag{2.64}$$

where γ represents the Euler number, $\Gamma(x)$ the gamma function, and $\psi(x)$ the digamma function, i.e. the logarithmic derivative of the gamma function.

When only the first image charges that the electron sees in each electrode are considered, we have

$$V_{im}(z) = -\frac{s}{4z(s-z)} . \tag{2.65}$$

Alternatively, the following approximation due to Simmons[54] has been used widely:

$$V_{im}(z) = -\frac{1.15\ \ln 2s}{4z(s-z)} . \tag{2.66}$$

Thus when the image potential is included the classical potential barrier between two planar electrodes can be expressed as

$$V(z) = \begin{cases} U_L & , \; z \le z_1 \\ -(V_a + \Delta\Phi)\frac{z}{s} + V_{im}(z) & , \; z_1 \le z \le z_2 \\ U_R & , \; z_2 \le z \end{cases} \quad , \tag{2.67}$$

where z_1 and z_2 represent the positions where the interface potential and the bulk inner potentials are equal. This image reduced potential barrier is represented in fig. 11, where the image potential given by eqs. (2.64), (2.65) and (2.66) is considered, together with the trapezoidal barrier of eq. (2.51). This figure exhibits, also, the lowered trapezoidal barrier tangent to the image reduced potential barrier of eq. (2.67); this barrier is lowered by a quantity inversely proportional to the interelectrode separation, since

$$V_{im}(s/2) = -\frac{k}{s} \quad , \tag{2.68}$$

where k is equal to ln2, 1 or 1.15 ln2, depending on which expression for the image potential is used, (2.64), (2.65) or (2.66), respectively.

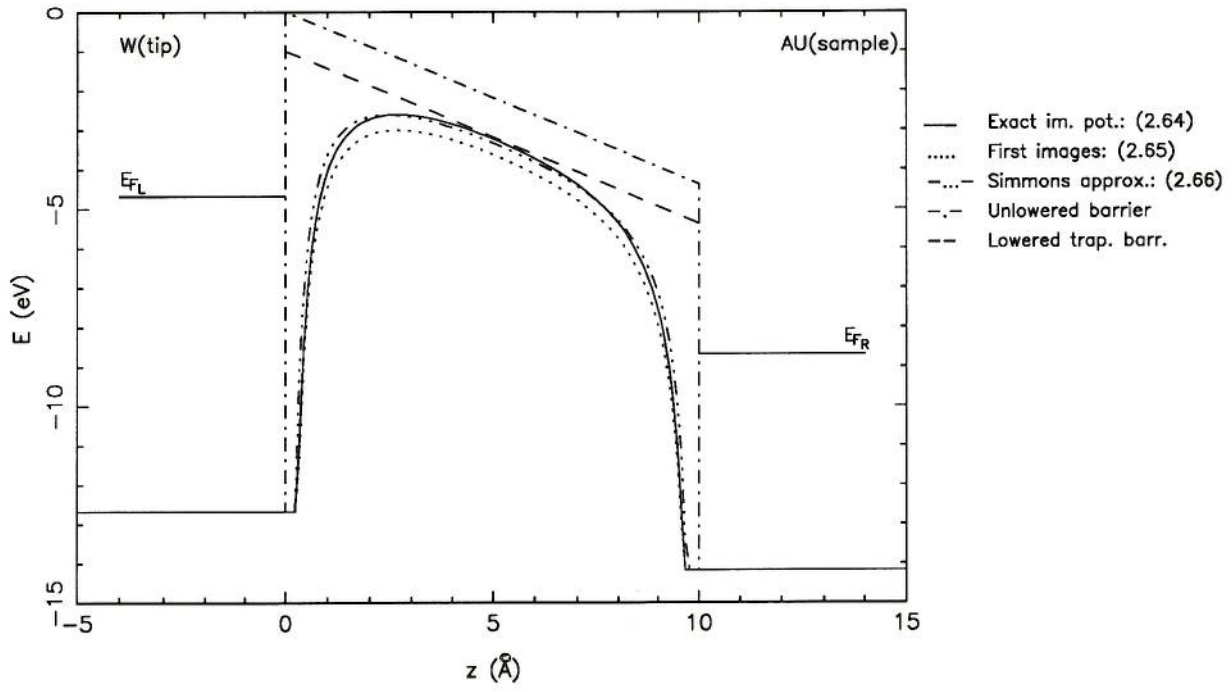


Fig. 2.11. Trapezoidal barrier of eq. (2.51) (dashed-dotted line), and image reduced potential barrier of eq. (2.67) with the image potential specified by eqs. (2.64) (solid line), (2.65) (dotted line) and (2.66) (dashed-dotted-dotted-dotted line). The lowered trapezoidal barrier tangent to the exact image reduced barrier of eqs. (2.67) and (2.64) is also shown (dashed line).

Transmission probabilities for electrons tunneling the image reduced potential barrier of eq. (2.67) have been calculated approximating the image potential by means of eq. (2.65) and solving numerically the Schrödinger equation; this has been done representing the solution as Chebyshev series[56]. Fig. 2.12 exhibits the calculated transmission probabilities, as a function of energy, for U_L = -12.68eV, U_R = -9.8eV, V_a = 4V, s = 10Å and F = -0.438eV/Å, together with the transmission probabilities for electrons tunneling the corresponding lowered trapezoidal barrier and the lowered bound levels of the infinite barrier.

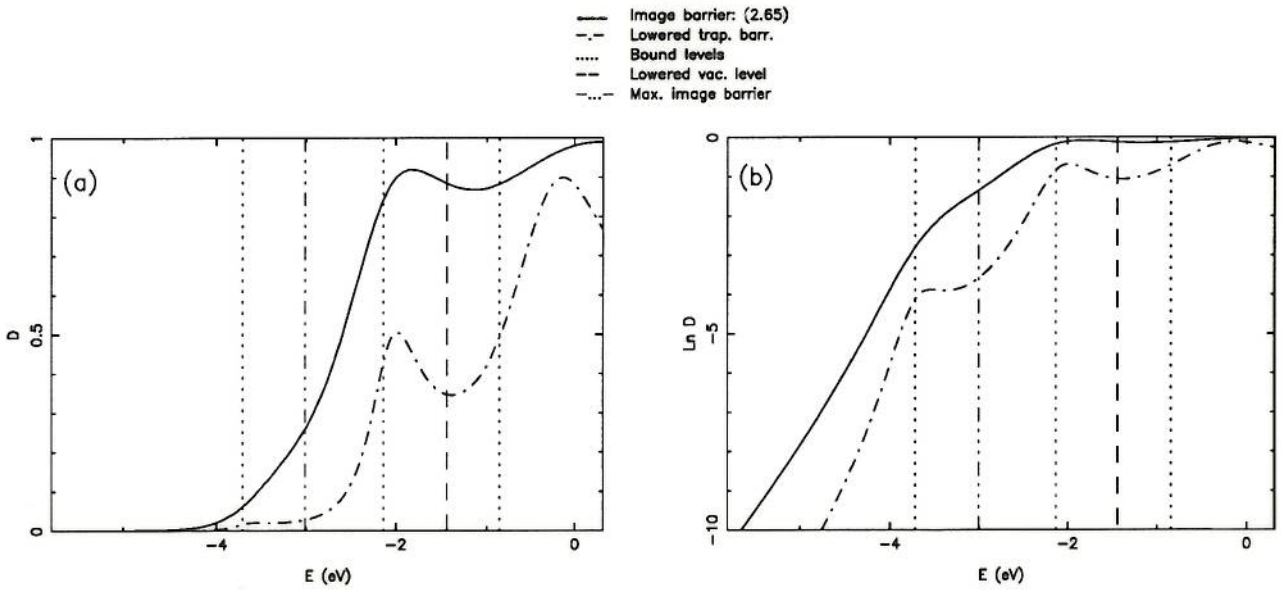


Fig. 2.12. a) Transmission probability of electrons tunneling the image reduced barrier with the image potential given by eq. (2.65) (solid curves), together with the transmission probability of electrons tunneling the corresponding lowered trapezoidal barrier (dashed-dotted curves), as a function of energy. Fig. 2.12b exhibits plots of the natural logarithm of the transmission probabilities of fig. 2.12a. The lowered bound energy levels of the infinite barrier (vertical dotted lines), the lowered vacuum level of the negatively biased electrode (vertical dashed line) and the maximum of the image reduced barrier (vertical dashed-dotted-dotted-dotted line) are also shown. U_L = -12.68eV, U_R = -9.8eV, V_a = 4V, s = 10Å and F=-0.438eV/Å.

Notice that the resonant levels of the image reduced potential barrier approximately coincide with the resonant levels of the lowered trapezoidal barrier, and thus coincide with the lowered bound levels of the infinite barrier for energies well below the lowered vacuum level of the negatively biased electrode. Hence, these resonant levels are lowered by a quantity

proportional to the interelectrode separation, and, accordingly, the lowering of the resonant levels gets more important as the interelectrode separation decreases. It is interesting to point out, also, that for energies below the Fermi level of the negative electrode the first transmission resonance of the image reduced potential barrier appears at smaller energies than the one obtained for the lowered trapezoidal barrier, especially for small bias; indeed, this first resonant level converges at $V_a = 0$ and large separations to the intrinsic image states[57], as pointed out by García et al[58].

On the other hand, considering the image reduced potential barrier rather than the trapezoidal barrier leads less pronounced peaks in the transmission probabilities, since this potential barrier is less abrupt than the trapezoidal one.

Tunneling characteristics: s-V_a and dI/dV_a-V_a

The scanning tunneling microscope can be used keeping the tunneling current constant and displacing the tip in the perpendicular direction to the surface as the applied voltage increases[22-25]. Hence, when the applied voltage gets greater than the work function of the positively biased electrode, field emission occurs, as pointed out above, and the electric field between the electrodes keeps approximately constant, in the constant current mode, as the applied voltage increases, assuming that the effective tunneling area keeps also constant.

Considering planar electrodes, the tunneling current density may be obtained by means of eq. (2.9), once the transmission probabilities for allowed energies are calculated; then, the tunneling current is obtained as the product of the current density times the tunneling area. Nevertheless, the tip-sample separation of the microscope that for a given value of the applied voltage makes constant the tunneling current cannot be obtained directly from eq. (2.9); instead, we must search numerically for the zeros of the following function:

$$f(s) = I(s) - I_0 \ , \tag{2.69}$$

where $I(s)$ is the tunneling current between two planar electrodes separated by a distance s, and I_0 is the constant value of the tunneling current. Notice that each time we search for the value

that the function of eq. (2.69) has got, the transmission probabilities, which are to be calculated solving the time-independent Schrödinger equation through the barrier in question must be integrated over all allowed energies, as shown in eq. (2.9); therefore, calculating the constant current mode tip-sample separation for a given value of the applied voltage, and, therefore, calculating the constant current mode s-V_a characteristics is a cumbersome and tedious computation, especially when the Schrödinger equation must be solved numerically.

Fig. 2.13 shows the constant current density mode distance-voltage characteristics calculated for U_L = -12.68eV, U_R = -9.8eV, Φ_L = 4.68eV, Φ_R = 4.3eV and J = 0.1nA/Å^2, when electrons are assumed to tunnel an image reduced potential classical barrier with the image potential given by eq. (2.65), together with the corresponding results obtained when the non-lowered and lowered trapezoidal barriers are considered.

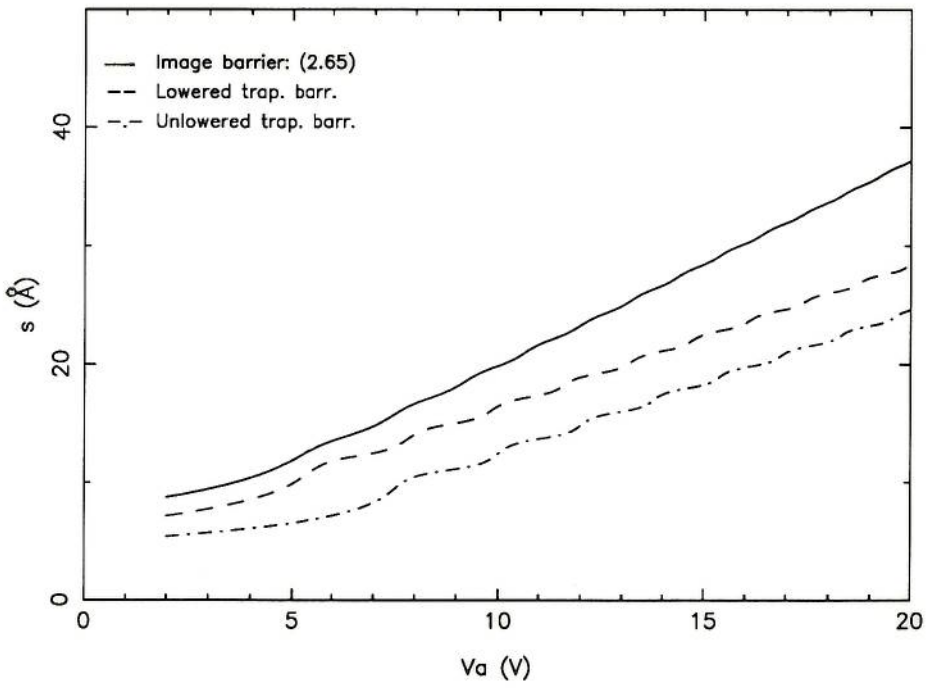


Fig. 2.13. Constant current density mode s-V_a characteristics for J = 0.1nA/Å^2 and different barrier models: The image reduced potential barrier of eq. (2.67) with the image potential specified by eq. (2.65) (solid curve), the corresponding lowered trapezoidal barrier (dashed curve) and the non-lowered trapezoidal barrier (dashed-dotted curve). U_L =-12.68eV, U_R = -9.8eV, Φ_L = 4.68eV and Φ_R = 4.3eV.

Notice that when the non-lowered trapezoidal barrier is considered in our calculations the constant current density mode electric field F keeps approximately constant in the

field-emission regime. However, when the lowered trapezoidal barrier is considered, the electric field does not keep constant at all; instead, it increases with V_a, since the height of the lowered barrier that electrons have to tunnel gets greater as the tip-sample separation increases. When electrons are assumed to tunnel the image reduced barrier, the constant current density mode electric field keeps nearly constant, too; this happens because though the height of the image reduced barrier increases as the tip-sample separation gets larger, at high voltages the barrier that electrons have to tunnel, which is very close to the negatively biased electrode´s surface, does not change appreciably with tip-sample separation.

It is interesting to observe that for certain values of the applied voltage the constant current density mode separation presents oscillations. It happens because for these values of the applied voltage a new transmission resonance appears below the Fermi level of the negatively biased electrode, as discussed above. Notice, also, that these oscillations are less pronounced when the position dependent image reduced potential barrier of eq. (2.67) is considered; this happens because the transmission resonances are smoother, too, as shown in fig. 2.12.

Fig. 2.14 shows the lowered bound energy levels corresponding to the image reduced potential barrier of eq. (2.67) with the image potential approximated by eq. (2.65), together with the non-lowered bound levels, as a function of the applied voltage, when the tip-sample separation making the tunneling current density through the image reduce barrier of eqs. (2.65) and (2.67) equal to 0.1nA/Å^2 is considered for each value of the applied voltage. It is worth noting that the values of the bias voltage for which an additional level appears below the Fermi level of the negatively biased electrode correlate with the oscillations appearing in the $s(V_a)$ curve represented in fig. 2.13 by a solid curve. Notice that the distances between these oscillations are slightly smaller than those between the non-lowered bound energy levels, since the levels are lowered by a quantity inversely proportional to the separation, which gets greater in the constant current density mode as the voltage increases.

These oscillations become more obvious when we evaluate the constant current density mode conductance, dI/dV_a, as a function of the applied voltage, derivating along the constant current density mode $s(V_a)$ curve. This may be done numerically, and the results so obtained

for a constant current density of $0.1 nA/Å^2$ are presented in fig. 2.15, when electrons are assumed to tunnel the image reduced barrier of eqs. (2.65) and (2.67), the corresponding lowered trapezoidal barrier and the non-lowered trapezoidal barrier of eq. (2.51), as in fig. 2.13.

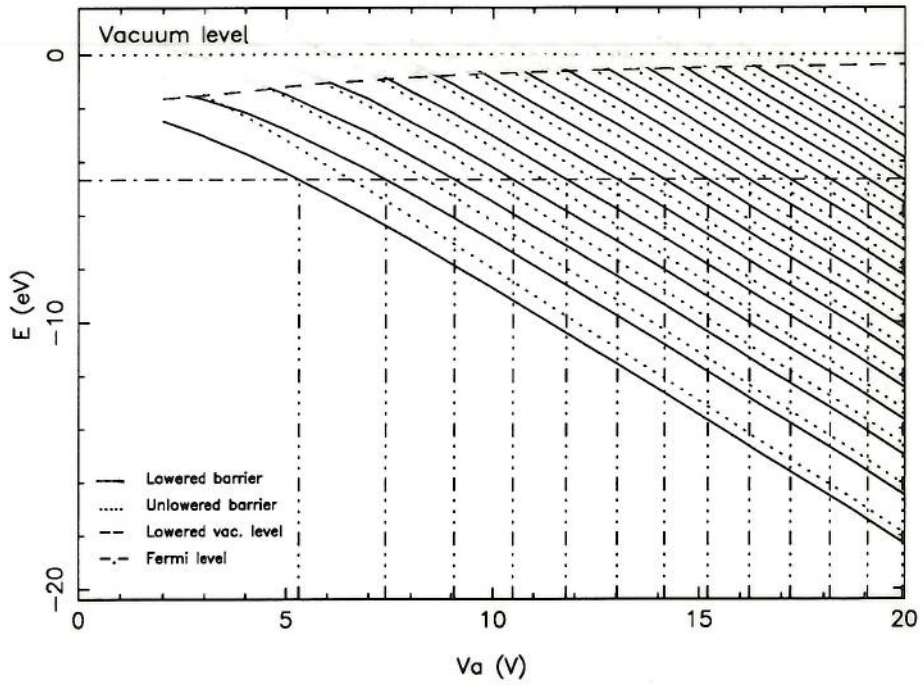


Fig. 2.14. Evolution of the lowered bound energy levels corresponding to the image reduced barrier with the image potential specified by eq. (2.65) (solid curves), together with the non-lowered bound energy levels (dotted curves), as a function of applied voltage, when the constant current density mode tip-sample distance s represented by the solid curve of fig. 2.13 is considered for each value of V_a. For energies below the Fermi level of the negatively bias electrode resonances of the lowered and non-lowered trapezoidal barriers exactly coincide with the lowered and non-lowered bound energy levels of the infinite barrier, respectively. The values that the applied voltage has each time an additional resonant level incorporates to the allowed energy region of tunneling electrons are represented by vertical lines, as in figs. 2.8b and 2.9.

The oscillations appearing in the conductance-voltage characteristics represented in fig. 2.15 by a solid line also correlate with the vertical lines of fig. 2.14; the first peak appears at a slightly smaller voltage than the one represented by the first vertical line of fig. 2.14, due to the fact that the first transmission resonance appears at smaller energies when the position dependent image reduced barrier of eq. (2.67) is considered, as discussed above; the remainder peaks appear at slightly greater voltages that the ones represented in fig. 2.14,

probably due to the contribution from electrons having the energy component E_z less than the Fermi energy. However, the oscillations appearing in the conductance-voltage characteristics obtained for the trapezoidal models of the barrier do not correlate with the vertical lines of fig. 2.14, not even when the lowered trapezoidal barrier tangent to the image reduced barrier is considered; this happens because though for a given s-V_a characteristic the peak positions would approximately coincide for both trapezoidal and non-trapezoidal image reduced barriers, the s-V_a characteristic and, hence, the electric field are very different for both barriers, thus becoming the bound energy levels and the peak positions in the $dI/dV_a(V_a)$ curve also different, in addition to the different shapes they present, which is due to the difference in the breadth of the transmission resonances.

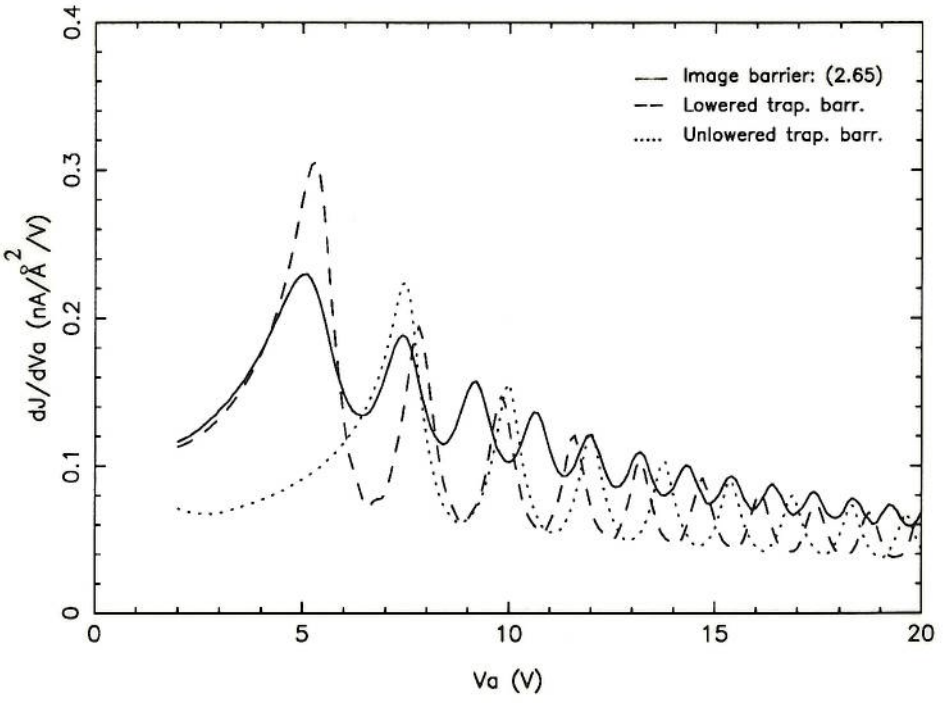


Fig. 2.15. Constant current density mode dJ/dV_a-V_a characteristics for J = 0.1nA/Å^2 and different barrier models, as in fig. 2.13. U_L = -12.68eV, U_R = -9.8eV, Φ_L = 4.68eV and Φ_R = 4.3eV.

On the other hand, the peak positions of the oscillations appearing in the conductance-voltage characteristics show a considerable dependence on the approximation used to evaluate the image potential, since different approximations lead to different heights of the image reduced barrier, as shown in fig. 2.16.

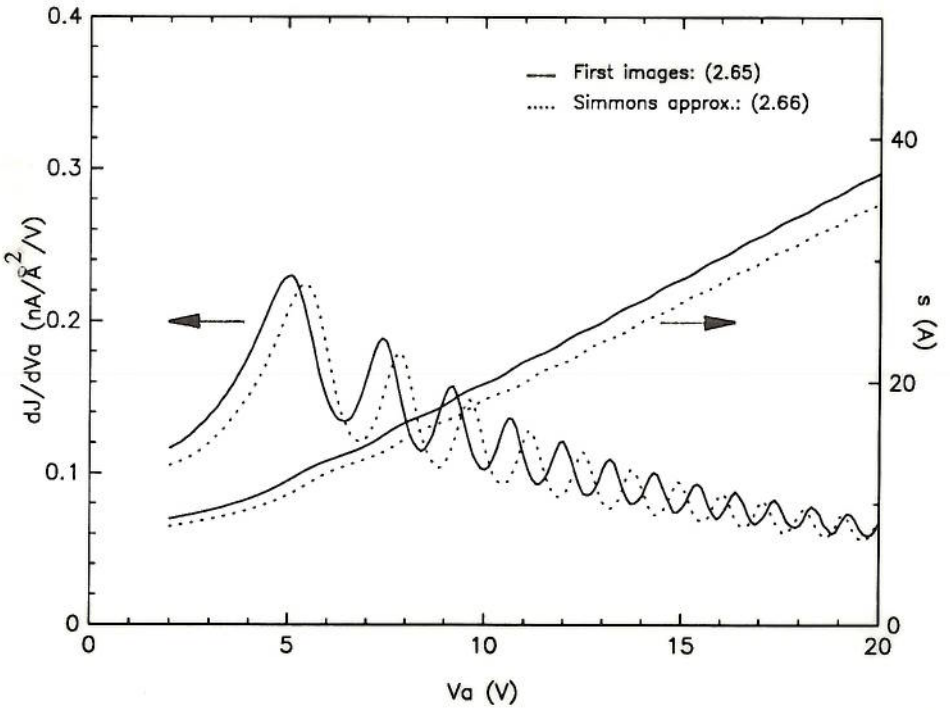


Fig. 2.16. Constant current density mode s-V_a and dJ/dV_a-V_a characteristics for J = 0.1nA/Å^2 and the image reduced potential barrier of eq. (2.67) with the image potential specified by eq. (2.65) (solid curves) and with the approximated image potential of Simmons, i.e. eq. (2.66) (dotted curves). U_L = -12.68eV, U_R = -9.8eV, Φ_L = 4.68eV and Φ_R = 4.3eV.

The peak positions of the oscillations appearing in the conductance-voltage characteristics are very sensitive, also, to the values of the work functions, which are not known with sufficient precision, and to the effective tunneling area, since the constant current mode s-V_a characteristics and, hence, the electric field and the resonant levels are strongly dependent on these quantities. This is illustrated in fig. 2.17, where plots are shown of the constant current density mode distance-voltage and conductance-voltage characteristics for different work functions and current densities when electrons are assumed to tunnel the image reduced barrier of eq. (2.67) with the image potential approximated by eq. (2.65). The dependence of the peak positions of the oscillations on the tunneling current density is of great interest because the tunneling area could vary during the experiment, in such a way that the constant current mode current density may not be constant, as will be discussed in section 2.5.

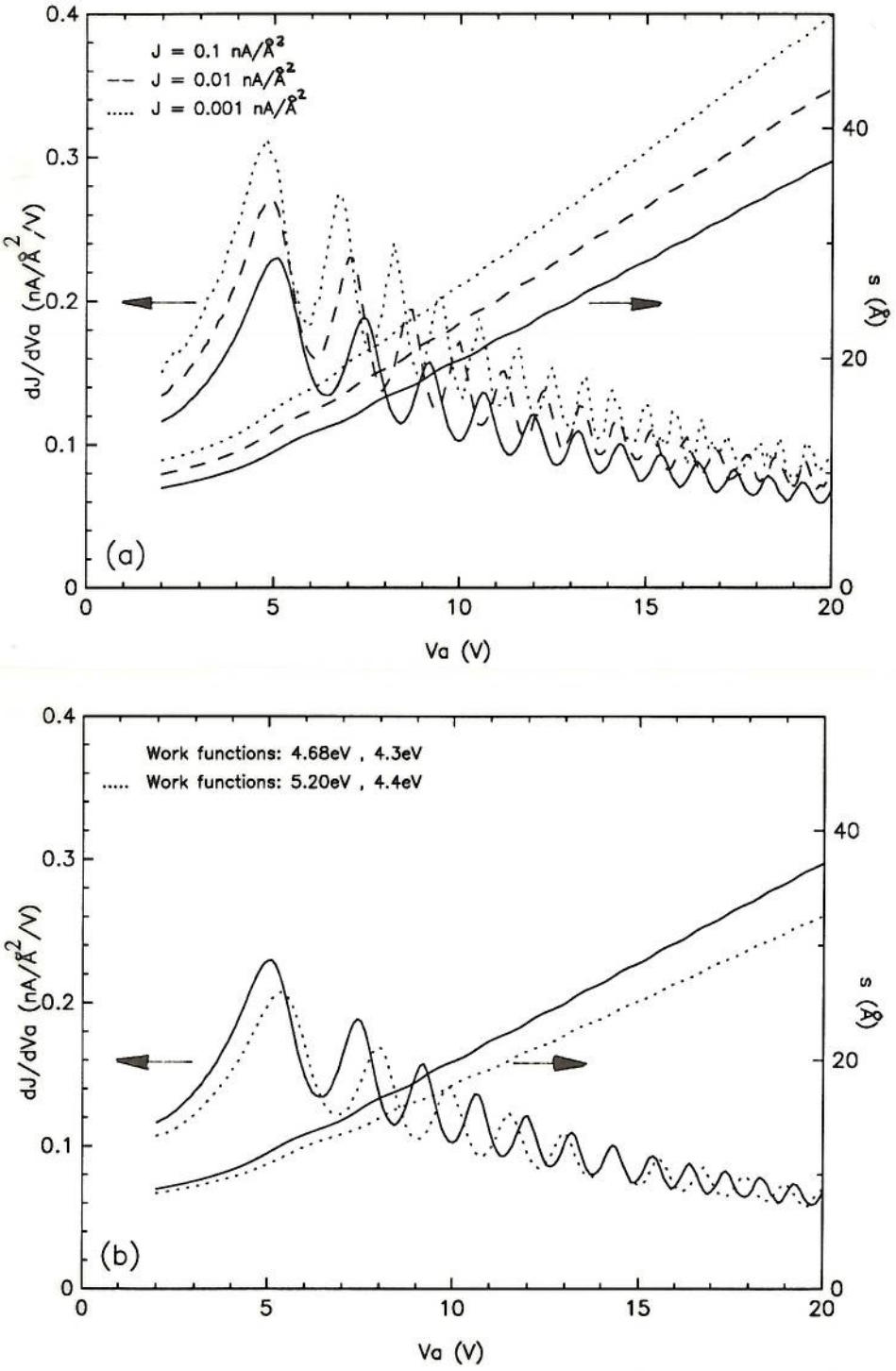


Fig. 17. Constant current density mode s-V_a and dJ/dV_a characteristics for the image reduced potential barrier of eq. (2.67) with the image potential approximated by eq. (2.65) and different current densities and work functions. In fig. 2.17a different current densities have been considered: $J = 0.1\text{nA/Å}^2$ (solid curves), $J = 0.01\text{nA/Å}^2$ (dashed curves) and $J = 0.001\text{nA/Å}^2$ (dotted curves), with $\Phi_L = 4.68\text{eV}$ and $\Phi_R = 4.3\text{eV}$. In fig. 2.17b different work functions have been considered: $\Phi_L = 4.68\text{eV}$ and $\Phi_R = 4.3\text{eV}$ (solid curves), and $\Phi_L = 5.20\text{eV}$ and $\Phi_R = 4.4\text{eV}$ (dotted curves), with $J = 0.1\text{nA/Å}^2$.

In particular, using the approximate formula of Simmons, i.e. eq. (2.66) for the image potential, a quite good agreement with the experimental data given by Becker et al when electrons tunnel from W to Au[24] may be obtained in the peak positions of the oscillations appearing in dI/dV_a-V_a[59], choosing the work functions and tunneling area in a proper manner. However, agreement is not obtained for the same parameters and the inverse polarization. On the other hand, the constant current mode tunneling characteristics are very sensitive to the shape of the interface potential profile and to the geometry of the electrodes, as will be shown in next sections. Consequently, it is necessary to consider more realistic barrier models and geometries; moreover, a trial and error analysis of the constant current mode tunneling characteristics may be used to determine both the shape of the interface potential and the radius of the tip.

In sections 2.4 and 2.5 calculations of s-V_a and dI/dV_a-V_a characteristics of a W-Au interface are performed and an interpretation of the experimental data given by Becker et al for direct and inverse polarization is presented. In section 2.4 tunneling between two planar metallic electrodes through a new potential barrier model which takes into account both non-local and local exchange and correlation effects is considered. In section 2.5 our full analysis of the three-dimensional models is presented, taking into account the tip-sample geometry.

As we do not know the work functions of the electrodes with sufficient precision, we have performed the calculations of sections 2.4 and 2.5 for different values of the work functions, and we have found that good agreement with the experimental data is obtained when they are assumed to be $\Phi_L = 5.2$eV and $\Phi_R = 4.4$eV for W and Au, respectively[60].

2.4. Potential barrier: one-dimensional model

Since the pioneering works of Lang and Kohn[61-63] based on the density-functional theory of inhomogeneous electron gas systems formulated by Hohenberg, Kohn and Sham[64,65], the density-functional formalism in the local-density approximation (LDA) for exchange and correlation has been widely used in the study of the jellium model of surfaces. This approximation has been applied with success to the calculation of the electronic structures of metal surfaces and, in particular, to the study of the short-range quantum-mechanical interactions that the electron sorrounding the surface encounters, which is one of the fundamental problems in surface physics.

However, the local-density approximation fails to reproduce the correct asymptotic behaviour of the potential in the vacuum region of the surface, since in this approximation the exchange-correlation potential decreases exponentially out of the surface, so it does not behave at large distances like the correct classical image potential due to the induced mirror-image in the metal. On the other hand, the role that the long-range image potential interaction plays has been shown to be important to account for the existence of the image bound states[57] lately observed[66-69] and also to give an interpretation of the experiments performed with the STM.

The problem of the long-range attractive potential between an external charged particle and a semi-infinite polarizable medium has been treated by a variety of semiclassical and quantum-mechanical approaches[70-73]. However, the interface potential between two surfaces appears as the result of different local and non-local effects[74,75]; non-local effects are reflected in the long-range image potential induced by both surfaces, while local effects, which can be obtained using the local density approach, are responsible for the fact that the effective potential barrier that electrons feel goes more smoothly to its bulk value than the classical image reduced barrier.

On the other hand, although for large distances between the electrodes the effective potential barrier should converge in the middle of the gap to the classical image reduced barrier, it has been shown[74] that for tip-sample distances of a few ångstroms the barrier is substantially decreased by the overlapping of the metal electronic charges. In addition,

dynamic effects tend to reduce the strength of the induced image potential[76,77], depending on the relation between the tunneling transversal time and the response time of both metals (typically given by the inverse of their plasmon frequencies); for very short transversal times the image potential would be reduced to zero, but theoretical calculations[77] show that for typical tip-sample distances of a few ångstroms the image potential is just reduced to around 70% of its full classical value.

Recently, a parametrized model of the potential at a metal surface has been suggested[78]:

$$V(z) = \begin{cases} \dfrac{U_0}{A\, e^{-B\,(z - z_0)} + 1}, & z \le z_0 \\ \dfrac{1 - e^{-\lambda\,(z - z_0)}}{4\,(z - z_0)}, & z_0 \le z \end{cases} \qquad (2.70)$$

referenced to the vacuum level. U_0 represents the bulk inner potential, the quantity λ determines the range of transition from the vacuum potential to its value in the bulk, and z_0 represents the position of the image plane relative to the edge of the positive background; the image plane is defined as the centre of mass of the induced charge distribution[63,79,80]. The constants A and B are determined by matching $V(z)$ and its derivative at the image plane, i.e. at $z = z_0$; this leads to

$$A = -\frac{2\,U_0}{\lambda} - 1 \qquad (2.71)$$

and

$$B = -\frac{U_0}{A} \,. \qquad (2.72)$$

Parametrized potential barrier at a metal-vacuum-metal interface

In order to take into account the physical basis of the problem discussed above, we generalize the parametrized surface potential of eq. (2.70) and propose the following barrier model for tunneling electrons at a metal-vacuum-metal interface[29,30]:

$$V(z) = \begin{cases} \dfrac{U_L}{A_L e^{B_L (z - z_L)} + 1} & , z \le z_L \\ -\dfrac{1}{4}\left[\dfrac{1 - e^{-\lambda_L (z - z_L)}}{z - z_L} + \dfrac{1 - e^{-\lambda_R (s - z_R - z)}}{s - z_R - z} - \dfrac{\mu}{d} f(z) \right] + V_e(z) & , z_L \le z \le s - z_R \\ \dfrac{U_R}{A_R e^{B_R (s - z_R - z)} + 1} & , s - z_R \le z \end{cases} \quad (2.73)$$

referenced to the vacuum level of the negatively biased electrode, which occupies the $z \le 0$ half-space. In this expression,

$$V_e(z) = -(V_a + \Phi_L - \Phi_R)\frac{z}{s} \quad (2.74)$$

and

$$f(z) = 2\gamma + \Psi\left(1 + \frac{z - z_L}{d}\right) + \Psi\left(2 - \frac{z - z_L}{d}\right). \quad (2.75)$$

U_L, Φ_L and U_R, Φ_R represent the bulk inner potential and the work function of the electrodes L and R, respectively, and d is the gap distance, which is defined to be the distance between the image planes situated at $z = z_L$ and $z = s - z_R$. A_L, B_L , A_R and B_R are determined by matching $V(z)$ and its derivative at the position of the image planes, which leads

$$A_{L,R} = \frac{-4\,U_{L,R}}{\lambda_{L,R} + \left[1 - \mu - \exp(-\lambda_{R,L}\, d)\right]/d + 4\,(V_a + \Delta\Phi)\, z'_{L,R}/s} - 1 \quad (2.76)$$

and

$$B_{L,R} = \frac{(A_{L,R} + 1)^2}{A_{L,R}} \frac{\lambda_{L,R}^2/2 - \left[1 - \mu - (1 + \lambda_{R,L}\, d)\exp(-\lambda_{R,L}\, d)\right]/d^2 \pm 4\,(V_a + \Delta\Phi)/s}{-4\,U_{L,R}} , \quad (2.77)$$

where

$$z'_L = z_L \quad (2.78)$$

and

$$z'_R = s - z_R . \quad (2.79)$$

In these expressions the notation "±" means that when B_R is to be calculated "+" must be used; similarly, "-" must be used when B_L is to be calculated.

The quantities λ_L and λ_R, as the quantity λ in eq. (2.70), determine the range of transition from the vacuum potential to its value in the bulk; for $d \gtrsim 5$Å they have a simple physical interpretation, since they tell us about the value of the potential at the image planes:

$$V(z_L) \approx -\left(\frac{\lambda_L}{4} + \frac{1-\mu}{4d}\right) - (V_a + \Delta\Phi)\frac{z_L}{s} \tag{2.80}$$

and

$$V(s - z_R) \approx -\left(\frac{\lambda_R}{4} + \frac{1-\mu}{4d}\right) - (V_a + \Delta\Phi)\frac{s - z_R}{s} \ . \tag{2.81}$$

Assuming that the crossing of the potential barrier and the image planes happens between the Fermi level and the bulk inner potential level[63], we should choose one of the following values of the quantities λ_L and λ_R:

$$4\,\Phi_{L,R} - \frac{1-\mu}{d} \le \lambda_{L,R} \le 4\,(\Phi_{L,R} + E_{F_{L,R}}) - \frac{1-\mu}{d} \ . \tag{2.82}$$

The quantity μ tells us about the dependence of the barrier height on the gap distance, since for $d \gtrsim 5$Å we have

$$V\left(z_L + \frac{d}{2}\right) \approx -\frac{1-\mu(1-\ln 2)}{d} - \frac{1}{2}(V_a + \Delta\Phi)\left(1 + \frac{z_L - z_R}{s}\right) \ . \tag{2.83}$$

Consequently, $\mu \,.\, (1 - \ln 2) / d$ represents the increase of the height of the potential (2.73) over the height of the image reduced potential (2.67) with the image potential approximated by eq. (2.65); thus in the tunneling region, far outside the image planes, the model barrier of eq. (2.73) converges to the exact image reduced barrier when $\mu = 1$ and to the image reduced barrier with the image potential approximated by eqs. (2.65) and (2.66) when $\mu = 0$ and $\mu \approx 0.66$, respectively.

The potential barrier of eq. (2.73) is represented in fig. 2.18 for different values of the parameters λ_R, μ, z_L and z_R, together with the exact image reduced potential barrier of eqs. (2.64) and (2.67).

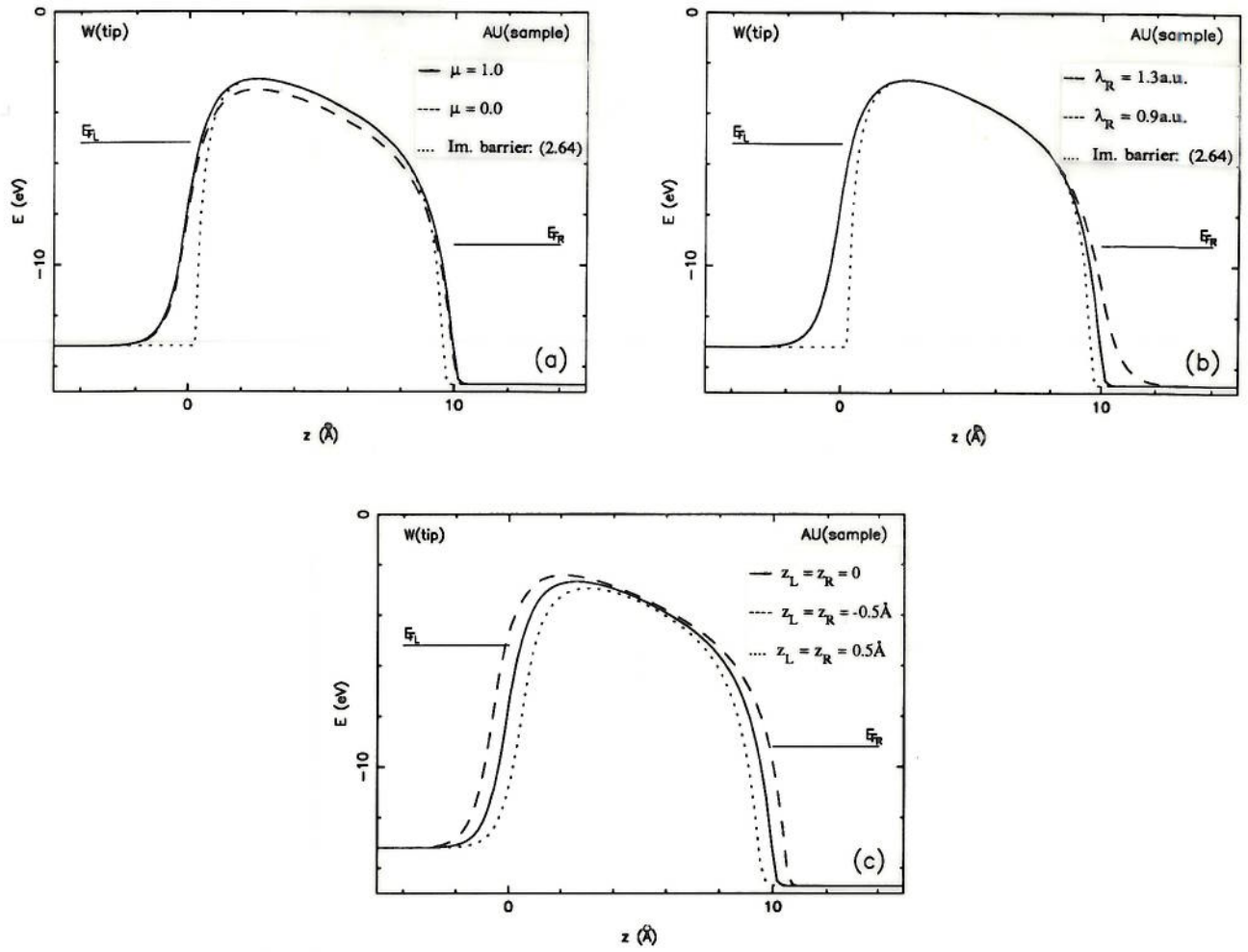
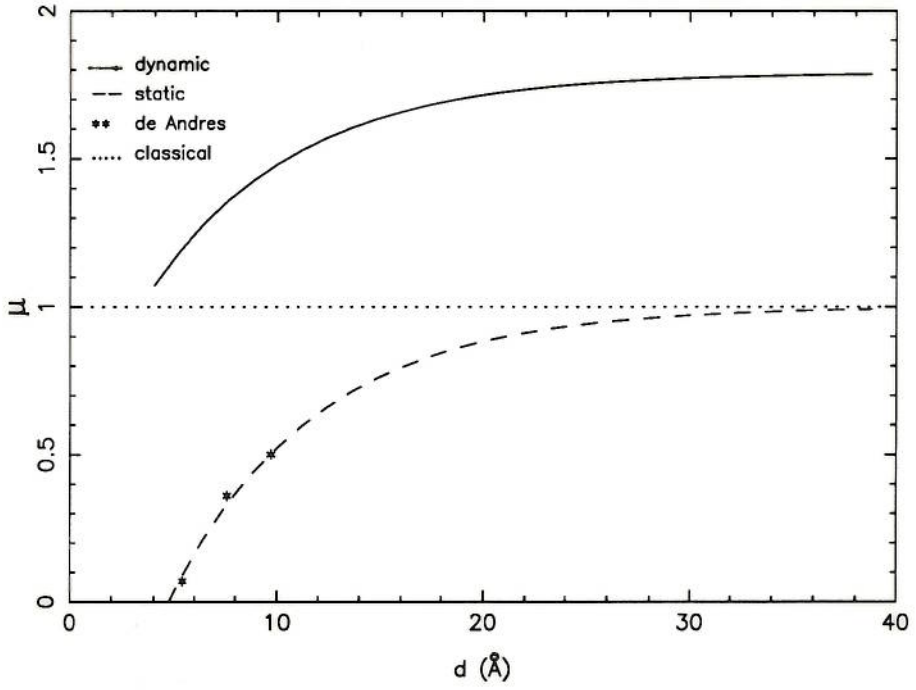


Fig. 2.18. Model potential barrier of eq. (2.73) with $\lambda_L = 1.0a_0^{-1}$, $\lambda_R = 1.3a_0^{-1}$, $z_L = z_R = 0$ and two different values of the parameter μ (fig. 2.18a), with $\lambda_L = 1.0a_0^{-1}$, $\mu = 1.0$, $z_L = z_R = 0$ and two different values of the parameter λ_R (fig. 2.18b), and with $\lambda_L = 1.0a_0^{-1}$, $\lambda_R = 1.3a_0^{-1}$, $\mu = 1.0$ and three different positions of the image planes (fig. 2.18c). In figs. 2.18a and 2.18b the exact classical image reduced potential barrier of eqs. (2.67) and (2.64) is also shown (dotted curves). $\Phi_L = 5.2$eV, $\Phi_R = 4.4$eV, $U_L = -13.2$eV , $U_R = -9.9$eV , $V_a = 4.0$V and $s = 10$Å .

The model barrier of eq. (2.73) fits the theoretical potential of de Andrés et al[74], which includes both local and non-local effects, by appropriately choosing λ_L, λ_R and μ. In particular, for d ≈ 9Å a good fitting is obtained for $\mu = 0.5$; a good fitting is obtained, also, using smaller values of the parameter μ when $d < 9$Å, which shows that for small tip-sample distances the barrier is substantially decreased due to the local exchange and correlation energy, and it does not converge to the exact classical image reduced potential barrier. These local effects depend on the gap distance and become negligible for large gap distances, indicating that some kind of dependence of the parameter μ on the distance between image

planes should be included. For large gap distances μ should converge to unity, if dynamic effects were neglected; but the static parameter μ that for small distances fits the potential of de Andrés et al and for large distances converges to unity should be enhanced in order to take into account dynamic effects. Fig. 2.19 exhibits μ as a function of gap distance for the static and dynamic cases, having assumed that the image potential is reduced to 65% of its full value due to dynamic effects.



2.19 irudia. Dependence on the gap distance of the parameter μ that makes the potential barrier of eq. (2.73) to fit at small distances the potential barrier of ref. 74 and to converge at large distances to the exact image reduced classical barrier (dashed curve); the cross points show the values of the parameter μ making the potential barrier of eq. (2.73) to fit the potential barrier of ref. 74 for gap distances of 5.4, 7.6 and 9.7Å, and the solid curve represents the dynamic parameter μ dependence on the gap distance obtained when the image potential is assumed to be reduced by dynamical effects by 65%.

On the other hand, we have found[31], also, that the apparent barrier height calculated with the model interface potential specified by eq. (2.73) is for short gap distances ($d < 6$Å) in good agreement with Lang´s calculation[81] made in the local density approximation; at greater distances our potential yields the appropriate apparent barrier height associated with image effects.

The experimentally observed oscillations in the constant current mode tunneling

conductance, as well as the transmission resonances ocurring in the positive kinetic energy region, are very sensitive to the detailed form of the interface potential barrier. In particular, the peak positions and the shape of the oscillations appearing in the constant current mode conductance-voltage characteristics depend critically on the barrier height and on the shape of the barrier in the region close to the positively biased electrode, so that both quantities μ and λ_R in eq. (2.73) play an important role in the study of such oscillations. In addition, the dependence of the tunneling current and, hence, the constant current mode separation and conductance on μ is also important, while the dependence of the tunneling current on λ_L and λ_R is negligible. Therefore, we fix λ_L and consider λ_R and μ as two fitting parameters.

Tunneling characteristics: s-V_a and dI/dV_a-V_a

Figs. 2.20a and 2.20b show constant current density mode distance-voltage and conductance-voltage characteristics calculated for $J = 0.1\text{nA/Å}^2$ when electrons tunnel the potential barrier of eq. (2.73) with $\lambda_L = 1.0a_0^{-1}$, $z_L = z_R = 0$ and different values of the parameters λ_R and μ, together with the same characteristics calculated for the image reduced classical barrier of eq. (2.67) with the image potential approximated by eq. (2.65). Fig. 2.20c shows the same characteristics calculated for the model barrier of eq. (2.73) with $\lambda_L = 1.0a_0^{-1}$, $\lambda_R = 1.3a_0^{-1}$, $\mu = 1.0$ and different positions of the image planes.

The positions of the oscillations appearing in the $dI/dV_a(V_a)$ curve calculated for the image reduced classical barrier approximately coincide with the corresponding positions obtained for the potential barrier of eq. (2.73) with $\mu = 0$, since for this value of the parameter μ the heights of both potential barriers coincide. However, the potential barrier of eq. (2.73), which represents a more realistic potential for ideal surfaces, is smoother than the classical image reduced classical barrier in the regions close to both surfaces and, hence, yields smoother dI/dV_a-V_a characteristics, which become even smoother as λ_R gets smaller.

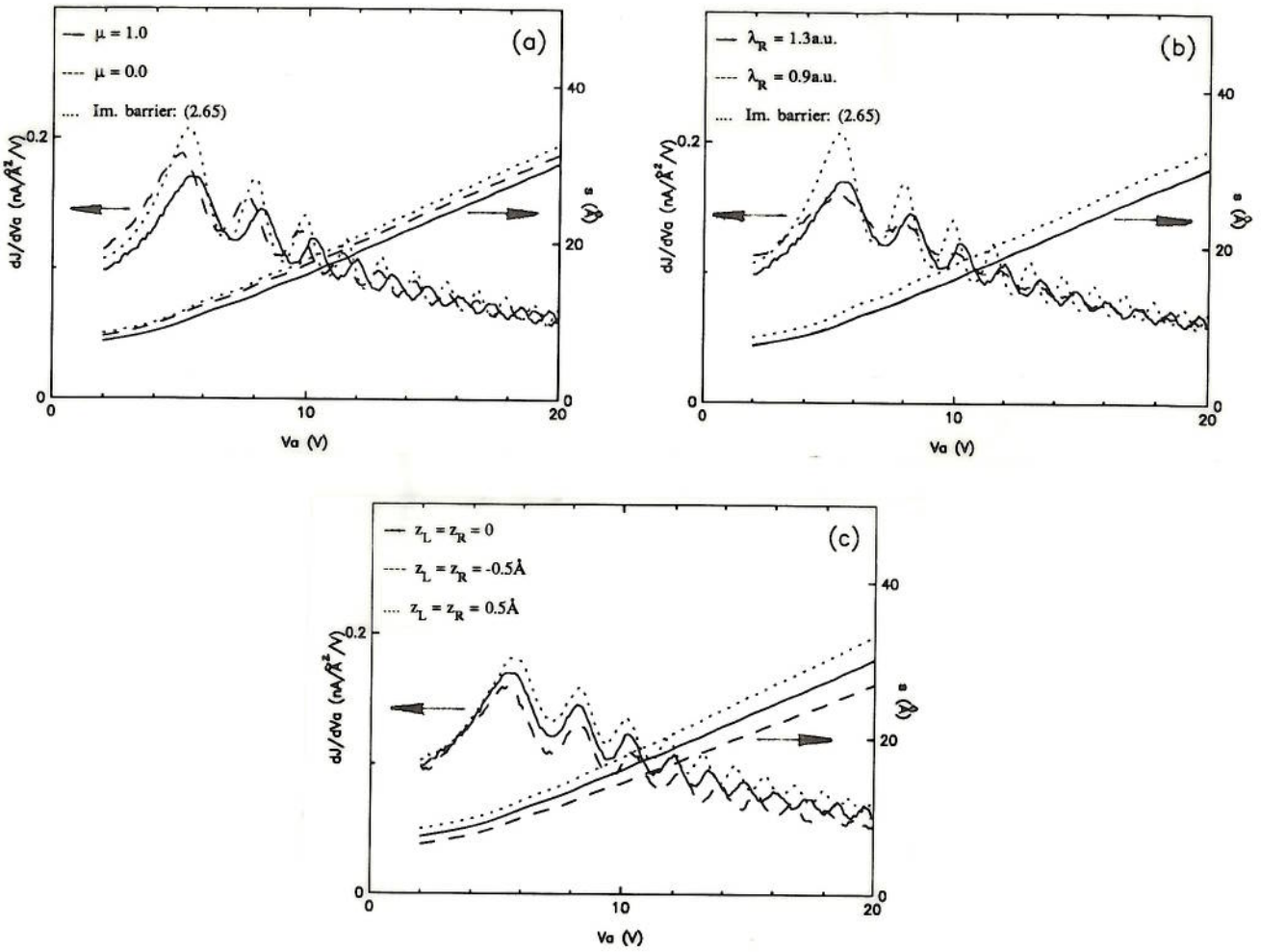
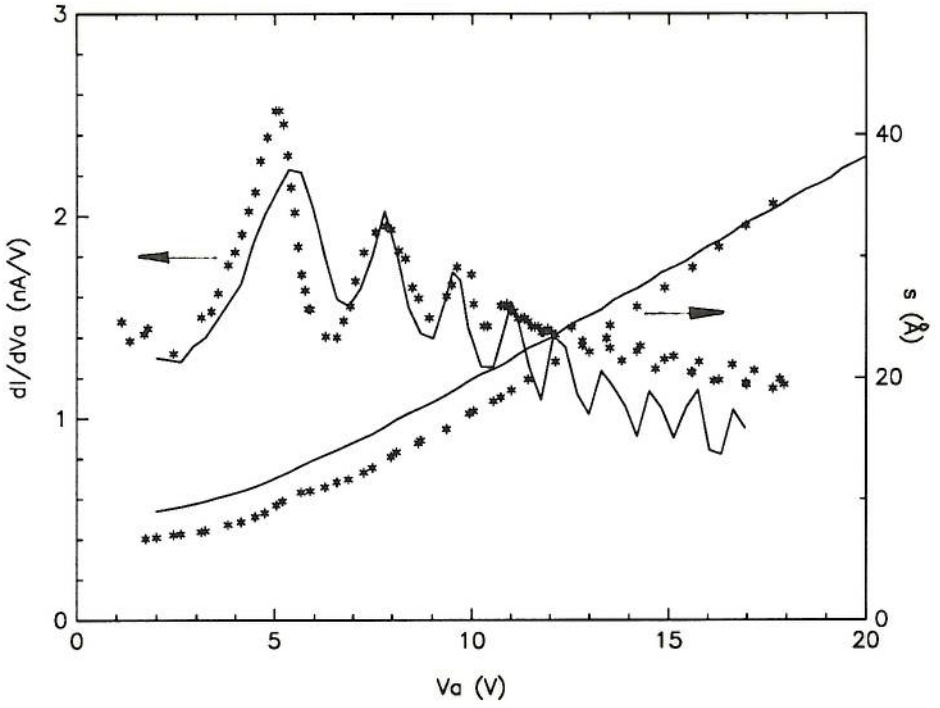


Fig. 20. Constant current density mode s-V_a and dI/dV_a-V_a characteristics for $J = 0.1\text{nA/Å}^2$ and the potential barrier of eq. (2.73), with $\lambda_L = 1.0a_0^{-1}$, $\lambda_R = 1.3a_0^{-1}$, $z_L = z_R = 0$ and two different values of the parameter μ (fig. 2.20a), with $\lambda_L = 1.0a_0^{-1}$, $\mu = 1.0$, $z_L = z_R = 0$ and two different values of the parameter λ_R (fig. 2.20b), and with $\lambda_L = 1.0a_0^{-1}$, $\lambda_R = 1.3a_0^{-1}$, $\mu = 1.0$ and three different positions of the image planes (fig. 2.20c). In figs. 2.20a and 2.20b the results of fig. 2.15 obtained for $J = 0.1\text{nA/Å}^2$ and the image reduced classical barrier with the image potential approximated by eq. (2.65) are also shown (dotted curves), for comparison. Φ_L = 5.2eV, Φ_R = 4.4eV, U_L = -13.2eV and U_R = -9.9eV.

On the other hand, when the image planes are located in the vacuum outside the positive background of the electrodes ($z_L > 0$ and $z_R > 0$), the constant current density mode separation gets greater and the oscillations become slightly less spaced in voltage, as shown in fig. 2.20c.

The experimentally observed oscillations appearing in the constant current mode $dI/dV_a(V_a)$ curve have been compared to our theoretical calculations obtained for different values of the tunneling current and the parameters λ_R and μ appearing in the model barrier of

eq. (2.73). It has been found that the shape of the experimentally observed oscillations are fitted for large values of λ_R, which make the interface potential close to the positively biased electrode more abrupt. It has been found, also, that when the gap distance dependent dynamic parameter μ of fig. 2.19, the image plane positions $z_L = z_R = 0$ and $\lambda_R = 1.3a_0^{-1}$ are considered, a reasonable fit between the low voltage peak positions of the calculated conductance and the experimental curve taken from ref. 24 is obtained asumming a constant area of 500Å, as shown in fig. 2.21.



2.21 irudia. Constant curent mode tunneling characteristics for I = 1nA and the potential barrier of eq. (2.73) with $\lambda_L = 1.0a_0^{-1}$, $\lambda_R = 1.3a_0^{-1}$, $z_L = z_R = 0$ and the gap distance dependent dynamic parameter μ of fig. 2.19, when the tunneling area is assumed to be constant and equal to 500Å. Also shown are the experimental curves of ref. 24 obtained for I = 1nA (cross points).

Nevertheless, two main discrepancies appear systematically for any value of the area and the parameters, between our one-dimensional results and the experimental curves. First of all, the first experimental peak is sharper than the theoretical one, and, second, the theoretical $dI/dV_a(V_a)$ curve is for high voltages systematically lower than the experimental one and the oscillations are more spaced in voltage; in an alike manner, the $s(V_a)$ characteristic does not fit appropriately the experimental behaviour at high voltages.

The first discrepancy can be related to the assumption made of having ideal and unrelaxed surfaces for both electrodes. As shown above, sharper peaks can be obtained at low voltages with more abrupt interface potentials; thus it may be inferred that the experimental curve could be fitted, al low voltages, by the one-dimensional results, just assuming some inwardly relaxed surface geometry for the positively biased electrode, since this kind of relaxation would increase the electron density just near the last crystal layer, this effect creating a deeper electronic potential as needed in this case.

The second discrepancy, appearing for high voltages, between the one-dimensional results and the experimental data, is related, however, to the three-dimensionality of the problem and the curvature of the tip. The analysis of this effect is the subject of the next section, where a three-dimensional calculation of the constant current mode s-V_a and dI/dV_a-V_a characteristics is presented; in this calculation we will not include any surface metal relaxation, which is assumed to be basically related to the low voltage behaviour of the conductance-voltage characteristic.

2.5. Surface geometry: three-dimensional approach

In this section we discuss a simple 3-D model, in which the tip and the sample are assumed to have spherical and planar geometry, respectively. The spherical model of the tip has been used in other theoretical approaches[33,35,36], and it is a first approximation to its real shape; in future work we will model the metals by a hyperboloidal tip and a planar base.

Let us consider a spherical tip of radius R and a planar sample, as shown in fig. 2.22, $R+s$ being the distance between the centre of the tip and the planar sample. We have the spherical tip and the planar sample at 0 and$V_a+\Delta\Phi$ potentials, respectively, V_a being the applied bias voltage and $\Delta\Phi = \Phi_L - \Phi_R$, the contact potential.

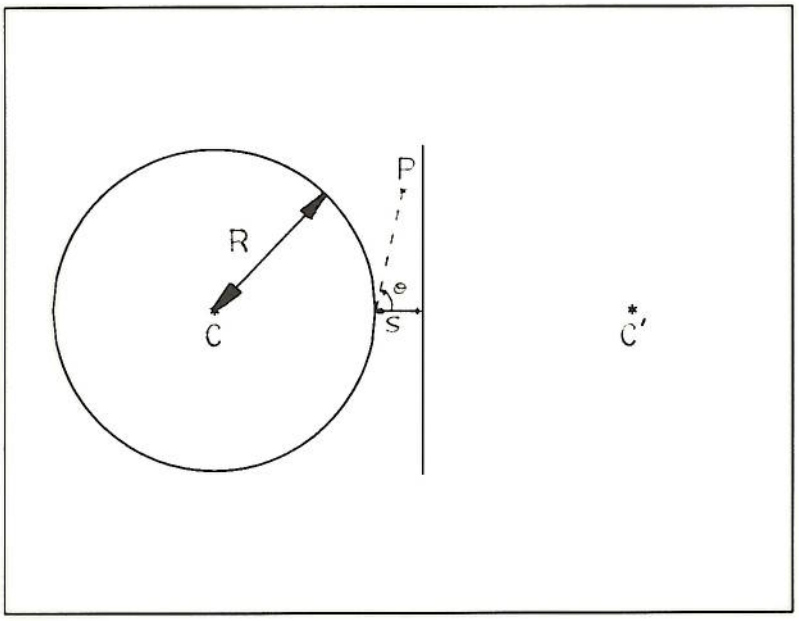


Fig. 2.22. Spherical tip of radius R and planar sample. s is the distance between the tip apex and the sample, and C' is the symetric point of C with respect to the planar sample, used as a reference point to solve the electrostatic problem.

Although it is impossible to get these two surfaces to be equipotential by an arrangement of a finite number of point charges, we may get as close an approximation to the exact solution as we wish, by taking enough of an infinite number of point charges as follows[82]

$$q_1 = (V_a + \Delta\Phi)R \quad , \quad q_i = \frac{R}{2R + 2s - d_{i-1}} q_{i-1} \tag{2.84}$$

and

$$q'_1 = -(V_a + \Delta\Phi)R \quad , \quad q'_i = \frac{R}{2R + 2s - d'_{i-1}} q'_{i-1} \quad , \tag{2.85}$$

where

$$d_1 = 0 \quad , \quad d_i = \frac{R^2}{2R + 2s - d_{i-1}} \tag{2.86}$$

and

$$d'_1 = 0 \quad , \quad d'_i = \frac{R^2}{2R + 2s - d'_{i-1}} \quad . \tag{2.87}$$

In these expressions d_i is the distance between the charge q_i and the centre C of the spherical tip, and d'_i is the distance between the charge q'_i and the point C' situated at the other side of the planar sample. Notice that the distances $d_i = d'_i$ keep smaller than R and the values $|q_i| = |q'_i|$ get smaller as the index i increases, in such a way that the effect of each succesive group of images diminishes.

Consequently, one finds for the electrostatic potential the following convergent serie:

$$V_e(r,\theta) = \sum_{i=1}^{\infty} q_i \left[\frac{1}{\left[(R - d_i)^2 + r^2 + 2(R - d_i) r\cos\theta \right]^{1/2}} - \frac{1}{\left[(R + 2s - d_i)^2 + r^2 - 2(R + 2s - d_i) r\cos\theta \right]^{1/2}} \right] \tag{2.88}$$

where q_i and d_i are given by (2.84) and (2.86), respectively. In particular, for $\theta = 0$ we have

$$V(z) = \sum_{i=1}^{\infty} q_i \left\{ \frac{1}{R + z - d_i} - \frac{1}{R + 2s - z - d_i} \right\} \tag{2.89}$$

and

$$E(z) = \sum_{i=1}^{\infty} q_i \left[\frac{1}{(R + z - d_i)^2} + \frac{1}{(R + 2s - z - d_i)^2} \right] z \quad , \tag{2.90}$$

where $z = r\cos\theta$ and z represents a unit vector normal to the planar sample.

In fig. 2.23 we have plotted the electrostatic potential of eq. (2.89), versus z, for V_a = 15V, s = 30Å and several values of the tip radius. At points close to the spherical tip the electric field is large compared to the case where both surfaces are planar, and it gets even larger as the applied voltage increases. Hence, for high voltages, the value one has to assign to

the tip-sample distance so that the electric field at the tip apex is constant increases more rapidly as the voltage increases than in the case where the tip is assumed to be planar. Consequently, when the tip is negatively biased the constant current mode tip-sample distances are, also, larger for high voltages than in the case of a planar tip, since the tunneling region appears in the high voltage range close to the negatively biased electrode; thus the constant current mode $s(V_a)$ curve will feature a bending up, which is an effect observed in the experiment.

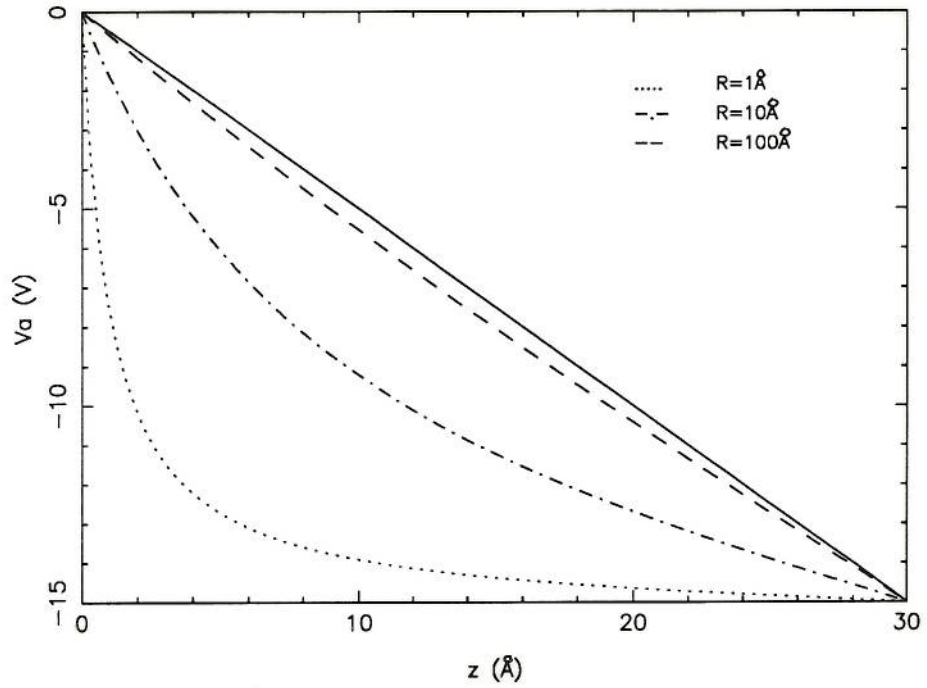


Fig. 2.23. Electrostatic potential along the axis between the tip and the sample ($\theta = 0$), as a function of coordinate z, for different values of the tip radius. The solid line represents the electrostatic potential between two conducting planes.

If the tip were made positive with respect to the sample, in such a way that electrons move from the planar sample towards the spherical tip, the tunneling region would appear, for high voltages, close to the sample surface, and the constant current mode $s(V_a)$ curve would feature a bending down, though in this case the effect of the curvature of the tip would be less important.

In order to have a simple idea of the role played by the geometry, we argue in the following way: For high voltages ($V_a > \Phi_R$) we are in the field emission regime and the current is controlled approximately just by the electric field; consequently, assuming that the

tunneling effective area remains constant (this approximation will be improved later on) and noticing that when the tip is negatively biased tunneling electrons are mostly crossing the interface from the tip apex, the constant current mode $s(V_a)$ curve can be determined approximately, for high voltages, by imposing the condition of constant electric field at the tip apex. Fig. 2.24 exhibits the calculated constant electric field mode distance-voltage characteristic for an electric field of 0.6eV/Å and several values of the tip radius.

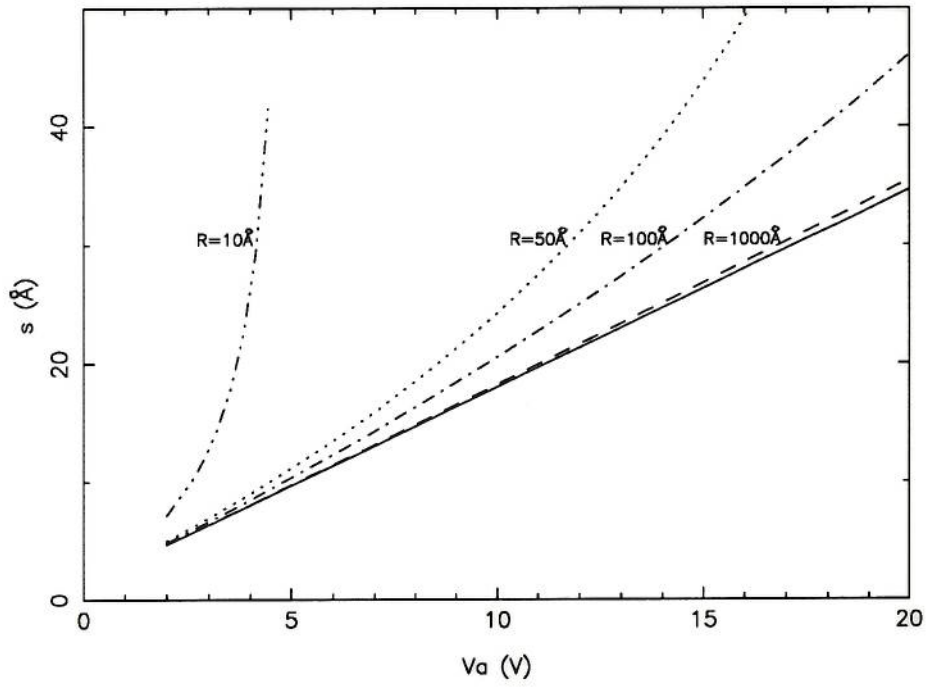


Fig. 2.24. Calculated s-V_a characteristics making the electric field at the tip apex constant and equal to 0.6eV/Å, for a planar tip (solid curve) and for different values of the radius of a spherical tip (dashed, dashed-dotted, dotted and dashed-dotted-dotted-dotted curves).

The results of fig. 2.24 show that the $s(V_a)$ curves are dramatically dependent on the tip radius, and comparing with the experimental data of ref. 24 one finds that the bending up of the experimental curve is similar to the one found in our calculations of fig. 2.24 for R ≈ 100Å. This is a very elementary argument to determine the tip radius, as we will see below; however, it shows the main effect that we will proceed now to analyse more carefully.

Effective tunneling area

For a given tip-sample configuration, the equipotential surfaces may be calculated numerically from eq. (2.88), searching for the zeros of a function of one variable. On the other hand, the electric field lines may also be calculated, derivating eq. (2.88) and solving the corresponding differential equations of first order. Fig. 2.25 shows some equipotential surfaces and electric field lines computed in the field emission regime for V_a = 15V, s = 30Å and R = 100Å, when the tip is negatively biased (fig. 2.25a) and when it is positively biased (fig. 2.25b). The equipotential surface S_F with potential equalling the Fermi level of the negatively biased electrode is also shown in this figure; this surface divides, neglecting image force effects, the tunneling region, that is, the classically forbidden part of the vacuum gap, from the positive kinetic energy region of Fermi electrons.

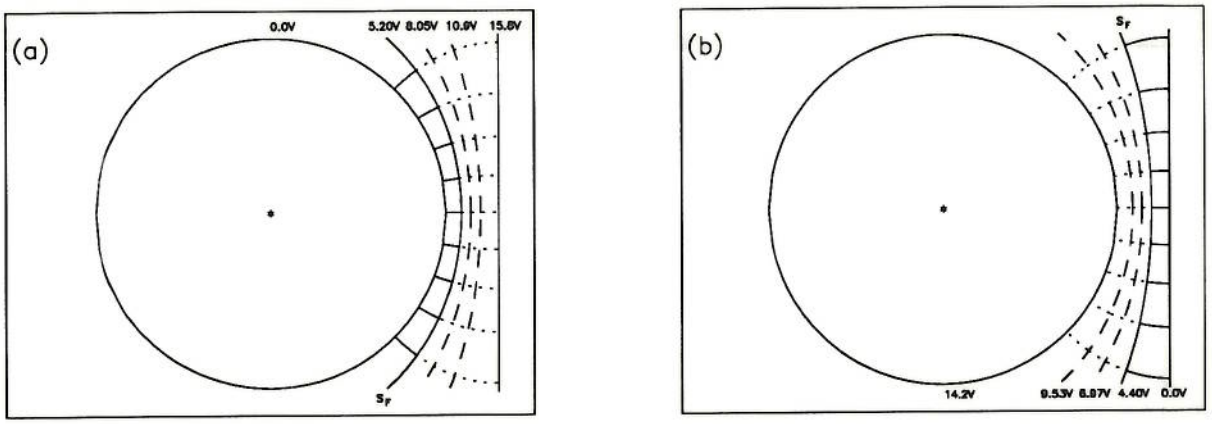


Fig. 2.25. Equipotential surfaces and electric field lines for a planar sample and a spherical tip of radius equal to 100Å, when the tip is negatively biased (fig. 2.25a) and when it is positively biased (fig. 2.25b). The equipotential surface where the electrostatic potential equals the Fermi level of the negatively biased electrode, S_F, is represented by a solid curve. The field lines are represented by solid curves along the tunneling region, and by dotted curves along the positive kinetic energy part of the vacuum gap; the tunneling region, that is, the negative kinetic energy region of Fermi electrons is defined, neglecting image forces, by S_F and the negatively biased electrode´s surface. The numbers in the upper part and in the base of the figure represent the potential values corresponding to the negatively biased tip and the positively biased tip, respectively; the potential difference between tip and sample changes when the sign of the applied voltage is changed, because of the difference between work functions. Applied voltage, tip-sample distance and tip radius have been taken to be V_a = 15V, s = 30Å and R = 100Å .

Notice that there is an asymmetry in the problem, associated to the two very different tunneling regions. In the field emission regime the tunneling current is approximately a function of the electric field alone, as pointed out above, so that the width of the tunneling region happens to be almost constant in the constant current mode and is at high voltages much less than the actual tip-sample separations; therefore, the equipotential surface dividing the tunneling region from the positive kinetic energy region of the vacuum gap becomes more and more bent towards the negatively biased electrode as the voltage increases in the constant current mode, no matter what the sign of the applied voltage is, and the effective area gets larger. However, since the S_F equipotential surface gets in the high voltage regime very close to the negatively biased electrode, when the tip is positively biased the tip asperities should play a minor role, with the implications that will be discussesd below.

In a semi-classical picture electrons must move along the electric field lines, in such a way that the maximum tunneling probability appears for electrons leaving the tip apex and this probability decreases as we move from this point. As the tunneling probability decreases very quickly with the tunneling barrier width, we can expect the effective tunneling area to be reduced to a small area around the tip apex; moreover, it can be expected from the above discussion to increase with the applied voltage.

The effective tunneling area can be defined integrating over the equipotential surface S_F as follows

$$A_{\text{eff}} = \frac{1}{J_0} \int_{S_F} dS\, J(\boldsymbol{r}) \quad , \tag{2.91}$$

where $J(\boldsymbol{r})$ represents the current density of electrons arriving at $\mathbf{r}$ in the equipotential surface S_F, J_0 being the current density of electrons tunneling along the axis between the electrodes. Using polar coordinates, one can write

$$A_{\text{eff}} = \frac{2\pi}{J\left[r(0),0\right]} \int_0^{\pi} d\theta \sqrt{\left[r(\theta)\right]^2 + \left[dr/d\theta\right]^2}\; r(\theta) \sin\theta\; J\left[r(\theta),\theta\right] \quad , \tag{2.92}$$

where $r=r(\theta)$ represents the equipotential surface S_F.

If the WKB approximation is used to evaluate electron tunneling probabilities, for tip-sample distances of interest here the tunneling current density can be obtained from eq.

(2.20). The mean barrier height and the tunneling barrier width for electrons arriving at (r,θ) in the equipotential surface S_F can be calculated in the following way:

$$\bar{\Phi}\left[r(\theta),\theta\right]=\frac{1}{\Delta s\left[r(\theta),\theta\right]}\int_{r_0(\theta)}^{r(\theta)} dr' \sqrt{1+r'^2\left[d\theta'/dr'\right]^2}\;\; \varphi\left[r',\theta'(r')\right] \qquad (2.93)$$

and

$$\Delta s\left[r(\theta),\theta\right]=\int_{r_0(\theta)}^{r(\theta)} dr' \sqrt{1+r'^2\left[d\theta'/dr'\right]^2}\quad , \qquad (2.94)$$

respectively, where

$$\varphi(r,\theta)=V_e(r,\theta)-\Phi_L\quad , \qquad (2.95)$$

if image force effects are neglected. In these expressions $V_e(r,\theta)$ is given by (2.88), and $r_0(\theta)$ represents the polar coordinate r of the intersection point between the negatively biased electrode surface and the electric field line $\theta' = \theta'(r')$ arriving at θ in the equipotential surface S_F. The mean barrier height does not change appreciably with θ; however, the tunneling barrier width changes strongly with θ, especially at low voltages. Fig. 2.26 exhibits the tunneling barrier width as a function of the polar coordinate θ, for V_a = 15V, s = 30Å and R = 100Å.

Fig. 2.27 illustrates how the effective area defined by means of eq. (2.92) changes for a negatively biased tip, for different values of the tip radius ranging from 100 to 200Å; in this calculation, the constant current density mode tip-sample distance has been considered for each value of the applied voltage. It is obvious from this figure that for small voltages the area is practically constant, as we expected, but it increases very rapidly for voltages larger than the work function of the positively biased electrode, as we have already discussed above.

The results of fig. 2.27 show that the effective tunneling area cannot be assumed to be constant, so that the tunneling current density is no longer constant in the constant current mode, neither is the electric field at the negatively biased electrode, not even at high voltages; the results of fig. 2.24 must, therefore, be reconsidered: For each value of the tunneling effective area and tip radius we have estimated the electric field at the tip apex for which the tunneling current would be in the high voltage range equal to 1nA; then we have calculated the

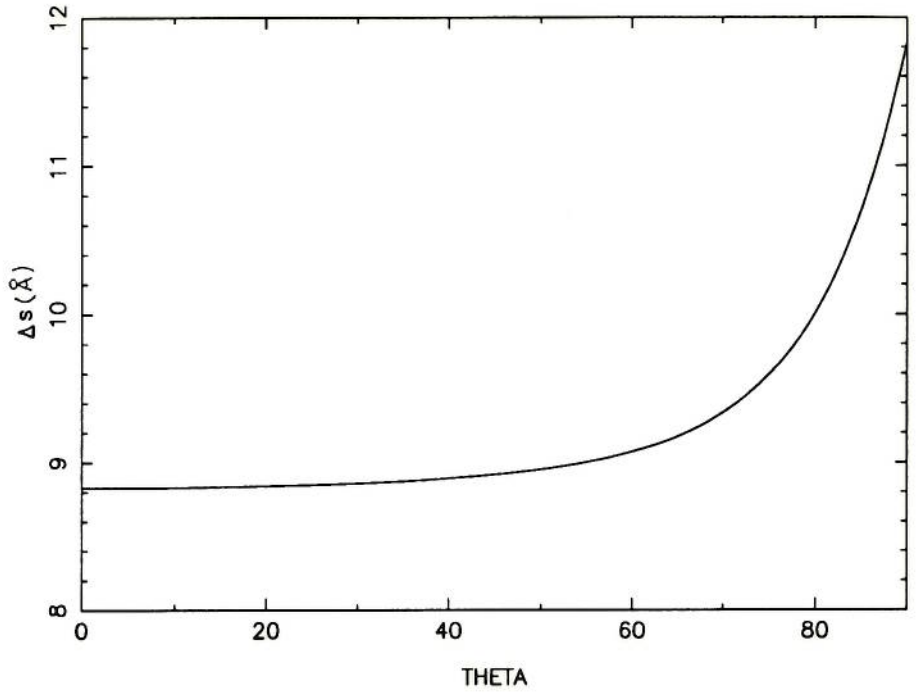


Fig. 2.26. Tunneling barrier width defined by means of eq. (2.94), as a function of the polar coordinate θ. The tip has been assumed to be negatively biased, and applied voltage, tip-sample distance and tip radius have been taken to be $V_a = 15$V, $s = 30$Å and $R = 100$Å, respectively.

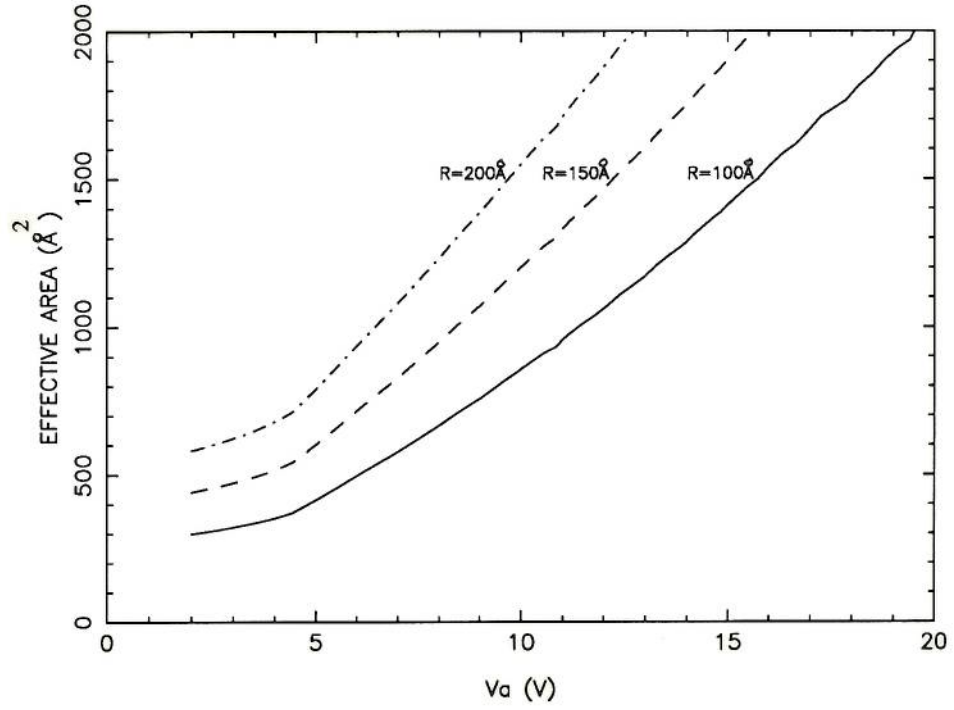


Fig. 2.27. Effective tunneling area calculated from eq. (2.92), as a function of the applied voltage, for tip radius of 100Å (solid curve), 150Å (dashed curve) and 200Å (dashed-dotted curve). The tip has been assumed to be negatively biased, and the constant current density mode tip-sample distance has been considered for each value of the applied voltage.

$s(V_a)$ curve making the electric field at the tip apex to vary in accordance to the dependence of the tunneling effective area on the applied voltage exhibited in fig. 2.27. The results obtained in this way are presented in fig 2.28; comparing the results of this figure with the experimental curve given in ref. 24, one finds that the bending up of the experimental curve is very similar to the calculated one when the tip radius is assumed to be R ≈ 150Å.

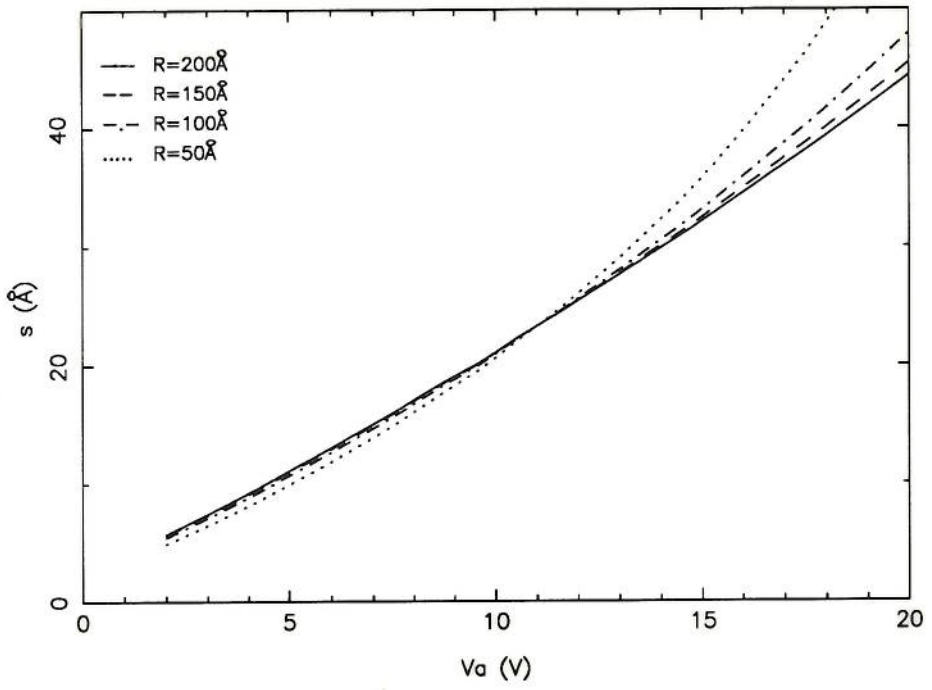


Fig. 2.28. s-V_a characteristics making the electric field at the tip apex to vary, as the applied voltage changes, according to the dependence of the tunneling effective area on the applied voltage represented in fig. 2.27, for different tip radius ranging from 50 to 200Å.

However, the effective area of fig. 2.27 should also be reconsidered, since in this calculation for each value of the applied voltage the constant current mode tip-sample distance should be taken, rather than the constant current density mode tip-sample distance taken there. Therefore, as the constant current mode tip-sample distance depends, at the same time, on the effective area, both quantities must be evaluated self-consistently. This point is discussed in the next section, introducing an analysis of the tunneling current calculation through the barrier.

Tunneling characteristics: s-V_a and dI/dV_a-V_a

First of all we calculate, using eq. (2.9), the tunneling current density across the potential barrier of eq. (2.73) with the electrostatic potential $V_e(z)$ of eq. (2.89). We assume a given tip radius, applied voltage and tip-sample distance, and consider tunneling along the axis between the electrodes. The quantities A_L, B_L, A_R and B_R determined by matching the potential and its derivative at the positions of the image planes

$$A_{L,R} = \frac{-4\,U_{L,R}}{\lambda_{L,R} + \left[1 - \mu - \exp(-\lambda_{R,L}\,d)\right]/d - 4\,V_e(z'_{L,R})} - 1 \qquad (2.96)$$

and

$$B_{L,R} = \frac{(A_{L,R}+1)^2}{A_{L,R}} \frac{\lambda_{L,R}^2/2 - \left[1 - \mu - (1 + \lambda_{R,L}\,d)\exp(-\lambda_{R,L}\,d)\right]/d^2 \pm 4\,V'_e(z'_{L,R})}{-4\,U_{L,R}} , \qquad (2.97)$$

where the notation "±" means that when B_L is to be calculated "+" must be used, and "-" must be used when B_R is to be calculated, and

$$\begin{aligned} z_L' &= z_L \\ z_R' &= s - z_R \ . \end{aligned} \qquad (2.98)$$

In fig. 2.29 we have plotted this potential barrier for forward and reverse bias and compared it to the corresponding barrier between two planar electrodes; it is worth mentioning that at high voltages the tunneling region area is close to the negatively biased electrode, thus the effect of the curvature on the tunneling current density being more important when the tip is negatively biased, as can be inferred from this figure.

Secondly, for the same values of the tip radius, applied voltage and tip-sample distance we determine the equipotential surfaces and the electric field lines, and calculate the effective tunneling area integrating over the equipotential surface S_F by means of eq. (2.92). Then we calculate the total tunneling current as the product of the effective area and the current density of electrons tunneling along the axis between the electrodes.

Finally, for a given tip radius and applied voltage we search for the tip-sample distance making constant the total tunneling current. Once we have determined for a given geometry, total current and applied voltage the constant current mode tip-sample distance, we proceed to

calculate the constant current mode distance-voltage characteristics; then we evaluate numerically, along the calculated constant current mode $s(V_a)$ curve, the constant current mode conductance, dI/dV_a-V_a, as a function of V_a, evaluating for each value of the applied voltage and tip-sample distance the effective area specified by eq. (2.92).

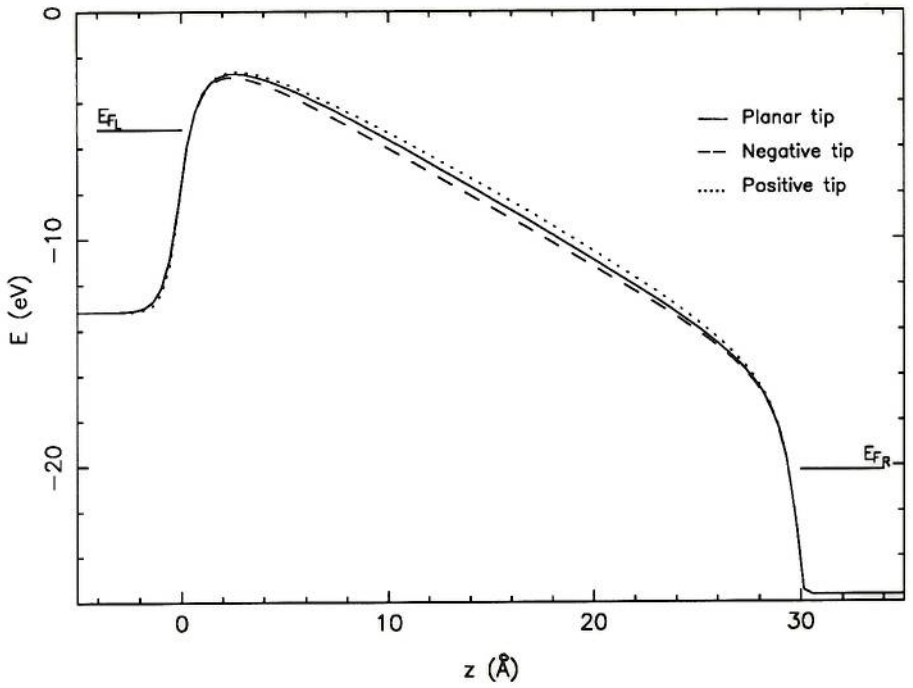


Fig. 2.29. Potential barrier of eq. (2.73) with the electrostatic potential of eq. (2.89), when the tip is taken to be negatively biased (dashed line) and when it is taken to be positively biased (dotted line); the solid line represents the corresponding model potential between two planar electrodes. The barrier parameters have been taken to be $\lambda_L = 1.0a_0^{-1}$, $\lambda_R = 1.3a_0^{-1}$, $\mu = 1.0$ and $z_L = z_R = 0$, and $\Phi_L = 5.2$eV, $\Phi_R = 4.4$eV, $U_L = 13.2$eV, $U_R = 9.9$eV, R=150Å, $V_a = 15$V and $s = 30$Å.

We have determined the constant current mode s-V_a and dI/dV_a-V_a characteristics for I = 1nA and several values of the tip radius. Our first aim has been to determine the radius of the tip sphere yielding a good agreement between our calculations and the experimental data given by Becker et al[24] , and we have found that a radius of 150Å yields the best agreement, although differences of 25Å do not introduce important modifications to our results. Figs. 2.30 and 2.31 show the s-V_a and dI/dV_a-V_a characteristics calculated for I = 1nA and a spherical tip with radius of 150Å, together with the available experimental data obtained when the tip is negatively biased[24] and when it is positively biased[83].

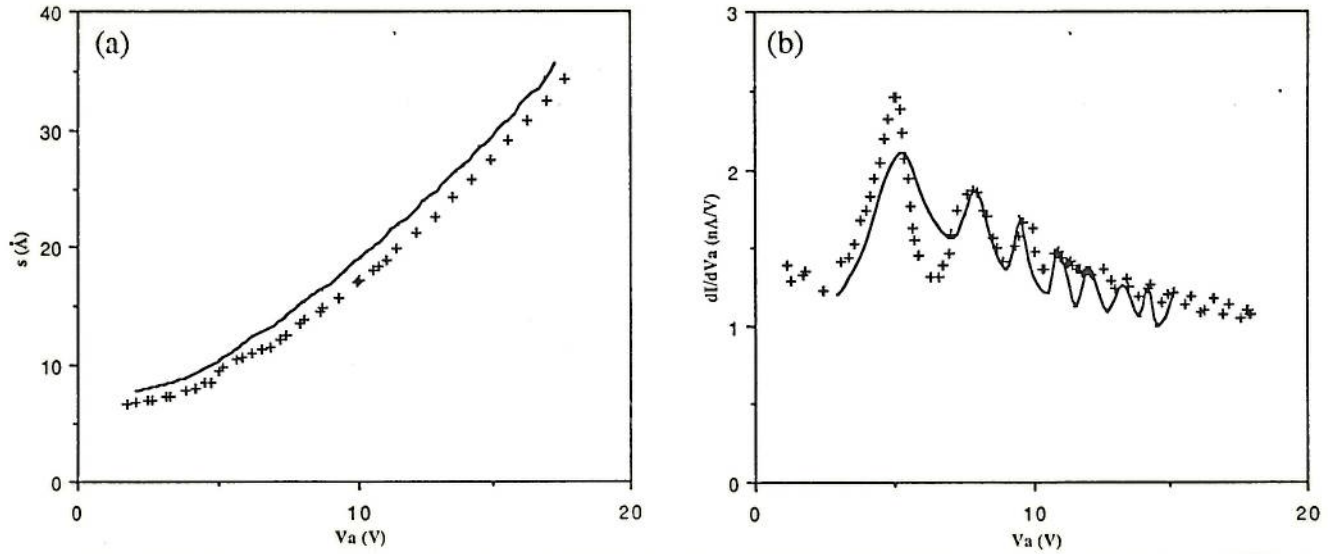


Fig. 2.30. Constant current mode s-V_a and dI/dV_a-V_a characteristics calculated as explained in the text, for I = 1nA and a negatively biased tip of radius R = 150Å, with $\lambda_L = 1.0a_0^{-1}$, $\lambda_R = 1.3a_0^{-1}$, the gap distance dependent dynamic parameter μ of fig. 2.19, z_L =-0.8Å and z_R = -0.2Å. Also shown are the experimental curves of ref. 24 (cross points), which have been obtained for I = 1nA.

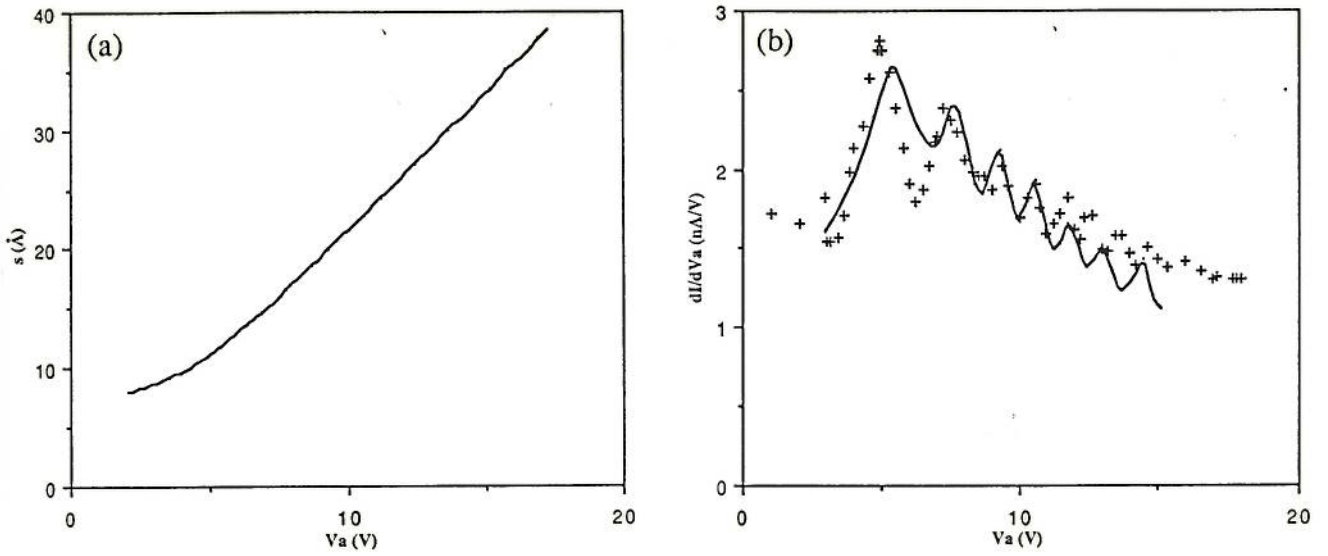


Fig. 2.31. As in fig. 2.30, but for a positively biased tip of radius R = 15Å. Here only the dI/dV_a-V_a experimental curve obtained for I = 1nA is presented[83] (cross points), since the experimental s-V_a curve is not available now.

In figs. 2.30 and 2.31 the barrier parameters $\lambda_L = 1.0a_0^{-1}$ and $\lambda_R = 1.3a_0^{-1}$ and the gap distance dependent dynamic parameter μ of fig. 2.19 have been considered. On the other hand, the aim of fitting both experimental data obtained for forward and reverse bias has led us to choose z_L = -0.8Å and z_R = -0.2Å; the negative values of these parameters are consistent

with the d-band character of W and Au, which will tend to displace the centroid of the induced density towards the material, compared with the results of the jellium model.

The agreement between the theoretical and experimental values of the s-V_a characteristics of fig. 2.30 is very good; the displacement between both curves is not significative, since experimentally it is not possible to place the tip-sample distance origin accurately so that the experimental data only give a measure of change in tip position[24]. This agreement shows that the three-dimensional effects discussed above are necessary to explain the high voltage behaviour of the s-V_a characteristics. Moreover, the analysis allows us to deduce the microscopic tip radius of curvature.

Good agreement is also found for the dI/dV_a-V_a characteristics obtained when the tip is taken to be negatively biased, although some discrepancies appear around the first oscillation of this curve; as discussed above, this is probably due to some possible relaxation of the sample surface. At high voltages we find, however, that the calculated oscillations of the $dI/dV_a(V_a)$ curve are a little damped in the experimental curve; this damping may be due to the asperities of the tip that tend to produce interferences among different parts protruding more or less from the mean tip surface, as argued by Bono and Good[28]. It is interesting to remark that the effect of the interferences among the different parts of the tip should disappear for the opposite bias, a positive tip bias, since in this case the tunneling region is at high voltages close to the sample surface, as discussed above (see fig. 2.25), and tip asperities play minor roles in the tunneling process; indeed, the experimental results obtained when the tip is positively biased[83] (see fig. 2.31b) show at high voltages sharper peaks than when the tip is negatively biased.

When the tip is taken to be positively biased, the calculated $dI/dV_a(V_a)$ curve is at high voltages lower than the experimental one and the oscillations are more spaced in voltage, showing that the calculated constant current mode tip-sample distance gets at high voltages smaller than the experimental one. The agreement between the theoretical and experimental curves obtained with this polarization of the applied voltage would be better if larger values of the tip radius were considered in our calculations; this result may be understood assuming that the tip radius may not be the same in both experiments.

In conclusion, it has been found that a reasonable fit to the interface potential can be made using the improved model potential of eq. (2.73), by a trial and error process to reproduce the experimentally determined s-V_a and dI/dV_a-V_a characteristics, which allows the tip radius to be determined and demonstrates the importance of taking into account the 3D tip-sample geometry in explaining the high voltage behaviour of the tunneling characteristics.

2.6.Apparent barrier height

In the preceeding sections it has been shown that the scanning tunneling microscope happens to be a useful tool not only to obtain topographic images of surfaces but also to provide a measure of the potential barrier that electrons feel when tunneling between two solids, if the constant current mode s-V_a and dI/dV_a-V_a characteristics are measured in the field emission regime. In this section we consider experiments made at very small voltages ($V_a << 1V$) when the tip is displaced in the perpendicular direction to the surface keeping either I or V_a constant, since in this mode the tunneling barrier height is measured directly.

On very general grounds one can write the microscope tunneling current, at small bias, as[42]

$$I = V_a\, k(s)\, e^{-2\sqrt{2\bar{\Phi}}\, s} \quad , \tag{2.99}$$

where V_a is the applied voltage, s the tip-sample distance, $\bar{\Phi}$ the mean tunneling barrier, and $k(s)$ a function of s. This equation suggests that an apparent barrier height can be defined as

$$\Phi_{ap} = \frac{1}{8}\left[d(\ln I) / ds \right]^2_{V_a} \tag{2.100}$$

or

$$\Phi_{ap} = \frac{1}{8}\left[d(\ln V_a) / ds \right]^2_{I} \quad , \tag{2.101}$$

since it should coincide with the mean tunneling barrier if the dependence on s of Φ and the pre-exponential factor in eq. (2.99) could be neglected. It is worth to remark that if V_a is assumed to be small enough, eqs. (2.100) and (2.101) yield the same value for the apparent barrier height, as it has already been shown by Coombs et al[84], since at very small voltages one finds

$$\frac{\left[d(\ln I) / ds \right]_{V_a}}{\left[d(\ln V_a) / ds \right]_{I}} = - \frac{\left[dI / dV_a \right]_{s}}{I / V_a} \quad . \tag{2.102}$$

Nevertheless, it is well known that the apparent barrier height, as measured with the STM, is practically independent of the tip-sample separation and approximately equal to the

average work function of the two solids over a long range of tip-sample distances[11,21], while the image potential and the local exchange and correlation effects tend to reduce drastically the interface barrier.

Binnig, García, Rohrer, Soler and Flores[21] have shown that these experiments are consistent with the existence of the image potential and have stated that a reduction in the actual barrier height inversly proportional to the tip-sample separation due to image force effects leads to apparent barrier heights very close to the work function, even at separations where the reduction in the actual barrier height is important. Coombs, Welland and Pethica[84], using a similar argument have stated that the image potential has no effect on the apparent barrier height, concluding that measurements of the conductance as a function of tip-sample separation is not a sensitive method for observing the image potential. Lang[81], arguing that the image contributions to the apparent barrier height can be neglected and, hence, that the failure of the local density approximation to give an image contribution to the potential far outside does not represent a problem in this case, has employed the local density approximation to calculate the apparent barrier height; surprisingly, he has found that the apparent barrier height goes for large tip-sample separations above the average work function. On the other hand, Payne and Inkson[85] have concluded that the image potential leads to an observable difference in apparent barrier heights as deduced from eqs. (2.100) and (2.101), which is in contradiction with eq. (2.102).

In this section we clarify the existing controversy about the contribution of the image potential to measurements of the apparent barrier height, demonstrate that the image potential play an important role in lowering the apparent barrier height and give new arguments showing why the apparent barrier height is so much constant over such a long range of tip-sample separations, as experiments show. We also present specific results for the apparent barrier height, calculated for different simple model barriers and the parametrized potential barrier of eq. (2.73), which introduces both image force and exchange-correlation effects and gives an appropriate description of the actual barrier height that electrons see when tunneling between two metals.

The calculations presented in this section have been obtained assuming planar parallel

metallic electrodes with Fermi energies of 8.0 and 5.5eV and work functions of 4.8eV.

General considerations

In order to examine the reliability of the mean barrier approximations discussed in section 2.1, which are still used to interpret STM experiments, first of all we have calculated for very small voltages the tunneling current densities through an image reduced classical barrier with the image potential approximated by the formula of Simmons, i.e. (2.66), by means of eqs. (2.23), (2.24) and (2.25), and also integrating numerically the Schrödinger equation and then integrating over all allowed energies by means of eq. (2.9). We have found that eq. (2.23), which is obtained in the MBA approximation, overestimates the tunneling current density, as already shown by Miskovsky et al[49], especially for small tip-sample separations, showing that the derivative with separation of the current density at constant applied voltage is also overestimated thus predicting too large apparent barrier heights. On the other hand, eqs. (2.24) and (2.25), which are both obtained in the SBA approximation, give for small tip-sample separations different current densities: eq. (2.24) underestimates the current density and eq. (2.25) overestimates it, especially for small tip-sample separations, thus predicting different apparent barrier heights.

Fig. 2.32 shows the apparent barrier height computed numerically from eq. (2.100) when the exact result for the tunneling current density is considered by means of eq. (2.9), and also when the approximated formulas (2.23), (2.24) and (2.25) are considered. It is obvious from this figure that for small interelectrode separations (s < 10Å) the mean barrier approximations lead to apparent barrier heights in poor agreement with the exact results, although for large separations these approximations lead to the correct behaviour of the apparent barrier height: it is almost constant and equal to the average work function of the electrodes, even for separations where the image potential reduces importantly the maximum and mean barrier heights. It is worth mentioning, also, that for very low voltages eqs. (2.20) and (2.23) lead both to the same apparent barrier height, as well as eqs. (2.21) and (2.24); on

the other hand, for low voltages the effective barrier height defined by eq. (2.26) is very similar to the mean barrier height of eq. (2.19), thus eqs. (2.23) and (2.30) leading to similar apparent barrier heights.

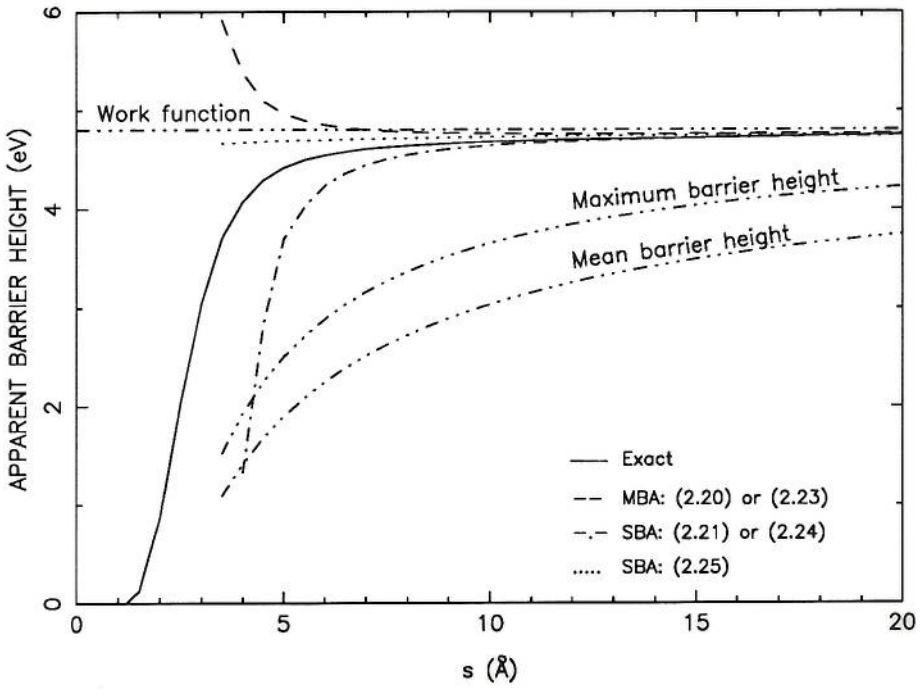


Fig. 2.32. Apparent barrier height deduced from eq. (2.100), as a function of tip-sample distance, when Simmons approximation to the image reduced potential barrier is used and the tunneling current density is calculated by means of eq. (2.9) after having solved numerically the Schrödinger equation (solid curve) or by means of different mean barrier approximations, i.e. eqs. (2.23) (dashed curve), (2.24) (dashed-dotted curve) and (2.25) (dotted curve). The average work function, the maximum barrier height and the mean barrier height are also given, for comparison.

Payne and Inkson[85] have used eq. (2.21), which is obtained in the SBA approximation, to calculate the tunneling current density through the image reduced potential barrier of Simmons. When the current density so obtained is introduced into eq. (2.100) the apparent barrier height represented in fig. 2.32 by a dashed-dotted curve is obtained. On the other hand, the apparent barrier height can also be obtained in terms of a derivative with separation of the bias voltage at constant current, whenever the voltage keeps very small ($V_a << 1V$), by means of eq. (2.101). Thus we have performed calculations of the constant current density mode $\ln V_a$ - s characteristics, for several values of the current density measured in A/cm^2, and plotted

them in fig. 2.33. In order to obtain the correct behaviour of the apparent barrier height, independently of the bias voltage, this must be very small; consequently, for each value of the tip-sample separation we have considered constant current densities for which $V_a < 0.1$V, in such a way that as the separation increases smaller constant current densities must be considered. The results deduced in this way from eq. (2.101), deriving numerically the $\ln V_a(s)$ curves of fig. 2.33, are plotted in fig. 2.34 as a function of separation; this figure also indicates which $\ln V_a$ - s characteristic has been derived in our calculation. As we expected, the results of fig. 2.34 are independent of the value of the constant current density, whenever the bias voltage is very small ($V_a < 0.1$V). Finally, let us notice that the apparent barrier height of fig. 2.34 is exactly the same as the one represented in fig. 2.32 by a dashed-dotted curve, both obtained using eq. (2.21) to calculate the current density: the apparent barrier height gets smaller as the separation decreases, although it keeps almost constant and equal to the work function of the electrodes for intermediate and large separations.

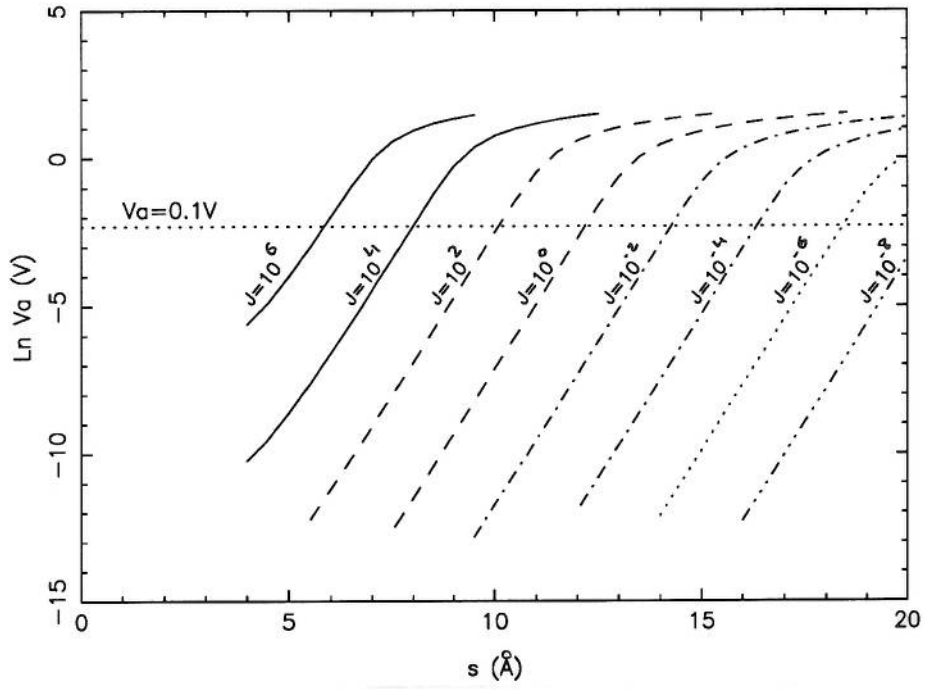


Fig. 2.33. Natural logarithm of the constant current density mode applied voltage, versus the interelectrode separation, deduced solving eq. (2.21) when the image potential is included by means of the approximate formula of Simmons, i.e. eq. (2.66), for different values of the current density J measured in A/cm^2. The dotted horizontal line represents an applied voltage of 0.1V.

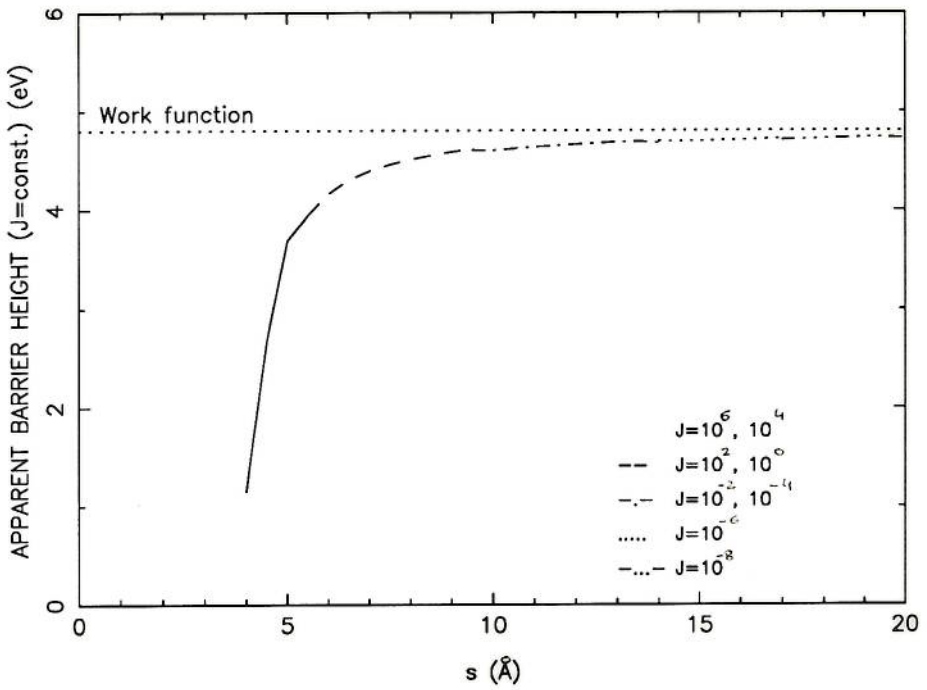


Fig. 2.34. Apparent barrier height, as a function of the interelectrode separation, deduced from eq. (2.101) derivating the constant current density mode $\ln V_a(s)$ curves of fig. 2.33 in the applied voltage range of 10^{-3}V < V_a < 10^{-1}V. Different line types show which curve of fig. 2.33 has been derivated.

However, Payne and Inkson[85] have concluded that the apparent barrier height measured at constant voltage is approximately equal to the work function, while the apparent barrier height measured at constant current yield lower values; this conclusion is just a consequence of having considered the constant voltage mode $\ln J$ - s and the constant current density mode $\ln V_a$- s characteristics in different ranges of the interelectrode separation.

On the other hand, Coombs, Welland and Phetica[84] have concluded that the apparent barrier height is extremly close to the unreduced work function, even for s = 3Å, since they have used eq. (2.25) rather than (2.21) or (2.24) to calculate the tunneling current density through the approximate image reduced potential barrier of Simmons thus obtaining the dotted curve of fig. 2.32.

In order to give new arguments showing why the apparent barrier height is over a long range of tip-sample separations very close to the work function even at separations where the reduction in the actual barrier height is important, first of all we use the MBA approximation to calculate tunneling current densities, which leads for large separations ($s \gtrsim 10$Å) to the correct behaviour of the apparent barrier height, as shown in fig 2.32.

Mean barrier approximation

Combining eqs. (2.23) and (2.100) we find the apparent barrier height as

$$\Phi_{ap} = \left\{ -(\bar{\Phi}^{1/2}\,\Delta s)\left[1+\frac{1}{\alpha\,\bar{\Phi}^{1/2}\,\Delta s\,(1+\alpha\,\bar{\Phi}^{1/2}\Delta s)}\right]-\frac{\Delta s'}{\alpha\,\Delta s}+\frac{\bar{\Phi}}{2\,\alpha\,\bar{\Phi}}\right\}^2, \quad (2.103)$$

where $\bar{\Phi}$ represents the mean barrier height of eq. (2.18); the quantity Δs represents the tunneling barrier width of Fermi electrons, that is, the distance between the classical turning points at the Fermi level, and

$$\alpha = 2\sqrt{2} \quad , \quad (2.104)$$

since in the low voltage range β as defined in eq. (2.31) takes the value unity[45].

Now we consider the image reduced potential barrier of eq. (2.67) with the following approximations of the image potential:

$$\text{a) } V_{im}(z) = 0 \quad , \quad (2.105)$$

$$\text{b) } V_{im}(z) = -\frac{C}{s} \quad (2.106)$$

and

$$\text{c) } V_{im}(z) = -\frac{C\,s}{4\,z\,(s-z)} \quad . \quad (2.107)$$

where C is a constant. These approximated image reduced potential barriers are represented in fig. 2.35 for C = 1.15 ln 2.

In case (a), that is, when the image potential is not included, the tunneling barrier width is equal to the tip-sample separation and the mean barrier height coincides with the average work function. Consequently, provided that the applied voltage is very small we find

$$\Phi_{ap} = \left\{ \Phi_0^{1/2}\left[1+\frac{1}{\alpha\,\Phi_0^{1/2}s\,(1+\alpha\,\Phi_0^{1/2}s)}\right]+\frac{1}{\alpha\,s}\right\}^2 \quad , \quad (2.108)$$

where Φ_0 is the average work function

$$\Phi_0 = \frac{\Phi_L + \Phi_R}{2} \quad . \quad (2.109)$$

In particular, when $s > 1/\Phi_0$ (for typical work functions $1/\Phi_0 \approx 3$Å), eq. (2.108) can be expanded as

$$\Phi_{ap} = \Phi_0 \left\{ 1 + 2\,\alpha^{-1}\,\Phi_0^{1/2}\,(\Phi_0\,s)^{-1} + O\left[(\Phi_0\,s)^{-2}\right] \right\} . \qquad (2.110)$$

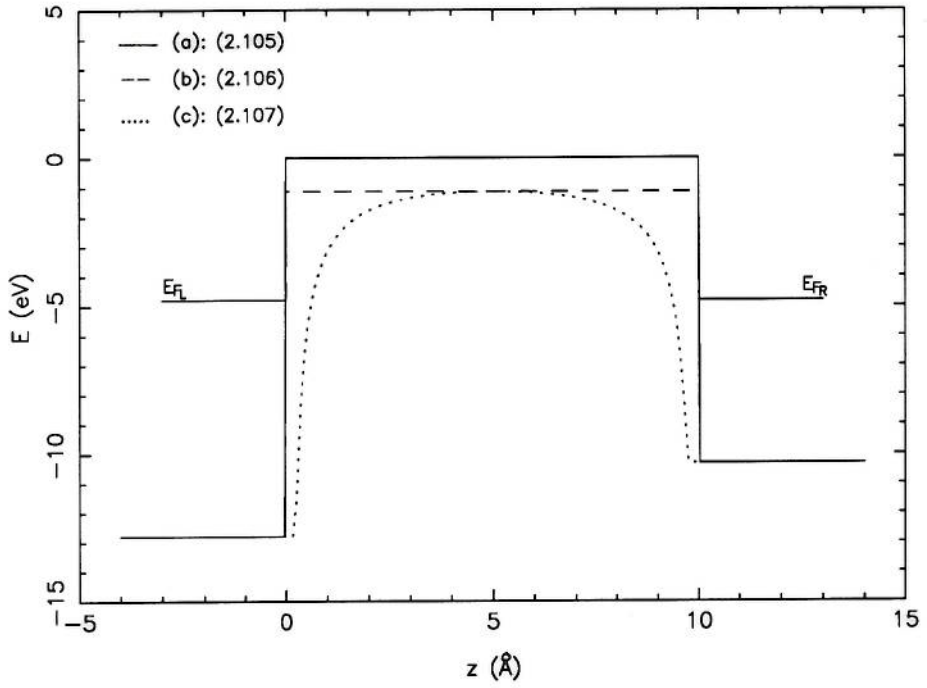


Fig. 2.35. Model potential barriers for very small applied voltages: (a) Square potential barrier of height equal to the average work function (solid line), (b) lowered square potential barrier tangent to the approximated image reduced potential barrier of Simmons, and (c) approximated image reduced potential barrier of Simmons. In this figure the constant C has been taken to be 1.15 ln2, thus the approximation (2.107) to the image potential being equal to the Simmons approximation.

Notice that for the simplest case of an unreduced square barrier the contribution to the apparent barrier height from the s-dependent part of the pre-exponential factor of eq. (2.23) is of first order in $(\Phi_0\,s)^{-1}$, in such a way that the apparent barrier height approaches the average work function from above for very large separations, as it has been already pointed out by Lang[81]. It is worth mentioning that this s-dependent pre-exponential factor in the current density comes from the contribution to the total current density due to electrons with E_z component of the energy smaller than the Fermi energy; since this contribution happens to be more important as the interelectrode separation decreases, the current density gets comparatively larger for small separations and the apparent barrier height gets larger than the

average work function. Accordingly, if tunneling electrons did not feel an image potential, the measured apparent barrier height would appreciably differ from the average work function at tip-sample separations commonly used in STM.

In case (b), that is, when the image reduced barrier is approximated by a lowered squared barrier, the tunneling barrier width is also equal to the tip-sample separation and the mean barrier height is given, for low voltages, by the following expression:

$$\bar{\Phi} = \Phi_0 - \frac{C}{s} \quad , \tag{2.111}$$

where C is equal to ln 2, 1 or 1.15 ln 2, depending on weather the potential barrier is taken to be tangent to the image reduced barrier with the image potential specified by eqs. (2.64), (2.65) or (2.66), respectively. Hence, one finds

$$\left(\bar{\Phi}^{1/2}\,\Delta s\right)' = \bar{\Phi}^{1/2}\left(1 + \frac{1}{2}\frac{C}{\bar{\Phi} s}\right) \tag{2.112}$$

and

$$\frac{\Delta s'}{\Delta s} - \frac{1}{2}\frac{\bar{\Phi}'}{\bar{\Phi}} = \frac{1}{s} - \frac{1}{2}\frac{C}{\bar{\Phi} s^2} \quad . \tag{2.113}$$

Thus combining eqs. (2.103), (2.112) and (2.113) we find, provided that the applied voltage is very small, the apparent barrier height as

$$\Phi_{ap} = \left\{ \bar{\Phi}^{1/2}\left(1 + \frac{1}{2}\frac{C}{\bar{\Phi} s}\right)\left[1 + \frac{1}{\alpha\,\bar{\Phi}^{1/2} s\,(1 + \alpha\,\bar{\Phi}^{1/2} s)}\right] + \frac{1}{\alpha s}\left(1 - \frac{1}{2}\frac{C}{\bar{\Phi} s}\right) \right\}^2 , \tag{2.114}$$

where $\bar{\Phi}$ is given by eq. (2.111), as a function of interelectrode separation.

It is interesting to notice that when $s > 1/\Phi_0$ eq. (2.114) may be expanded giving eq. (2.110), since

$$\bar{\Phi}^{1/2}\left(1 + \frac{1}{2}\frac{C}{\bar{\Phi} s}\right) = \Phi_0^{1/2}\left\{1 + O\left[(\Phi_0 s)^{-2}\right]\right\} . \tag{2.115}$$

Accordingly, the potential barriers of cases (a) and (b) lead to exactly the same apparent barrier height up to first order in $(\Phi_0 s)^{-1}$. However, the apparent barrier height deduced in cases (a) and (c) is not very close to the work function; instead, the lowered and non-lowered square barriers give apparent barrier heights above the average work function.

As a result of the variation with separation of the actual barrier height in case (b), the tunneling current increases more rapidly as the separation gets smaller, and this effect completely mask, up to first order in $(\Phi_0 s)^{-1}$, the absolute reduction in barrier height, as already shown by Binnig et al[21]. Nevertheless, it cannot be concluded from this that the image potential does not contribute to measurements of the apparent barrier height, as will be shown below.

In case (c), that is, when the full behaviour of the classical image potential is taken into account, the mean barrier height can be written as

$$\bar{\Phi} = \Phi_0 - \frac{f(s)}{\Delta s} \quad , \tag{2.116}$$

where

$$f(s) = -\frac{C s}{4} \int_{s_1}^{s_2} \frac{dz}{z\,(s - z)} \quad . \tag{2.117}$$

Thus substituting (2.116) into (2.103), we find

$$\Phi_{ap} = \left\{ \bar{\Phi}^{1/2} \left(\Delta s' + \frac{1}{2} \frac{f(s)}{\bar{\Phi} \Delta s} \Delta s' - \frac{1}{2} \frac{f'(s)}{\bar{\Phi}} \right) \left[1 + \frac{1}{\alpha \bar{\Phi}^{1/2} \Delta s \,(1 + \alpha \bar{\Phi}^{1/2} \Delta s)} \right] \right.$$

$$\left. + \frac{1}{\alpha \Delta s} \left(\Delta s' - \frac{1}{2} \frac{f(s)}{\bar{\Phi} \Delta s} \Delta s' + \frac{1}{2} \frac{f'(s)}{\bar{\Phi}} \right) \right\}^2 \quad . \tag{2.118}$$

It is of crucial interest to observe that when this expression is expanded in powers of $(\Phi_0 s)^{-1}$ it does not lead to eq. (2.110), unless the function $f'(s)$ has not any non-zero first order term in $(\Phi_0 s)^{-1}$, since in this case

$$\bar{\Phi}^{1/2} \left(1 + \frac{1}{2} \frac{C}{\bar{\Phi} s} \right) = \Phi_0^{1/2} \left\{ 1 - \frac{1}{2} \Phi_0^{-1/2} f'(s) + O\left[(\Phi_0 s)^{-2} \right] \right\} .$$

Indeed, performing the integral in the second hand of eq. (2.117), we find, after some algebra,

$$f(s) = \frac{C}{2} \ln \frac{s + \Delta s}{s - \Delta s} \tag{2.119}$$

and

$$\Delta s = s\left(1 - \frac{C}{\Phi_0 s}\right)^{1/2} . \tag{2.120}$$

Thus substituting eq. (2.120) into eq. (2.119) and derivating, we find

$$f'(s) = \frac{C/2}{\Delta s} \tag{2.121}$$

and

$$\Delta s' = \frac{s - C\,\Phi_0^{-1}/2}{\Delta s} . \tag{2.122}$$

Finally, substituting (2.116), (2.121) and (2.122) into (2.103) we find the apparent barrier height as

$$\Phi_{ap} = \left\{ \bar{\Phi}^{1/2}\left(\frac{\bar{\Phi}+\Phi_0}{2\bar{\Phi}}\frac{s - C\,\Phi_0^{-1}/2}{\Delta s} - \frac{C/4}{\bar{\Phi}\Delta s}\right)\left[1 + \frac{1}{\alpha\bar{\Phi}^{1/2}\Delta s\,(1+\alpha\bar{\Phi}^{1/2}\Delta s)}\right] \right.$$

$$\left. - \frac{1}{\alpha\Delta s}\left(\frac{\Phi_0 - 3\bar{\Phi}}{2\bar{\Phi}}\frac{s - C\,\Phi_0^{-1}/2}{\Delta s} - \frac{C/4}{\bar{\Phi}\Delta s}\right)\right\}^2 , \tag{2.123}$$

where $\bar{\Phi}$ is given by eq. (2.116), as a function of interelectrode separation. In particular, when $s > 1/\Phi_0$ eq. (2.123) can be expanded as[31]

$$\Phi_{ap} = \Phi_0\left\{1 - \left(C/2 - 2\,\alpha^{-1}\,\Phi_0^{1/2}\right)(\Phi_0 s)^{-1} + O\left[(\Phi_0 s)^{-2}\right]\right\} . \tag{2.124}$$

Consequently, the potential barriers of cases (b) and (c) do not lead to the same apparent barrier height, not even up to first order in $(\Phi_0 s)^{-1}$; instead, when the full behaviour of the classical image potential is considered the resulting apparent barrier height is lower than the apparent barrier height obtained in cases (a) an (b), though it is still higher than the actual barrier height. This happens because in case (c) the mean barrier height decreases with separation more slowly than the maximum barrier height, which is obvious from eqs. (2.116) and (2.121), and, accordingly, the absolute reduction in barrier height is not completely masked by the effect of its variation with separation.

It is interesting to observe, also, that for typical work functions the first-order

contributions to the apparent barrier height from the s-dependent part of the pre-exponential factor in the current density and from the s - dependent f function in eq. (2.116) nearly cancell out: when $\Phi_0 = 4.8$eV the potential barrier of case (c) leads to an apparent barrier height that would exactly coincide, up to first order in $(\Phi_0\, s)^{-1}$, with the average work for $C = 0.59$. Consequently, when the exact classical image potential of eq. (2.64) or the approximated formulas of eqs. (2.65) and (2.66) are considered the apparent barrier height approaches the average work function from below for large interelectrode separation and remains, for gap widths large enough for second and higher order terms in $(\Phi_0\, s)^{-1}$ to be negligible, nearly equal to the average work function, as the results of next section will also show.

In order to illustrate the discussion we have just made about the contribution of the image potential to the apparent barrier height, in fig. 2.36 we show the apparent barrier heights deduced from eqs. (2.108), (2.114) and (2.123) for cases (a), (b) and (c), respectively, for two different values of C.

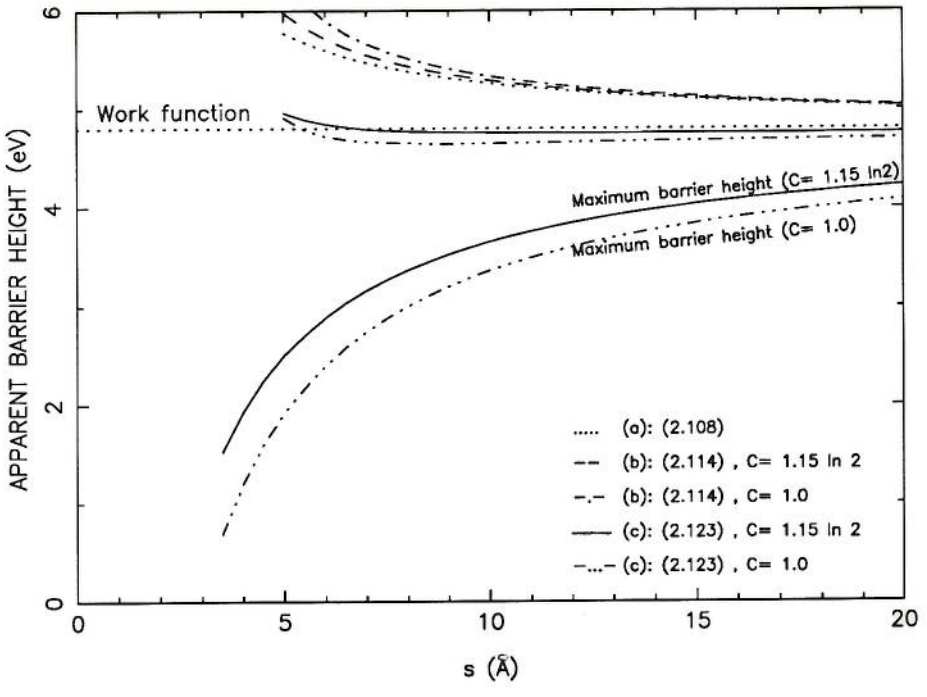


Fig. 2.36. Apparent barrier heights deduced from eqs. (2.108), (2.114) and (2.123) for cases (a), (b) and (c) of fig. 2.35, respectively, as a function of tip-sample distance, for two different values of C: 1.15 ln2 (solid and dashed curves) and 1.0 (dashed-dotted and dashed-dotted-dotted-dotted curves). The maximum barrier heights of cases (b) and (c) are also shwon for these two values of C.

In agreement with the preceding discussion, it is obvious from this figure that when the image potential reduced barrier is assumed to be constant and equal to its maximum value (case (b)) the apparent barrier height is larger than Φ_0; however, when the more appropriate image reduced barrier of case (c) is considered the apparent barrier height is somewhat smaller than Φ_0, showing the important role that the full behaviour of the image potential plays in lowering the apparent barrier height, even though it is higher than the actual barrier height. It is interesting to observe, also, that the apparent barrier height is in case (c) rather constant and close to Φ_0, although it depends for all gap widths slightly on the maximum barrier height: greater maximum barrier heights give greater apparent barrier heights. Contrarily, in case (b) the apparent barrier height is, for gap widths large enough for second and higher order terms in $(\Phi_0\, s)^{-1}$ to be negligible, independent of the maximum barrier height, and it gets larger, at very small gap widths, as the maximum barrier height decreases.

Exact results

For small interelectrode separations the WKB mean barrier approximations are no longer valid, so that it is necessary to calculate exactly the transmission probabilities of tunneling electrons and integrate numerically over all allowed energies by means of eq. (2.9).

The transmission probabilities of electrons tunneling the non-lowered and lowered square barriers of cases (a) and (b) of the preceding section are easily calculated by connecting exponential functions, solutions of the time-independent Schrödinger equation through this barriers, and their derivatives at the interfaces:

$$D = \frac{4\, k_L\, k_R\, k^2}{k^2\,(k_L + k_R)^2 + \left[k^2\,(k^2 + k_L^2 + k_R^2) + k_L^2\, k_R^2\right] \sinh^2(k\, s)}\ , \tag{2.125}$$

where

$$k_L = \sqrt{2\,(E - U_L)}\ , \tag{2.126}$$

$$k_R = \sqrt{2\,(E - U_R)} \tag{2.127}$$

and

$$k = \sqrt{2\,(-E - C/s)} \quad . \tag{2.128}$$

The constant C is zero when the unreduced square barrier of case (a) is considered.

Now substituting eq. (2.125) into eq. (2.9) and then introducing eq. (2.9) into eq. (2.100) we can compute the apparent barrier height. In particular, if transmission probabilities of electrons with energy components E_z smaller than the Fermi energy are neglected one finds

$$\Phi_{ap} = \frac{1}{8}\left(\frac{\partial \ln D_0}{\partial s} + \frac{C}{k_0 s^2}\frac{\partial \ln D_0}{\partial k_0}\right)^2 \quad , \tag{2.129}$$

where

$$\frac{\partial \ln D_0}{\partial s} = \frac{-k_0\left[k_0^2\,(k_0^2 + k_L^2 + k_R^2) + k_L^2 k_R^2\right]\sinh(2\,k_0\,s)}{B} \tag{2.130}$$

and

$$\frac{\partial \ln D_0}{\partial k_0} = \frac{2}{k_0} - \frac{A}{B} \quad . \tag{2.131}$$

In these expressions D_0 represents the transmission probability of Fermi electrons incident in the direction perpendicular to the tunnel junction, and

$$k_0 = \sqrt{2\,(\Phi_L - C/s)} \quad , \tag{2.132}$$

$$A = 2\,k_0\,(k_L + k_R)^2 + 2\,k_0\,(2\,k_0^2 + k_L^2 + k_R^2)\sinh^2(k_0 s) + \left[k_0^2\,(k_0^2 + k_L^2 + k_R^2) + k_L^2 k_R^2\right] s \sinh(2\,k_0 s) \tag{2.133}$$

and

$$B = k_0^2\,(k_L + k_R)^2 + \left[k_0^2\,(k_0^2 + k_L^2 + k_R^2) + k_L^2 k_R^2\right]\sinh^2(k_0 s) \quad . \tag{2.134}$$

Fig. 2.37 exhibits the apparent barrier height calculated when the transmission probabilities of eq. (2.125) are integrated by means of eq. (2.9) and the result introduced in eq. (2.100), together with the apparent barrier height of eq. (2.129). This figure shows that the contribution to the apparent barrier height from electrons with energy component E_z smaller than the Fermi energy is important, as also shown by eqs. (2.110) and (2.124) of the preceding section. On the other hand, a reduction in the barrier height prportional to $1/s$ does

not introduce any change in the apparent barrier height for large separations; moreover, for small separations lower barriers give higher apparent barrier heights, in agreement with the results of the preceding section.

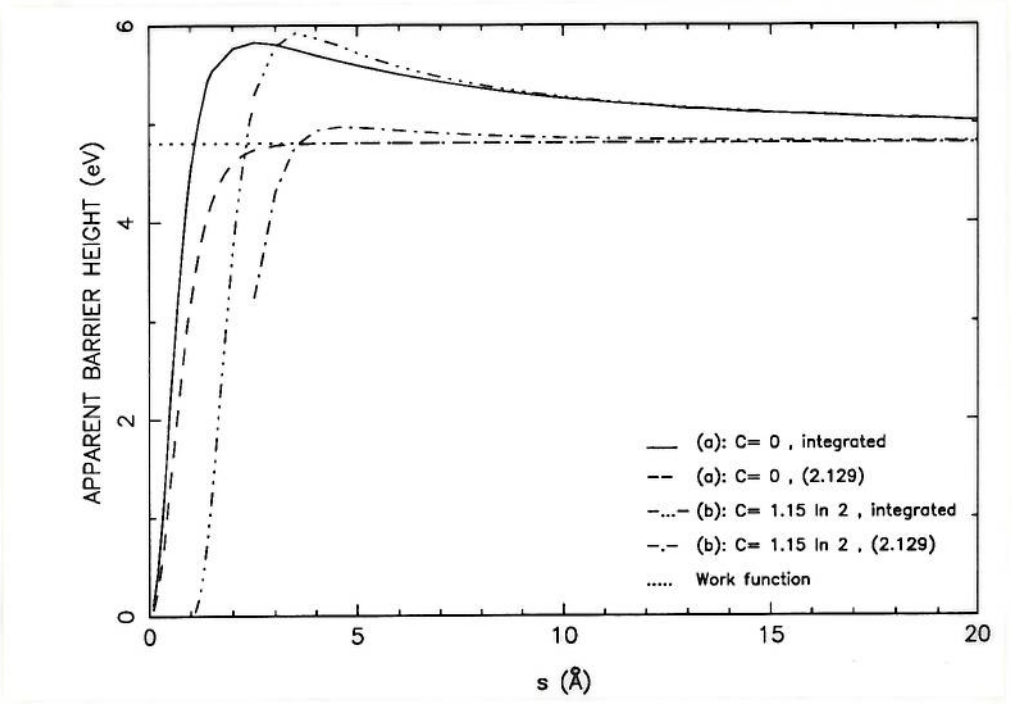


Fig. 2.37. Exact results for the apparent barrier height, as a function of tip-sample distance, when the non-lowered (solid curve) and lowered (dashed-dotted-dotted-dotted curve) square barriers of cases (a) and (c) are considered and the tunneling current density is calculated integrating the transmission probability of eq. (2.125) over all allowed energies by means of eq. (2.9). The apparent barrier height of eq. (2.129) obtained not integrating the transmission probability over allowed energies is also represented for the non-lowered (dashed curve) and lowered (dashed-dotted curve) square barriers.

It is worth mentioning that when a very small applied voltage is introduced in the square barriers of cases (a) and (c) and Airy functions and their derivatives are connected at the interfaces in order to determine the transmission probabilities, exactly the same results as those shown in fig. 2.37 are obtained, as we expected.

The transmission probabilities of electrons tunneling the approximated image reduced potential barrier of Simmons have been calculated solving the Schrödinger equation numerically, thus obtaining the exact tunneling current density by integrating over all allowed energies. The apparent barrier height deduced fro eq. (2.100) having calculated the current density in this way is represented in fig. 2.38, for small separations, together with the apparent

barrier heights of cases (a) and (b) also represented in fig. 2.37. Let us emphasize that the apparent barrier height is for the more appropriate potential barrier of case (c) rather constant and close to Φ_0 for gap widths larger than 5 or 6Å, in agreement with the experimental results and the discussion of last section. However, in these calculations the apparent barrier height goes to zero for s ≈ 1Å; this is a shortcoming of the image potential model introduced, which at very small separations does not describe the barrier that electrons feel when they tunnel between the tip and the sample. Indeed, as shown by Lang[86] and Ferrer et al[87], the apparent barrier height goes to zero for $s = 0$.

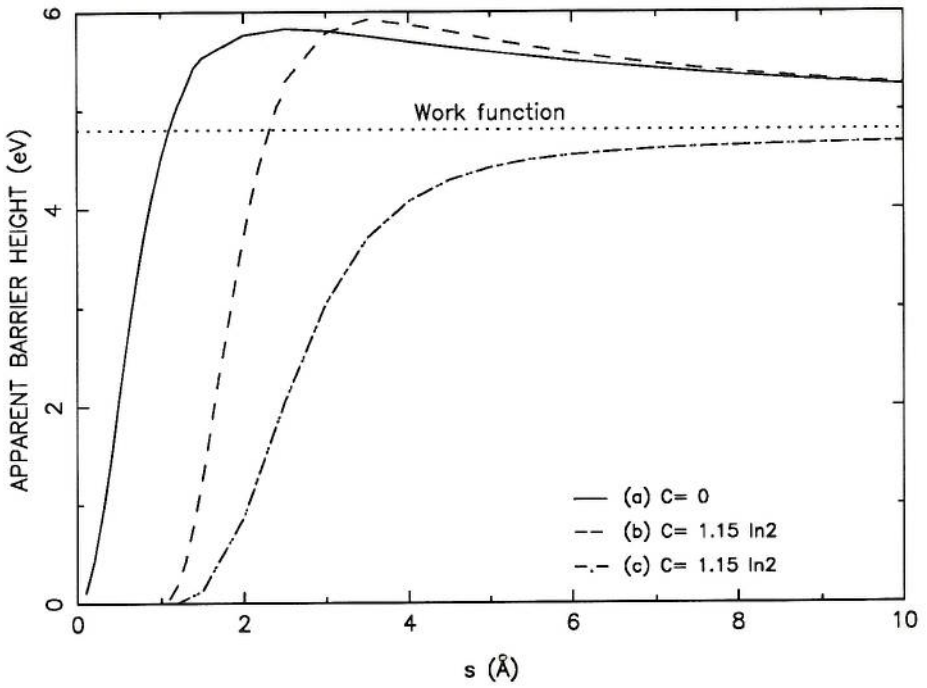


Fig. 2.38. Exact results for the apparent barrier height, as a function of tip-sample distance, when the potential barriers of cases (a) (solid curve), (b) (dashed curve) and (c) (dashed-dotted curve) are considered: (a) unlowered sqare barrier, (b) lowered square barrier with C = 1.15 ln2 and (c) Simmons approximation to the image reduced barrier (C =1.15 ln2).

In order to give a more realistic description of the barrier, we have improved on these results by using the parametrized model barrier of eq. (2.73). For small interelectrode separations eqs. (2.80) and (2.81) are no longer valid and the parameters λ_L and λ_R making the value of the interface potential at the image planes constant strongly depend on the gap distance. To evaluate these gap distant dependent parameters, we have solved mumerically for

each distance the following algebraic system

$$V(z_L) = -\frac{1}{4}\left[\lambda_L - \frac{e^{-\lambda_R d} - 1}{d} - \frac{\mu}{d}\right], \tag{2.135}$$

$$V(s - z_R) = -\frac{1}{4}\left[\lambda_R - \frac{e^{-\lambda_L d} - 1}{d} - \frac{\mu}{d}\right] - \Delta\Phi \ . \tag{2.136}$$

The gap distance dependent parameters λ_L eta λ_R making $V(z_L) = V(s\text{-}z_R) = -\Phi_L - 1.3\text{eV}$ are shown in table 2.1 for $\Phi_L = \Phi_R = 4.8\text{eV}$, and in table 2.2 for $\Phi_L = 3\text{eV}$ and $\Phi_R = 6\text{eV}$. In these tables the gap distance dependent parameter μ considered in our calculations is also shown.

Table 2.1. Potential barrier parameters λ_L, λ_R and μ considered in our calculations when the work functions are taken to be $\Phi_L = \Phi_R = 4.8\text{eV}$.

d (Å)	μ	$\lambda_L = \lambda_R$ (a_0^{-1})	d (Å)	μ	$\lambda_L = \lambda_R$ (a_0^{-1})
0.1	0.01	0.49	1.0	0.50	0.76
0.3	0.09	0.57	3.0	0.50	0.81
0.5	0.22	0.65	5.0	0.50	0.85
0.7	0.35	0.71	7.0	0.50	0.86
0.9	0.46	0.75	9.0	0.50	0.87

Table 2.2. Potential barrier parameters λ_L, λ_R and μ considered in our calculations when the work functions are taken to be $\Phi_L = 3eV$ and $\Phi_R = 6eV$.

d(Å)	μ	$\lambda_L(a_0^{-1})$	$\lambda_R(a_0^{-1})$	d(Å)	μ	$\lambda_L(a_0^{-1})$	$\lambda_R(a_0^{-1})$
0.1	0.01	-1.59	2.99	1.0	0.50	0.44	1.04
0.3	0.09	-0.19	1.43	3.0	0.50	0.55	1.00
0.5	0.22	0.16	1.16	5.0	0.50	0.58	1.02
0.7	0.35	0.33	1.08	7.0	0.50	0.60	1.04
0.9	0.46	0.42	1.05	9.0	0.50	0.61	1.05

The tunneling current density calculated by means of eq. (2.9) of electrons tunneling the parametrized potential barrier (2.73) is plotted in fig. 2.39 versus gap distance, i.e. distance between image planes, for $V_a = 0.01V$, $\Phi_L = \Phi_R = 4.8eV$ and the gap distance dependent barrier parameters λ_L, λ_R and μ given in table 2.1, which approximately fit the potential of ref. 74. In figs. 2.40 and 2.41 the apparent barrier height is exhibited as a function of gap distance, for the special case $\Phi_L = \Phi_R = 4.8eV$ and also for significantly different values of the work functions ($\Phi_L = 3eV$ and $\Phi_R = 6eV$), when the potential barrier parameters λ_L, λ_R and μ are taken to be those of tables 2.1 and 2.2, respectively. The results of these figures also show that the apparent barrier height is rather constant and quite close to Φ_0 for $d \gtrsim 6$Å, although they differ, at short gap distances, substantially from the results obtained with the classical image potential of eq. (2. 107). Indeed, the apparent barrier height calculated with the model barrier of eq. (2.73) goes to zero for $d = 0$, in agreement with refs. 86 and 87.

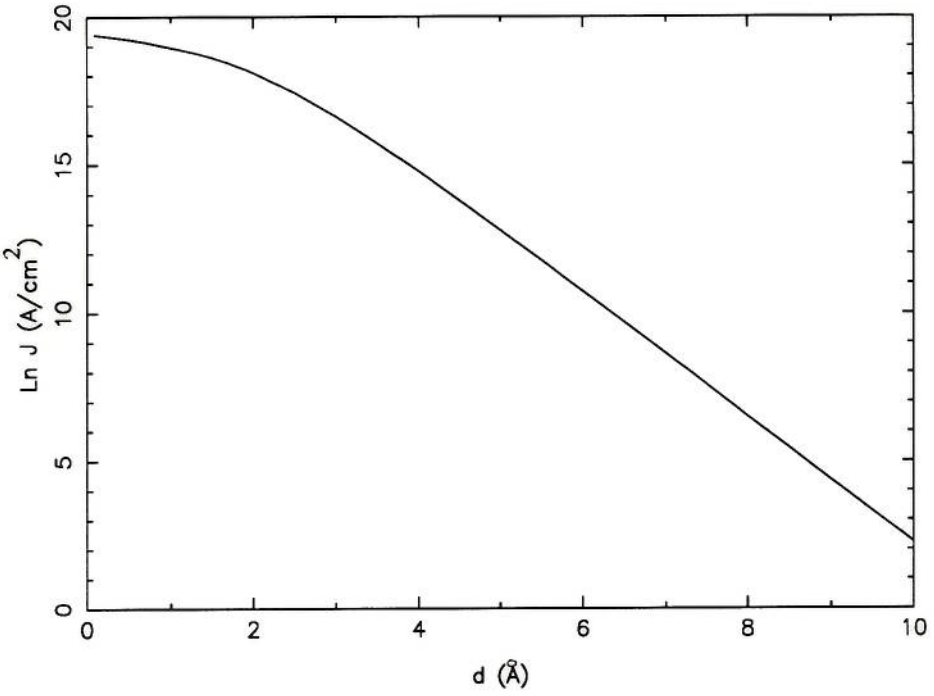


Fig. 2.39. Natural logarithm of the tunneling current density versus gap distance, for V_a = 0.01V, deduced from eq. (2.9) having solved the Schrödinger equation through the potential barrier of eq. (2.73) with $\Phi_L = \Phi_R$ = 4.8eV and the gap distance dependent barrier parameters of table 2.1.

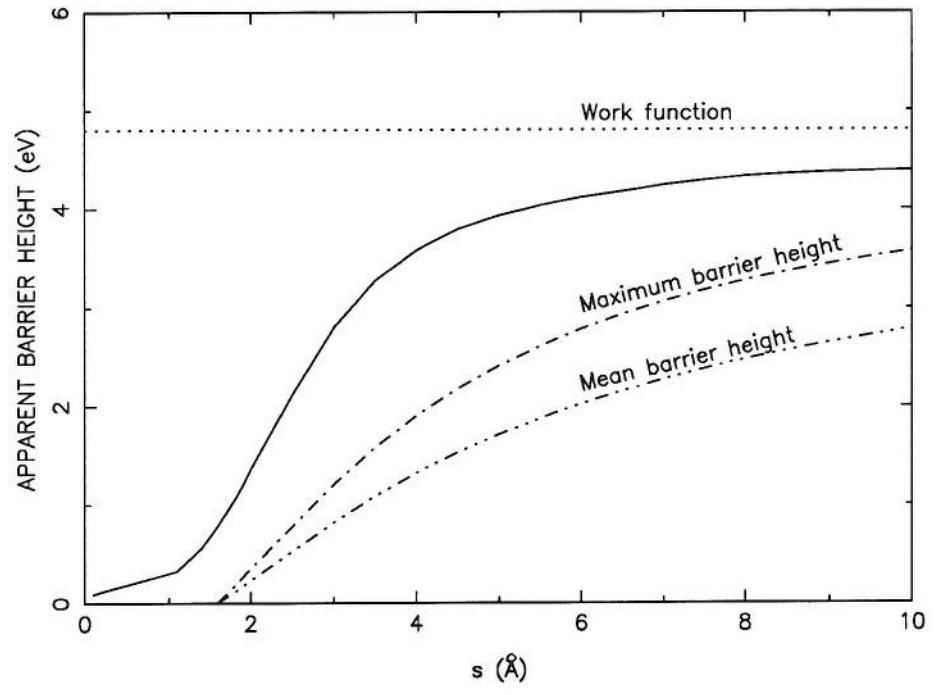


Fig. 2.40. As in fig. 2.38, but when the model barrier of eq. (2.73) is considered, with $\Phi_L = \Phi_R$ = 4.8eV and the gap distance dependent barrier parameters of table 2.1. Also shown are the maximum barrier height and the mean barrier height defined by eq. (2.18).

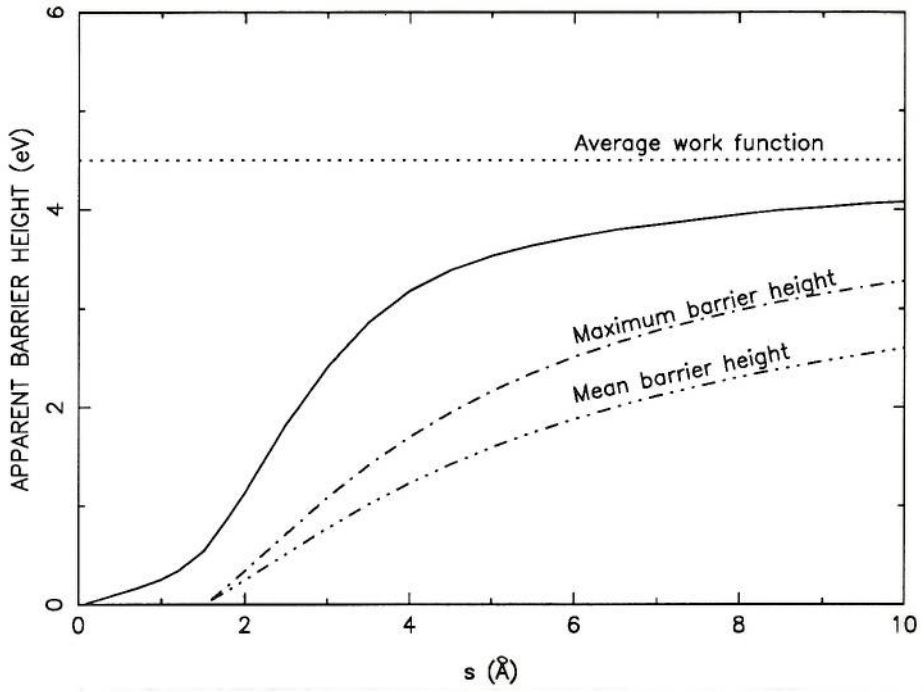


Fig 2.41. As in fig. 2.40, but with Φ_L = 3.0eV, Φ_R = 6.0eV and the gap distance dependent barrier parameters of table 2.2.

In figs. 2.40 and 2.41 we show, as well, the mean barrier height, $\overline{\Phi}$, as calculated from eq. (2.18) using the potential model of eq. (2.73). The comparison of the two barriers, $\overline{\Phi}$ and Φ_{ap}, shows the large difference between them for the actual potential of the interface. On the other hand, it is worth emphasizing that the apparent barrier height is always smaller than Φ_0: this is the main difference between the results presented here and Lang´s calculation[81], which otherwise shows a reasonable agreement with our results at short distances. The reason of this discrepancy can be traced back to the non-local effects (image potential), not included in Lang´s calculation, which play an important role in lowering the apparent barrier height, as has been shown above.

References

1. E. Schrödinger, *Quantization as a problem of proper values*, Part I. Annalen der Physik. **79** 361 (1926). Part II, **79** 489 (1926). Part III, **80** 437 (1926). Part IV, **81** 109 (1926).
2. J.R. Oppenheimer, *Three notes on the quantum theory of aperiodic effects*, Phys. Rev. **31** 66 (1928).
3. G. Gamow, *Zur quanten theorie des atomkernes*, Z. Phys. **51** 204 (1928).
4. R.H. Fowler & L. Nordheim, *Electron emission in intense electric fields*, Proc. Roy. Soc. (London) **119** 173 (1928).
5. E.W. Müller, *Electron-microscopic observations upon field cathodes*, Z. Physik. **106** 541 (1937).
6. E.W. Müller, *The resolution of the field-ion microscope*, Z. Naturforsch. **11**a 88 (1956). See also R.H. Good & E.W. Müller, *Field emission*, in Handbuch der Physik Vol. 21 (Edited by S. Flugge, Spring Verlag, Berlin, 1956), p. 176.
7. R.D. Young, J. Ward & F. Scire, *Observation of metal-vacuum-metal tunneling, field emission, and the transition region*, Phys. Rev. Lett. **27** 922 (1971).
8. R.D. Young, J. Ward & F. Scire, *The topografiner: An instrument for measuring surface microtopografy*, Rev. Sci. Instrum. **43** 999 (1972).
9. W.A. Thompson & S.F. Hanrahan, *Thermal drive apparatus for direct vacuum tunneling experiments*, Rev. Sci. Instrum. **47** 1303 (1976).
10. E.C. Teague, *Room temperature gold-vacuum-gold tunneling experiments*, Ph.D. thesis, North Texas State University, Denton, Texas (1978).
11. G.Binnig, H. Rohrer, Ch. Gerber & E. Weibel, *Tunneling through a controlable vacuum gap*, Appl. Phys. Lett. **40** 178 (1982).
12. G.Binnig, H. Rohrer, Ch. Gerber & E. Weibel, *Surfaces studies by scanning tunneling microscopy*, Phys. Rev. Lett. **49** 57 (1982).
13. G.Binnig & H. Rohrer, *Scanning tunneling microscopy*, Helv. Phys. Acta **55** 726 (1982).

14. G.Binnig & H. Rohrer, *Scanning tunneling microscopy - from birth to adolescence*, Rev. Mod. Phys. **59** 615 (1987).

15. C. Kittel, *Elementary statistical physics* (New York: John Wiley, 1958), p. 25.

16. For reviews of scanning tunneling microscopy and references, see G. Binnig & H. Rohrer, *Scanning tunneling microscopy*, Physica **127**B 37 (1984). A. Baratoff, *Theory of scanning tunneling microscopy - Methods and approximations*, Physica **127**B 143 (1984). G. Binnig & H. Rohrer, *Scanning tunneling microscope*, Sci. Am. **253** 50 (1985); J.A. Golovchenko, *The tunneling microscope: A new look at the atomic world*, Science **232** 48 (1986); C.F. Quate, *Vacuum tunneling: A new technique for microscopy*, Phys. Today, **39** 26 (1986); P.H. Cutler, T.E. Feuchtwang & Y. Kuk., *Theory and application of scanning tunneling microscopy*, Materials forum **10** no.2 (1987); T.E. Feuchtwang & P.H. Cutler, *Tunneling and scanning tunnel microscopy: A critical review*, Physica Scripta **35** 132 (1987); E. Louis, F. Flores & P.M. Echenique, *Theoretical aspects of scanning tunneling microscopy*, Physica Scripta **37** (1988); J. Gimzewski, *New fields for STM*, Physics World **225** (1989); E. Louis, F. Flores & P.M. Echenique, *Theory of scanning tunneling microscopy*, Radiat. Eff. **109** 309 (1989).

17. G. Binnig, H. Rohrer, Ch. Gerber & E. Weibel, *7×7 reconstruction on Si(111) resolved in real space*, Phys. Rev. Lett. **50** 120 (1983).

18. R.S. Becker, J.A. Golovchenko, E.G. McRae & B.S. Swartzentruber, *Tunneling i mages of atomic steps on the Si(111) 7×7 surface*, Phys. Rev. Lett. **55** 2028 (1985).

19. G. Binnig & H. Rohrer, *Scanning tunneling microscopy*, Surf. Sci. **126** 236 (1986).

20. R.M. Tromp, *Spectroscopy with the scanning tunneling microscope: a critical review*, J. Phys. C **1** 10211 (1989).

21. G. Binnig, N. García, H. Rohrer, J.M. Soler & F.Flores, *Electron-metal surface interaction potential with vacuum tunneling: Obervation of the image force*, Phys. Rev. B **30** 4816 (1984).

22. J.K. Gimzewsky & R. Moller, *Transition from the tunneling regime to point contact studied using scanning tunneling microscopy*, Phys. Rev. B **36** 1284 (1987).

23. G. Binnig, K.H. Frank, H. Fuchs, N. García, B. Reihl, H. Rohrer, F. Salvan & A.R. Williams, *Tunneling spectroscopy and inverse photoemission: Image and field states*, Phys. Rev. Lett. **55** 991 (1985).

24. R.S. Becker, J.A. Golovchenko & B.S. Swartzentruber, *Electron Interferometry at Crystal surfaces*, Phys. Rev. Lett. **55** 987 (1985).

25. R.S. Becker, J.A. Golovchenko, D.R. Hamann & B.S. Swartzentruber, *Real-space observation of surface states on Si(111) 7×7 with the tunneling microscope*, Phys. Rev. Lett. **55** 2032 (1985).

26. R.M. Feenstra, J.A. Stroscio and A.P. Fein, *Tunneling spectroscopy of the Si(111) 2×1 surface*, Surface Sci. **181** 295 (1987).

27. J.H. Coombs & J.K. Gimzewski, *Fine structure in field emission resonances at surfaces*, J. Microscopy **152** 841 (1988).

28. J. Bono and R.H. Good, *Conductance oscillations in scanning tunneling microscopy as a probe of the surface potential*, Surface Sci. **188** 153 (1987).

29. J.M. Pitarke & P.M. Echenique, *Potential barrier for tunneling electrons in STM,* Proceeding of the 11th Werner Brandt Workshop on Penetration Phenomena of Charged Particles in Matter, Oak Ridge, Tennessee, April 14-15 (1988).

30. J.M.Pitarke, F. Flores & P.M. Echenique, *Tunneling spectroscopy: Surface geometry and interface potential effects*, Surf. Sci. **234** 1 (1990).

31. J.M. Pitarke, P.M. Echenique & F.Flores, *Apparent barrier height for tunneling electrons in STM*, Surf. Sci. **217** 267 (1989).

32. J. Bardeen, *Tunneling from a many-particle point of view*, Phys. Rev. Lett. **6** 57 (1961).

33. J. Tersoff & D.R. Hamann, *Theory and application of the scanning tunneling microscope*, Phys. Rev. Lett. **50** 1998 (1983).

34. T.E. Feuchtwang, P.H. Cutler & N.M. Miskovsky, *A theory of vacuum tunneling microscopy*, Phys. Lett. A **99** 167 (1983).

35. J. Tersoff & D.R. Hamann, *Theory of the scanning tunneling microscope*, Phys. Rev. B **31** 805 (1985).

36. M.S. Chung, T.E. Feuchtwang, P.H. Cutler, *Spherical tip model in the theory of the*

scanning tunneling microscope, Srf. Sci. **187** 559 (1987).

37. J. Tersoff, *Method for the calculation of scanning tunneling microscope images and spectra*, Phys. Rev. B **40** 11990 (1989).
38. N.D. Lang, *Vacuum tunneling current from an adsorbed atom*, Phys. Rev. Lett. **55** 230 (1985).
39. N.D. Lang, *Theory of single-atom imaging in the scanning tunneling microscope*, Phys. Rev. Lett. **56** 1164 (1986).
40. N.D. Lang, *Apparent size of an atom in the scanning tunneling microscope as a function of bias*, Phys. Rev. Lett. **58** 45 (1987).
41. A. Sommerfeld & H. Bethe, *Electronentheorie der Metalle*, in Hanbuch der Physik Vol. 24 (Edited by S. Flugge, Springer Verlag, Berlin, 1953), p. 240.
42. N. García, C. Ocal & F. Flores, *Model theory for scanning tunneling microscopy: application to Au(110) (1×2)*, Phys. Rev. Lett. **50** 2002 (1983).
43. E. Stoll, A. Baratoff, A. Selloni & P. Carnevali, *Current distribution in the scanning vacuum tunnel microscope: a free-electron model*, J. Phys. C **17** 3073 (1984).
44. L.D. Landau & E.M. Lifshitz, *Course of theoretical physics, Vol.3: Quantum Mechanics (non relativistic theory)* (3rd. ed. Oxford, England: Pergamon Press, 1977), pp. 76-78.
45. J.G. Simmons, *Generalized formula for the electric tunnel effect between similar electrodes separated by a thin insulating film.* J. Appl. Phys. **34** 1793 (1963).
46. C.B. Duke, *Tunneling in solids* (New York: Academic Press, 1969), p. 60.
47. E. Merzbacher, *Quantum mechanics* (2nd edition, New York: Jon Wiley and Sons, 1952), chapter 7.
48. R. Holm, *The electric tunnel effect across thin insulator films in contacts*, J. Appl. Phys. **22** 569 (1951).
49. N.M. Miskovsky, P.H. Cutler, T.E. Feuchtwang & A.A. Lucas, *The multiple-image interactions and the mean-barrier approximation in MOM and MVM tunneling junctions*, Appl. Phys.A **27** 139 (1982).
50. M. Abramowitz & I.A. Stegun, *Handbook of Mathematical Functions* (Dover, New York, 1965), p. 446.

51. B.A. Politzer, *Comparison of a numerical method and the WKB approximation in the determination of transmission coefficients for thin insulating films*, J.Appl. Phys. **37** 279 (1965).

52. K.H. Gundlach, *Zur Berchnung des tunnelstroms durch eine trapezformige potentialstufe*, Solid-State Electron. **9** 949 (1966).

53. W.R. Smythe, *Static and Dynamic Electricity* (New York, Mac Graw-Hill, 1953), chapter 4.

54. See ref. 28. The form of the image potential given here is in error by a factor of 2, and the correct formula is given by eq. (2.61), as Simmons pointed out in a subsequent paper (J.G. Simmons, *Potential barriers and emission-limited current flow between closely spaced parallel metal electrodes*, J. Appl. Phys. **35** 2472 (1964)).

55. See ref. 50, chapter 6.

56. C.M.M. Nex, *The use of Chebyshev series in computational physics* , Computer Physics Communications **20** 1 (1980).

57. P.M. Echenique & J.B. Pendry, *The existence and detection of Rydberg states at surfaces*, J. Phys. C **11** 2065 (1978).

58. R. García, J.J. Sáenz, J.M. Soler & N. García, *Tunneling current through localized surface states*, Surf. Sci. **181** 69 (1987).

59. R. García, J.J. Sáenz, J.M. Soler & N. García, *Distance-voltage characteristics in scanning tunneling microscopy*, J. Phys. C **19** L31 (1986).

60. C.T. Lynch, *CRC Handbook of Material Science*, CRC Press, Inc. Boca Raton, Florida.

61. N.D. Lang & W. Kohn, *Theory of metal surfaces: charge density and surface energy*, Phys. Rev. B **1** 4555 (1970).

62. N.D. Lang & W. Kohn, *Theory of metal surfaces: work function*, Phys. Rev B **3** 1215 (1971).

63. N.D. Lang & W. Kohn, *Theory of metal surfaces: induced surface charge and image potential*, Phys. Rev. B **7** 3541 (1973).

64. P. Hohenberg & W. Kohn, *Inhomogeneous electron gas*, Phys. Rev. 136 B864 (1964). See also N.D. Lang, *Density-functional formalism and the electronic structure of*

metal surfaces, in Solid State Physics Vol. 28 (1973), p. 225.

65. W. Kohn & L.J. Sham, *Self-consistent equations including exchange and correlation effects*, Phys. Rev. **140** A1133 (1965).
66. V. Dose, W. Altman, A. Goldman, V. Kolac & J. Rogozik, *Image-potential states observed by inverse photoemission*, Phys. Rev. Lett. **52** 1922 (1984).
67. D. Straub & F.J. Himpsel, *Identification of image-potential surface states on metals*, Phys. Rev. Lett. **52** 1922 (1984).
68. B. Reihl, K.H. Frank & R.R. Schliter, *Image-potential and intrinsic surface states on Ag(100)*, Phys. Rev. B **30** 7328 (1984).
69. N. García, B. Reihl, K.H. Frank & A.R. Williams, *Image states: Binding energies, effective masses and surface corrugations*, Phys. Rev. Lett. **54** 591 (1985).
70. P.M. Echenique, R.H. Ritchie, N. Barberan & J.Inkson, *Semiclassical image potential at a solid surface*, Phys. Rev. B **23** 6486 (1981).
71. J.R. Manson & R.H. Ritchie, *Self-energy of a charge near a surface*, Phys. Rev. B **24** 4867 (1981).
72. P.M. Echenique, A. Gras-Marti, J.R. Manson & R.H. Ritchie, *Image potential for a tunneling electron*, Phys. Rev. B **35** 7357 (1987).
73. F. García Moliner and F. Flores, *Introduction to the theory of solids surfaces*, (Cambridge Univ. Press, 1979).
74. P. De Andrés, F. Flores, P.M. Echenique & R.H. Ritchie, *A barrier potential calculation for tunneling electrons at a metal-metal interface*, Europhys. Lett. **3** 101 (1987).
75. S. Ossicini & C.M. Bertoni, *Image-force effects on the barrier height for metal-metal tunneling electrons*, Phys. Rev. B **35** 848 (1987).
76. M.T. Michalewicz & J.Mahanty, *Correction to image potential between metals* , Phys. Lett. A **116** 392 (1986).
77. B.N.J. Persson & A. Baratoff, *Self-consistent dynamic image potential in tunneling*, Phys. Rev B **38** 9616 (1988).
78. R.O. Jones, P.J. Jennings and O. Jepsen, *Surface barrier in metals: A new model with application to W(001)*, Phys. Rev. B **29** 6474 (1987).

79. S. Ossicini, C.M. Bertoni & P. Gies, *Image plane for surface potential*, Europhys. Lett. **1** 661 (1989).

80. P.A. Serena, *Self-consistent image potential in a metal surface*, Phys. Rev. B **34** 6767 (1986).

81. N.D. Lang, *Apparent barrier height in scanning tunneling microscopy*, Phys. Rev. B **37** 10395 (1988).

82. See ref. 53

83. R.S. Becker & J.A. Golovchenko, private communication.

84. J.H. Coombs, M.E. Welland & J.P. Pethica, *Experimental barrier heights and the image potential in scanning tunneling microscopy*, Surf. Sci. **198** L353 (1988).

85. M.C. Payne & J.C. Inkson, *Measurement of workfunctions by tunneling and the effect of the image potential*, Surf. Sci. **159** 485 (1985).

86. N.D. Lang, *Resistance of a one-atom contact in the scanning tunneling microscope*, Phys. Rev. B **36** 8173 (1987).

87. J. Ferrer, A. Martin-Rodero & F. Flores, *Contact resistance in the scanning tunneling microscope at very small distances,* Phys. Rev. B **38** 10113 (1988).

3. INTERACTION OF SWIFT DICLUSTERS WITH ELECTRONS IN SOLIDS: KNOCK-ON ELECTRON EMISSION

3.1.Introduction

It is well known that the potential of charged particles is modified when they pass through matter; indeed, when charged particles penetrate a solid target they disturb the electrons of the target and the response of these electrons represents a modification of the electric field and potential of the penetrating particles.

In particular, for swift charges particles with velocity exceeding the Fermi velocity the electron density of the target shows collective oscillations behind the instantaneous location of the projectile. In 1948 Böhr[1] referred for the first time to this phenomenon of coherent electron displacements in solids, and explained qualitatively that a fast positively charged particle penetrating matter induces an electronic polarization wake trailing behind the particle; however, the first calculation of the wake was made by Neufeld and Ritchie[2-4], who derived an explicit expression for the distribution of the polarization density in the space sourrounding the moving particle.

In order to account for the wake potential and the induced electron density fluctuations originated by the passage of fast charged particles through matter, Neufeld and Ritchie treated the electron gas as a quantum plasma and studied the dynamic behaviour of the plasma in the linear approximation, following the collective description of electron interactions which had been investigated by Bohm and Pines[5-8]. Neufeld and Ritchie used a local metallic dielectric function to represent the response of the medium, and found that as a result of the collective response of the medium the induced electron density is periodically distributed in space and time. A quantum mechanical dielectric response function of the electron gas has been derived by Lindhard[9], in the Random Phase Approximation (RPA)[10].

Since these pioneering works were developed, the distribution in space and time of perturbations of electron motion in solids caused by the passage of swift particles has been the subject of a continued theoretical and experimental interest[11-27]. In particular, non-local dielectric functions of the target have been used[15,18,19,22,23] to calculate the wake potential and the induced electron density fluctuations, and also to estimate the binding energy of wake-riding states and the stopping of a charged particle passing through matter due to the

polarization of the medium.

Most of the experimental work in this field is related to measurements of the electric field strength and the wake potential, quantities that are obtained from certain averages of the induced electron density fluctuations. However, recent experimental research has been concerned with the distribution in space of valence electron density fluctuations induced by the passage of swift ions[28]: measurements of the knock-on collision electrons emitted under bombardment of swift dimolecular ions have been performed, since the electron density fluctuations induced by the leading ion around the trailing ion of the bombarding dicluster may appear experimentally in the dependence of the emitted knock-on electron yield on the orientation of the projectile.

In order to interpretate such experiments for the detection of electron density fluctuations, it would be necessary to use a non-linear theory which accounts at the same time for the induced electron density fluctuations and the non-linear effects associated to the multiple scattering between valence electrons and bombarding diclusters; however, no detailed non-linear theory exists at present. In this chapter some preliminary theoretical work involving the interpretation of such experiments is presented.

In section 3.2 linear-response theory calculations of the electron density fluctuations induced by the leading ion at the position of the trailing ion of the bombarding dicluster are presented[29], as a function of the orientation of the projectile, in the plasmon-pole approximation. In section 3.3 we go beyond first order and study theoretically the dependence of the 0° knock-on collision electron yield caused by the passage of swift dimolecular ions through matter on the orientation of the moving diclusters; the scattering by each ion is described by means of the phase shifts of a velocity dependent Yukawa potential describing the dynamic screening, and the multiple scattering effects are approximated within the second Born approximation[30]. In section 3.4 scattering theory is combined with methods developed in the theory of low energy electron difraction (LEED), in order to study in detail the dependence of multiple scattering effects on the orientation of the molecular axis of the projectiles[31]. Finally, references are given.

3.2. Electron density fluctuations

Assume that a charge of magnitude Z moves with uniform velocity $\boldsymbol{v}$ through an homogeneous isotropic electron plasma. Noting that a fast charged particle (v > 1a.u.) which interacts with matter may be considered to be a point charge with a well-defined trajectory, the charge density due to this particle is

$$\rho_{ext}(\boldsymbol{k}, \omega) = Z\,\delta(\boldsymbol{r} - \boldsymbol{v}t) \ . \tag{3.1}$$

Assuming that departures of the plasma from equilibrium are small perturbations around the undisturbed motion of the system, we can use a linear approximation and find

$$\rho(\boldsymbol{k}, \omega) = \frac{\rho_{ext}(\boldsymbol{k}, \omega)}{\varepsilon(\boldsymbol{k}, \omega)} \ , \tag{3.2}$$

where $\rho_{ext}(\boldsymbol{k},\omega)$ is the Fourier transform of the charge density due to the external particle and $\varepsilon(\boldsymbol{k},\omega)$ represents the dielectric response function of the plasma. Hence, the induced electron density fluctuation $\delta n(\boldsymbol{r},t) = -\rho_{ind}(\boldsymbol{r},t)$ in the medium is given by

$$\delta n(\boldsymbol{r}, t) = -\frac{1}{(2\pi)^4}\int d\boldsymbol{k}\, d\omega\, \rho_{ext}(\boldsymbol{k}, \omega)\left[\frac{1}{\varepsilon(\boldsymbol{k}, \omega)} - 1\right] e^{i(\boldsymbol{k}\cdot\boldsymbol{r} - \omega t)} \ . \tag{3.3}$$

Now substituting eq. (3.1) into eq. (3.3), one finds

$$\delta n(\rho, z, t) = -\frac{Z}{(2\pi)^2 v}\int_0^\infty d k_\perp\, k_\perp J_0(k_\perp \rho)\int_{-\infty}^{\infty} d\omega\, e^{i\frac{\omega}{v}(z - vt)}\left[\frac{1}{\varepsilon\left(k_\perp, \omega; k_z = \frac{\omega}{v}\right)} - 1\right], \tag{3.4}$$

where ρ and z are cylindrical coordinates referred to the direction of motion, and $k_\perp$ and k_z are components of the wave vector $\boldsymbol{k}$ in the plane perpendicular to the direction of motion and in the direction of motion, respectively.

The salient features of the full quantum expression for $\varepsilon(\boldsymbol{k},\omega)$ in metals can be retained by using the plasmon pole approximation[32-34]

$$\varepsilon(k, \omega) = 1 + \frac{\omega_p^2}{\beta^2 k^2 + \frac{1}{4}k^4 - \omega(\omega + i\gamma)} \ , \tag{3.5}$$

where γ is an effective damping constant, and ω_p represents the classical plasma frequency of a free electron gas with equivalent one-electron radius r_s:

$$\omega_p = (3/r_s^3)^{1/2} \quad . \tag{3.6}$$

The constant β is the velocity of propagation of density disturbances in an electron gas, v_F being the Fermi velocity of electrons in the medium:

$$\beta = \left(\frac{3}{5}\right)^{1/2} v_F \, . \tag{3.7}$$

Substitution of eq. (3.5) into (3.4) yields the electron density fluctuation[18]

$$\delta n(\rho, z) = \delta n_1(\rho, z) + \delta n_2(\rho, z) \, , \tag{3.8}$$

where

$$\delta n_1(\rho, z) = -\frac{Z\omega_p^2}{\sqrt{2}\pi} \int_0^{Q_c} dQ \; Q J_0(\sqrt{2}\, Q\rho) \; \frac{\sin\left(\sqrt{2(\alpha \pm \xi)}\; \tilde{z}\right)}{\xi\sqrt{\alpha \pm \xi}} \tag{3.9}$$

and

$$\delta n_2(\rho, z) = \frac{Z\omega_p^2}{2\sqrt{2}\pi} \int_{Q_c}^{\infty} dQ\, Q J_0(\sqrt{2}\, Q\rho) \frac{e^{-\sqrt{2}\,\delta|\tilde{z}|}}{\gamma\delta} \frac{\gamma\cos(\sqrt{2}\,\gamma|\tilde{z}|) + \delta\sin(\sqrt{2}\,\gamma|\tilde{z}|)}{G}, \tag{3.10}$$

with

$$\tilde{z} = z - vt \quad . \tag{3.11}$$

In these expressions,

$$Q_c = \frac{1}{\sqrt{2}\, v}\left[(v^2 - \beta^2)^2 - \omega_p^2\right]^{1/2} , \tag{3.12}$$

$$\alpha = v^2 - \beta^2 - Q^2 \, , \tag{3.13}$$

$$\xi = \left[(v^2 - \beta^2)^2 - 2v^2Q^2 - \omega_p^2\right]^{1/2} , \tag{3.14}$$

$$\gamma = \frac{1}{\sqrt{2}}\sqrt{G + \alpha} \quad , \tag{3.15}$$

$$\delta = \frac{1}{\sqrt{2}}\sqrt{G - \alpha} \tag{3.16}$$

and

$$G = (Q^4 + 2\beta^2 Q^2 + \omega_p^2)^{1/2} . \tag{3.17}$$

The notation "±" means that when $\tilde{z} > 0$ "+" is to be used; similarly, "-" is to be used when $\tilde{z}$

< 0.

Eq. (3.8) is exactly the result obtained in the plasmon pole approximation when the induced electron density fluctuations are related to the wake potential by Poisson equation, being the wake potential equal to the mean value of the scalar potential of the interaction between the moving particle and the plasma, with the interaction hamiltonian given by[37]

$$H_i = \sum_k g_k f_k(t) (b_k + b^+_{-k}) \quad , \tag{3.18}$$

where

$$f_k(t) = -Z\, e^{i\, k.v\, t} \tag{3.19}$$

and

$$g_k = \left(\frac{2\,\pi\,\omega_p^2}{k^2\, V\, \omega_k} \right)^{1/2} \quad , \tag{3.20}$$

as shown by Echenique and Ritchie[35,36]. In these expressions V is the normalization volume, b_k^+ and b_k are the plasmon creation and annihilation operators, and ω_k represents the energy difference between the excited state and the ground state, which is, in the plasmon pole approximation, unique for a given k and given by

$$\omega_k = \left(\omega_p^2 + \beta^2 k^2 + \frac{1}{4} k^4 \right)^{1/2} \quad . \tag{3.21}$$

Consequently, when swift diclusters, each ion having charge Z and constant velocity v, penetrate solid targets the density fluctuation induced by the leading ion at the position of the trailing ion is given, in the plasmon-pole approximation, by eq. (3.8), where

$$\rho = R\, sin\, \theta \tag{3.22}$$

and

$$\hat{z} = -R\, cos\, \theta \quad . \tag{3.23}$$

R is the distance between the pair of ions of the dicluster, which is assumed to be constant, and θ is the angle formed by the molecular axis of the projectile with the beam axis (see fig. 3.1). Fig. 3.2 shows plots of the electron density fluctuation calculated in this way, as a function of the angle θ, for $R = 2.2a_0$, $r_s = 1.53a_0$ and different constant velocities of the

projectile.

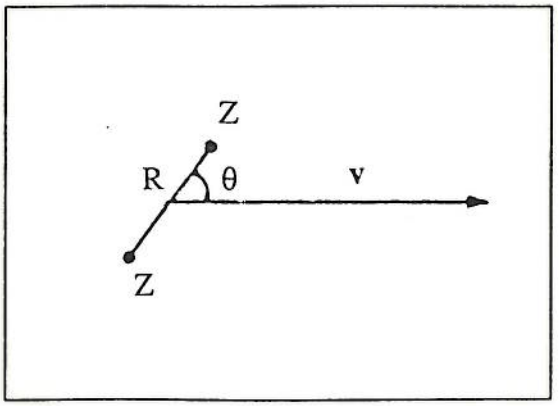


Fig. 3.1. Geometry of the bombarding dicluster, each ion having charge Z and velocity $\boldsymbol{v}$. R is the distance between the pair of ions, and θ is the angle formed by the molecular axis of the dicluster with the beam axis.

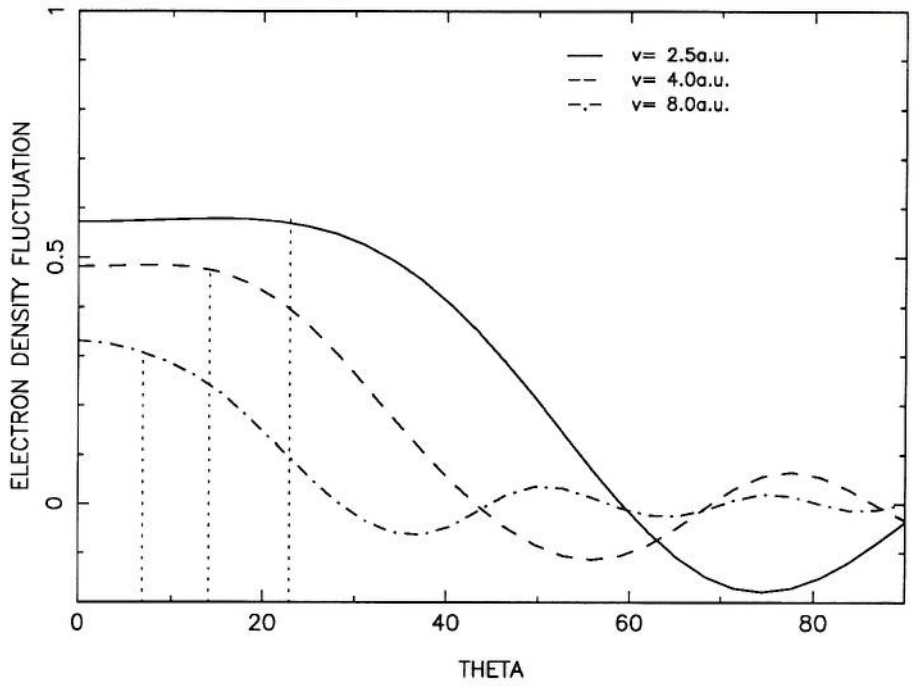


Fig. 3.2. Electron density fluctuation per unit electron density and unit charge induced at the position of the trailing ion by the leading ion, as a function of the orientation θ of bombarding diclusters moving with velocity $v = 2.5$a.u. (solid curve), $v = 4.0$a.u. (dashed curve) and $v = 8.0$a.u. (dashed-dotted curve); the medium is characterized by a density parameter $r_s = 1.53a_0$. Also shown are the corresponding angles $\theta = \sin^{-1}(\beta/v)$ (vertical dotted lines).

The electron density fluctuation of target valence electrons in the position of the trailing ion is most prominent when the trailing ion is in the conical region behind the leading ion with

half-angle of opening $\theta \approx \sin^{-1}(\beta / v)$, which defines the envelope of the collective wake. Consequently, the yield of knock-on electrons produced by the trailing ion should be sensitive to the density fluctuation of target valence electrons, and these experimental data might be used to study the electron polarization wake, as suggested by Yamazaki[28]. Hence, Yamazaki and coworkers have measured the yield of knock-on electrons emitted at 0° with respect to the beam axis from carbon foils bombarded by 4.5MeV N_2^+ ions ($v = 2.5$a.u.), as a function of the orientation of the projectiles, and have found that the electron yield decreases as θ increases, which is qualitatively in agreement with the results of fig. 3.2.

Nevertheless, it is not well-known what the relationship between the yield of knock-on electrons and the electron density fluctuations of the target is; moreover, the cross sections of 0° knock-on electrons also depend on the orientation of the bombarding diclusters, even when there is not any valence electron density fluctuation in the target. Consequently, in order to give an interpretation of such experiments it is necessary to study in detail the result of the multiple scattering involved in the interaction of swift diclusters with matter leading to knock-on electron emission.

The following sections attempt to study in detail the dependence of multiple scattering effects on the orientation of bombarding diclusters, by means of second order perturbation theory and also combining scattering theory with methods developed in the theory of low energy electron diffraction (LEED).

3.3. Scattering of electrons by swift diclusters penetrating matter: perturbation theory approach

We consider a solid target and the process of valence electrons being scattered by the passage of swift dimolecular clusters, each ion having charge Z and velocity $\boldsymbol{v}$, as shown in fig. 3.1; R is the distance between the pair of ions of the dicluster, and θ is the angle between the molecular axis of the projectile and the beam axis. Treating the ion as infinitely massive, we work in the projectile inertial frame.

Assuming that the unscattered wave functions of target valence electrons are plane waves, they may be expanded in partial waves corresponding to given values of the quantum numbers l and m, about the jth ion of the dicluster, as[38]

$$\varphi_{\boldsymbol{k}_i}(\boldsymbol{r}) = \frac{1}{\sqrt{V}} 4\pi \, e^{\boldsymbol{k}_i \cdot \boldsymbol{r}_j} \sum_{l=0}^{\infty} \sum_{m=-l}^{m=l} i^l \, j_l(k\,|\boldsymbol{r} - \boldsymbol{r}_j|) \, Y^*_{lm}(\boldsymbol{k}_i/k) \, Y_{lm}(\boldsymbol{s}_j) \quad , \tag{3.24}$$

where $\boldsymbol{k}_i$ is the momentum of the incident electron, V is the normalization volume, j_l represents the spherical Bessel function of the first kind and lth order[39], k is the momentum modulus of the incident electron, which is constant as far as scattering is assumed to be elastic, $\boldsymbol{r}_j$ is the position vector of the jth ion of the dicluster, Y_{lm} are the spherical harmonics, and

$$\boldsymbol{s}_j = \frac{\boldsymbol{r} - \boldsymbol{r}_j}{|\boldsymbol{r} - \boldsymbol{r}_j|} \quad . \tag{3.25}$$

As a result of the interaction with bombarding diclusters, the wave functions of target valence electrons are no longer plane waves; instead, they are the solution of the Schrödinger equation corresponding to the potential created by the dicluster. If the potential created by each ion of the dicluster were the Coulomb bare potential, the Schrödinger equation could be expressed in prolate spheroidal coordinates and the spheroidal phase shifts and scattering amplitudes could be computed[40-46], though it would be a cumbersome task.

However, the Coulomb potential of the ions is screened by the polarization of the medium and the scattering between bombarding diclusters and target valence electrons is not exactly solvable. Thus with the aim of calculating the scattering amplitudes of this interaction process, first of all we consider the scattering of target valence electrons from two independent

ions, and then approximate the multiple scattering effects within the second Born approximation.

The stationary scattering wave function of target valence electrons in the central potential of each ion constituting the bombarding dicluster may be expanded in partial waves as

$$\Psi_{k_i}(r) = e^{i k_i \cdot r_j} \sum_{l=0}^{\infty} \sum_{m=-1}^{m=1} c_{l\,m}(k)\, R_l(k\,,\, |r - r_j|)\, Y_{l\,m}(s_j) \quad , \tag{3.26}$$

where c_{lm} are the expansion coefficients, and R_l are the radial functions; for every radial function we have

$$-\frac{1}{2}\left[\frac{1}{r^2}\frac{d}{dr}\left(r^2\frac{d}{dr}\right) - \frac{l(l+1)}{r^2}\right] R_l(k\,,\, r) + U(r)\, R_l(k\,,\, r) = E\, R_l(k\,,\, r) \quad . \tag{3.27}$$

The screened potential $U(r)$ created by each ion satisfies the condition

$$\lim_{r \to \infty} |U(r)| < \frac{M}{r^{1+\varepsilon}} \quad , \tag{3.28}$$

where M is some constant and $\varepsilon > 0$. Therefore, out of the range of the potential the general solution of eq. (3.27) may be expressed as[47]

$$R_l(k\,,\, r) = C_l^{(1)}(k)\, j_l(k\, r) + C_l^{(2)}(k)\, n_l(k\, r) \quad , \tag{3.29}$$

where j_l and n_l are spherical Bessel functions of the first and second kind, respectively, and

$$\tan \delta_l(k) = - C_l^{(2)}(k) / C_l^{(1)}(k) \quad , \tag{3.30}$$

the quantities δ_l being the phase shifts, which display the influence of the interaction. Substituting eq. (3.30) into eq. (3.29) one finds, in terms of spherical Hankel functions of the first and second kind,

$$R_l(k\,,\, r) = D_l(k)\left[e^{2 i \delta_l} h_l^{(1)}(k\, r) + h_l^{(2)}(k\, r)\right] \quad , \tag{3.31}$$

where the quantities D_l are some functions of k.

Introducing eq. (3.31) into eq. (3.26) and taking advantage of the relationship between the spherical Bessel functions of the first kind and the spherical Hankel functions of the first and second kind, the scattering wave function may be expressed, out of the range of the potential, as

$$\Psi_{k_i}(r) = \varphi_{k_i}(r) + \Psi^{(s)}_{k_i}(r) \quad , \tag{3.32}$$

where $\varphi_{ki}(r)$ is the unscattered wave function,

$$\varphi_{k_i}(r) = e^{i k_i \cdot r_j} \sum_{l=0}^{\infty} \sum_{m=-l}^{m=l} d_{lm}(k)\, j_l(k\,|r - r_j|)\, Y_{lm}(s_j) \quad , \tag{3.33}$$

and $\Psi^{(s)}_{ki}(r)$ is the scattered wave function,

$$\Psi^{(s)}_{k_i}(r) = e^{i k_i \cdot r_j} \sum_{l=0}^{\infty} \sum_{m=-l}^{m=l} d_{lm}(k)\, \frac{e^{2 i \delta_l} - 1}{2}\, h_l^{(1)}(k\,|r - r_j|)\, Y_{lm}(s_j) \quad . \tag{3.34}$$

Comparing eqs. (3.24) and (3.33), one finds the values of the coefficients d_{lm}, thus rewriting eq. (3.34) as

$$\Psi^{(s)}_{k_i}(r) = \frac{1}{\sqrt{V}}\, 4\pi\, e^{i k_i \cdot r_j} \sum_{l=0}^{\infty} \sum_{m=-l}^{m=l} i^l\, \frac{e^{2 i \delta_l} - 1}{2}\, h_l^{(1)}(k\,|r - r_j|)\, Y^*_{lm}(k_i/k)\, Y_{lm}(s_j), \tag{3.35}$$

which for large r is given by

$$\Psi^{(s)}_{k_i}(r) \underset{r \to \infty}{=} \frac{1}{\sqrt{V}}\, e^{i \Delta \cdot r_j}\, f^0(k_i, k_f)\, \frac{e^{i k r}}{r} \quad . \tag{3.36}$$

In this expression, k_f is the momentum of the scattered electron, Δ is the momentum transfer,

$$\Delta = k_i - k_f \quad , \tag{3.37}$$

and $f^0(k_i,k_f)$ represents the scattering amplitude,

$$f^0(k_i, k_f) = \frac{4\pi}{k} \sum_{l=0}^{\infty} \sum_{m=-l}^{m=l} \frac{e^{2 i \delta_l} - 1}{2 i}\, Y^*_{lm}(k_i/k)\, Y_{lm}(k_f/k) \quad . \tag{3.38}$$

Choosing the z-axis along the direction of k_i, eq. (3.38) may also be written as

$$f^0(k_i, k_f) = \frac{1}{k} \sum_{l=0}^{\infty} (2l + 1)\, \frac{e^{2 i \delta_l} - 1}{2 i}\, P_l(\cos\theta) \quad , \tag{3.39}$$

where θ is the angle between k_i and k_f, and the quantities P_l are the Legendre polinomials.

Consequently, if scattering were sufficiently weak for multiple scattering to be neglected, the differential scattering cross section of target valence electrons in the potential of the bombarding diclusters would be

$$\frac{d\sigma}{d\Omega} = \left| \left(1 + e^{i \Delta \cdot R}\right)\, f^0(k_i, k_f) \right|^2 \quad , \tag{3.40}$$

where $\boldsymbol{R}$ represents the position vector of the leading ion with respect to the trailing ion. It is interesting to observe that even when multiple scattering effects are neglected the differential scattering cross section strongly depends on the orientation of the bombarding diclusters. In particular, the differential scattering cross section of electrons emitted at 0° with respect to the beam axis is maximum when the bombarding dicluster is orientated in a plane perpendicular to the beam axis, and there can be other maxima for different orientations depending on the velocity and the internuclear distance of the projectiles.

In cases where scattering is strong enough there are other large contributions to the scattering cross section, since the electronic flux scattered by one ion can incide on the other ion scattering again, and so on. Thus the incident electronic wave on each ion is no longer an unscattered plane wave; instead, it is the superposition of the unscattered wave and the scattered wave resulting from a multiple scattering process. Now we approximate these multiple scattering effects within the second Born approximation.

Second Born approximation

The stationary scattering wave function, solution of the time-independent Schrödinger equation of a target valence electron in the potential $U(\boldsymbol{r})$ can be written as[48]

$$\Psi_{\mathbf{k}_i}(\boldsymbol{r}) = \varphi_{\mathbf{k}_i}(\boldsymbol{r}) + 2\int d\boldsymbol{r}' G_0^{(+)}(\boldsymbol{r}, \boldsymbol{r}')\, U(\boldsymbol{r}')\, \Psi_{\mathbf{k}_i}(\boldsymbol{r}') \quad , \tag{3.41}$$

where $\varphi_{ki}(\mathbf{r})$ is the incident plane wave, and $G_0(\boldsymbol{r},\boldsymbol{r}')$ is the outgoing Green function

$$G_0^{(+)}(\boldsymbol{r}, \boldsymbol{r}') = -(2\pi)^{-3} \lim_{\varepsilon \to 0^+} \int \frac{e^{i\boldsymbol{k}'\cdot(\boldsymbol{r}-\boldsymbol{r}')}}{k'^2 - k^2 - i\varepsilon}\, d\boldsymbol{k}' \quad . \tag{3.42}$$

Eq. (3.41) is the Lippman-Schwinger equation of potential scattering. For large distances the scattering wave function (3.41) can be expressed as eq. (3.32), where the scattered wave function is

$$\Psi_{\boldsymbol{k}_i}^{(s)}(\boldsymbol{r}) \underset{r\to\infty}{=} \frac{1}{\sqrt{V}} f(\boldsymbol{k}_i, \boldsymbol{k}_j) \frac{e^{ikr}}{r} \quad , \tag{3.43}$$

and

$$f(\boldsymbol{k}_i, \boldsymbol{k}_f) = -\frac{V}{2\pi} <\varphi_{\boldsymbol{k}_f} | U | \Psi_{\boldsymbol{k}_i}> \ . \tag{3.44}$$

The Lippman-Schwinger equation can be solved by iteration, starting with the plane wave $\varphi_{\boldsymbol{k}i}(\mathbf{r})$ as the zero order approximation; then substituting the scattering wave function $\Psi_{\boldsymbol{k}i}(\mathbf{r})$ into eq. (3.44), one would find the Born series for the scattering amplitude in powers of the potential . Instead, if the first order approximation of the scattering wave function is introduced into eq. (3.44), one finds the second Born approximation for the scattering amplitude:

$$f_{B_2} = -\frac{V}{2\pi}\left[< \varphi_{\boldsymbol{k}_f} | U | \varphi_{\boldsymbol{k}_i} > + 2 < \varphi_{\boldsymbol{k}_f} | U\, G_0^{(+)}\, U | \varphi_{\boldsymbol{k}_i} > \right] , \tag{3.45}$$

or, substituting eq. (3.42) into eq. (3.45),

$$f_{B_2} = -\frac{V}{2\pi}\left[< \varphi_{\boldsymbol{k}_f} | U | \varphi_{\boldsymbol{k}_i} > - \frac{V}{4\pi^3}\int d\boldsymbol{q}\, \frac{< \varphi_{\boldsymbol{k}_f} | U | \varphi_{\boldsymbol{q}} > < \varphi_{\boldsymbol{q}} | U | \varphi_{\boldsymbol{k}_i} >}{q^2 - k^2 - i\,0^+} \right] . \tag{3.46}$$

This result can also be obtained by means of time-dependent perturbation theory, when the perturbation is assumed to be constant in time except for being turned on as $t \rightarrow -\infty$ and off as $t \rightarrow +\infty$[49].

The potential of the bombarding dicluster is

$$U(\boldsymbol{r}) = U_1(\boldsymbol{r}) + U_1(\boldsymbol{r} + \boldsymbol{R}) \ , \tag{3.47}$$

where $U_1(\boldsymbol{r})$ and $U_1(\boldsymbol{r} + \boldsymbol{R})$ represent the potentials created by the trailing ion and the leading ion of the dicluster, respectively. For high momentum transfers, the wake potential of swift ions may be approximated by a spherically symmetric form of the total potential that electrons in the medium feel, that is, a velocity dependent Yukawa potential

$$U_1(\boldsymbol{r}) \ = -\frac{Z}{r}\, e^{-\alpha r} , \tag{3.48}$$

where

$$\alpha = \frac{\omega_p}{v} \ . \tag{3.49}$$

Here ω_p is the plasmon frequency given by eq. (3.6), and v is the velocity of the projectile.

Substituting eq. (3.48) into eq. (3.46) leads, after some algebra, the following result

$$f_{B_2}(\boldsymbol{k}_i, \boldsymbol{k}_f) = \left(1 + e^{i\,\boldsymbol{\Delta}.\boldsymbol{R}}\right) f^{0}_{B_2}(\boldsymbol{k}_i, \boldsymbol{k}_f) + f'(\boldsymbol{k}_i, \boldsymbol{k}_f) \ , \tag{3.50}$$

where $\boldsymbol{\Delta}$ is given by eq. (3.37), and $f^{\circ}_{B2}(\boldsymbol{k}_i, \boldsymbol{k}_f)$ is the second Born scattering amplitude of electrons in the potential of eq. (3.48) created by a point charge of magnitude Z moving with velocity $\boldsymbol{v}$ through the target (see Appendix):

$$f^{0}_{B_2} = \frac{2Z}{\Delta^2 + \alpha^2} + \frac{(2Z)^2}{\Delta\,\Gamma}\left[\tan^{-1}\frac{\alpha\,\Delta}{2\Gamma} + \frac{1}{2}\,i\ln\frac{\Gamma + k\,\Delta}{\Gamma - k\,\Delta}\right], \tag{3.51}$$

where

$$\Gamma = \left[\alpha^4 + k^2\,(4\,\alpha^2 + \Delta^2)\right]^{1/2} \ . \tag{3.52}$$

$f'(\boldsymbol{k}_i, \boldsymbol{k}_f)$ represents the scattering amplitude related to first order multiple scattering effects:

$$f' = \frac{2Z^2}{\pi^2}\int \frac{d\boldsymbol{q}}{q^2 - k^2 - i\,0^+}\,\frac{e^{-i\,(\boldsymbol{k}_i - \boldsymbol{q}).\boldsymbol{R}} + e^{-i\,(\boldsymbol{q} - \boldsymbol{k}_f)\,.\,\boldsymbol{R}}}{\left(\alpha^2 + |\boldsymbol{k}_i - \boldsymbol{q}|^2\right)\left(\alpha^2 + |\boldsymbol{q} - \boldsymbol{k}_f|^2\right)} \ . \tag{3.53}$$

In the case of a swift charge particle moving with velocity exceeding the Fermy velocity, $k/\alpha >> 1$ for typical electron densities of the target, and the criterion for convergence of the Born series becomes

$$\frac{Z}{k}\ln\frac{k}{\alpha} << 1 \ . \tag{3.54}$$

Thus we expect the Born approximation to be valid for large incident velocities and small charges. In fig. 3.3 we compare the second order differential scattering cross section of electrons in the central potential created by a single ion, deduced squaring the modulus of the scattering amplitude (3.51), with the well known first order differential scattering cross section and the exact result, when $\boldsymbol{k}_i$ and $\boldsymbol{k}_f$ are taken to be $-\boldsymbol{v}$ and $\boldsymbol{v}$, respectively.

Fig. 3.3 shows that the second Born approximation offers no improvement over the first Born approximation, even at high velocities for which we would expect the Born series to converge rapidly. The reason for this failure of the second Born approximation has been pointed out by Joachain[50], noting that the second order differential scattering cross section does not account for all second order corrections in k to the first order differential cross section. Consequently, when scattering of electrons in the potential of eq. (3.47) is considered, instead of approximating the exact scattering amplitude by the second Born

scattering amplitude of eq. (3.50), we approximate it by

$$f(\boldsymbol{k}_i , \boldsymbol{k}_f) = \left(1 + e^{i\,\Delta.R}\right) f^0(\boldsymbol{k}_i , \boldsymbol{k}_f) + f'(\boldsymbol{k}_i , \boldsymbol{k}_f) \ , \tag{3.55}$$

where f^0 is the exact scattering amplitude of eq. (3.39) of electrons in the central velocity dependent Yukawa potential of a single ion, and f', given by eq. (3.53), accounts for the first order multiple scattering effects. Therefore, in this approximation we have

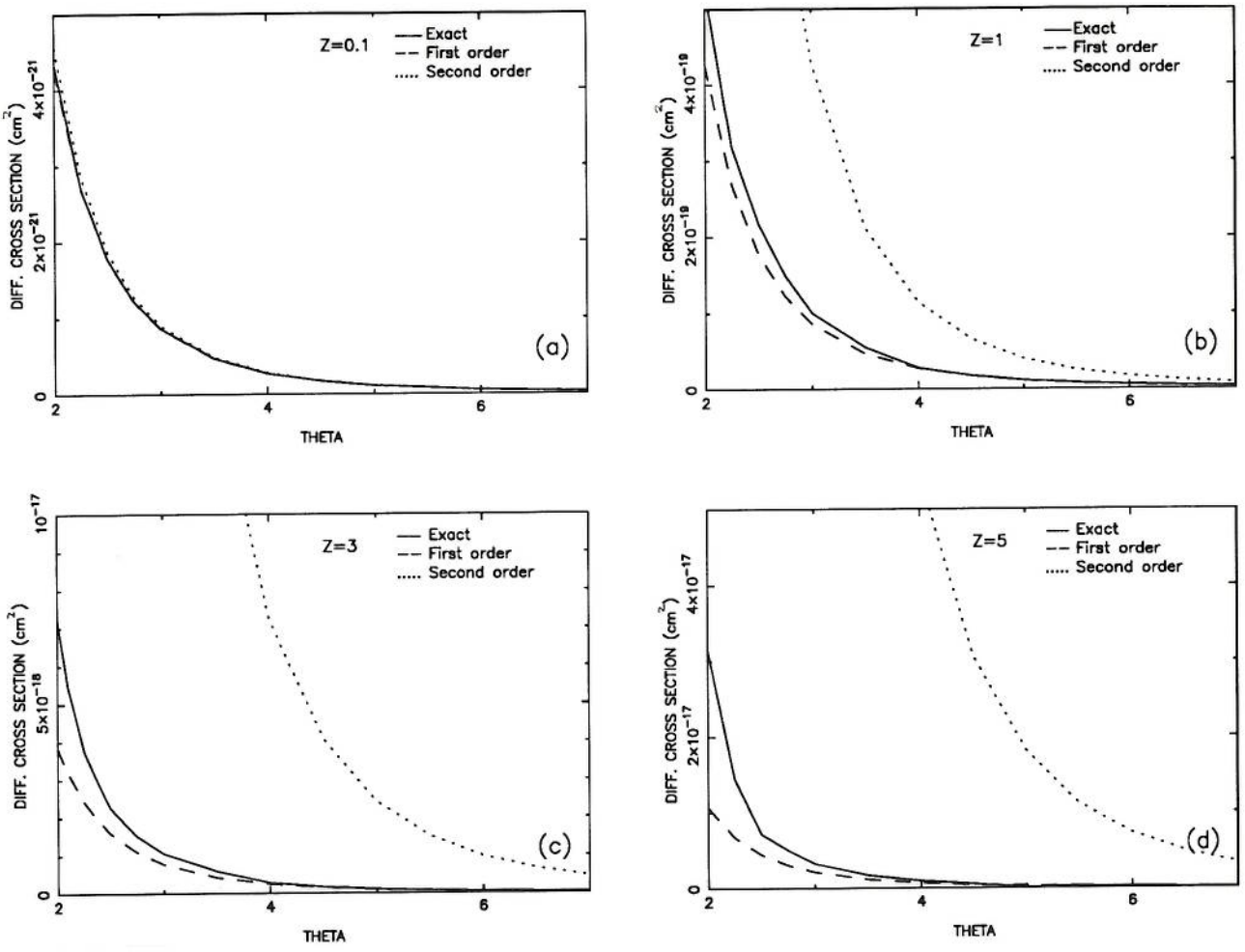


Fig. 3.3. Calculations of the differential scattering cross section, versus v, of electrons in the central potential of eq. (3.48), deduced squaring the modulus of the exact scattering amplitude of eq. (3.39) (solid curves), together with the first and second order differential scattering cross sections deduced for the same potential squaring the first term and the modulus of the whole scattering amplitude of eq. (3.51), respectively (dashed and dotted curves); $\boldsymbol{k}_i$ and $\boldsymbol{k}_f$ have been taken to be $-\boldsymbol{v}$ and $\boldsymbol{v}$, respectively, and different values of Z have been considered: 0.1 (fig. 33a), 1 (fig. 3.3b), 3 (fig. 3.3c) and 5 (fig. 3.3d). The exact differential scattering cross sections have been obtained computing the phase shifts by numerical integration of the radial Schrödinger equation through the velocity dependent Yukawa potential of eq. (2.48).

$$\frac{d\sigma}{d\Omega} = \left| \left(1 + e^{i \Delta . R}\right) f^{0}(k_i , k_f) + f'(k_i , k_f) \right|^2 . \qquad (3.56)$$

It is well known that

$$\lim_{\varepsilon \to 0^+} \frac{1}{x - i\,\varepsilon} = PP \frac{1}{x} + i\,\pi\,\delta(x) , \qquad (3.57)$$

where PP denotes the Cauchy principal part; therefore, eq. (3.53) can be rewritten as

$$f' = \frac{2Z^2}{\pi^2} \left[\int_0^{\infty} PP \frac{g(q)}{q^2 - k^2} dq + i\,\pi \frac{g(k)}{2k} \right] , \qquad (3.58)$$

where

$$g(q) = \int d\Omega \frac{e^{-i(k_i - q).R} + e^{-i(q - k_f).R}}{\left(\alpha^2 + |k_i - q|^2\right)\left(\alpha^2 + |q - k_f|^2\right)} , \qquad (3.59)$$

Ω representing the solid angle defining the direction of q. When target valence electrons having zero velocity in the laboratory system are considered $k_i = -v$, thus the differential scattering cross section of knock-on electrons emitted at 0° with respect to the beam axis being that of eq. (3.56) with

$$g(q) = 4\,\pi q^2 e^{i\,v R \cos\theta} \int_{-1}^{1} dv \frac{J_0\left[q R \sqrt{1 - v^2}\,\sin\theta\right] \cos(q R\, v \cos\theta)}{(\alpha^2 + q^2 + v^2)^2 - 4\, v^2 q^2 v^2} , \qquad (3.60)$$

where θ is the angle between R and v, and J_0 is the zero order Bessel function of the first kind.

Figs. 3.4 and 3.5 exhibit plots of the differential scattering cross section (3.56) of electrons being initially at rest in the laboratory frame to be emitted at 0° with respect to the beam axis, as a function of θ, together with the simple differential scattering cross section of eq. (3.40) which neglects multiple scattering effects. In fig. 3.4 the charge and internuclear distance have been taken to be Z = 1and R = 2.2a.u., and different values of the velocity have been considered; in fig. 3.5 the velocity has been taken to be v = 2.5a.u. and different values of the charge Z and internuclear distance R have been considered.

Figs. 3.4 and 3.5 show that even when multiple scattering is neglected, the dependence of the differential scattering cross section on the orientation of diclusters is important, as

pointed out above. Indeed, when $\boldsymbol{k}_i$ and $\boldsymbol{k}_f$ are taken to be $-\boldsymbol{v}$ and $\boldsymbol{v}$, respectively, eq. (3.40) may be expressed as

$$\left(\frac{d\sigma}{d\Omega}\right)^{0} = 2\left[1 + \cos\left(2\, v R\, \cos\theta\right)\right]\left|f^{0}(-\boldsymbol{v}, \boldsymbol{v})\right|^{2}; \tag{3.61}$$

thus the dependence of the yield of 0° knock-on electrons on the orientation of bombarding diclusters presents oscillatios, which depend on the velocity and internuclear distance of the projectiles.

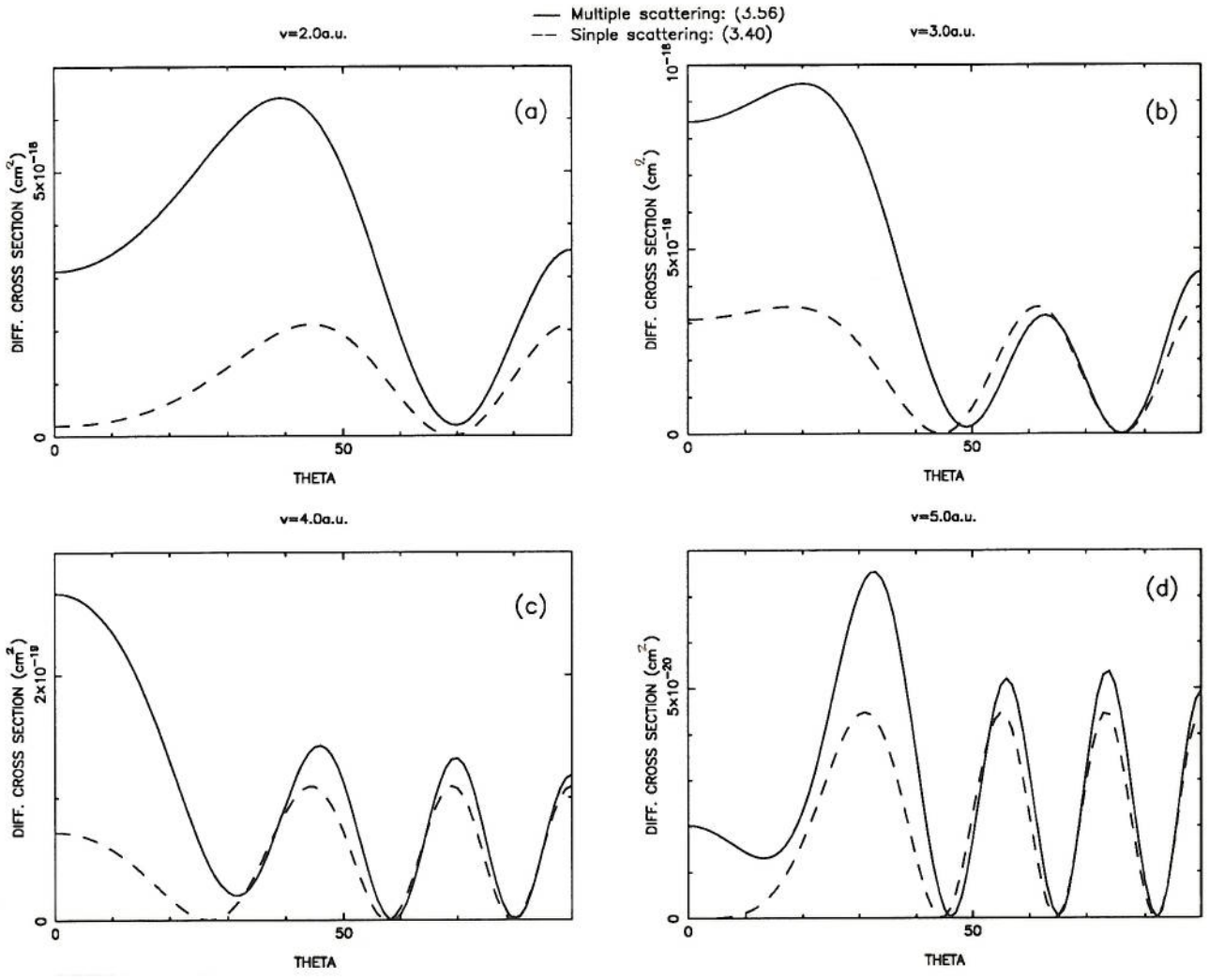


Fig. 3.4. Differential scattering cross sections deduced from eq. (3.40) (dashed curves) and eq. (3.56) (solid curves), as a function of the orientation of bombarding diclusters moving with velocity v = 2.0a.u. (fig. 3.4a), v = 3.0a.u. (fig. 3.4b), v = 4.0a.u. (fig. 3.4c) and v = 5.0a.u. (fig. 3.4d), when $\boldsymbol{k}_i$, $\boldsymbol{k}_f$, Z and R are taken to be $-\boldsymbol{v}$, $\boldsymbol{v}$, 1 and 2.2a.u., respectively.

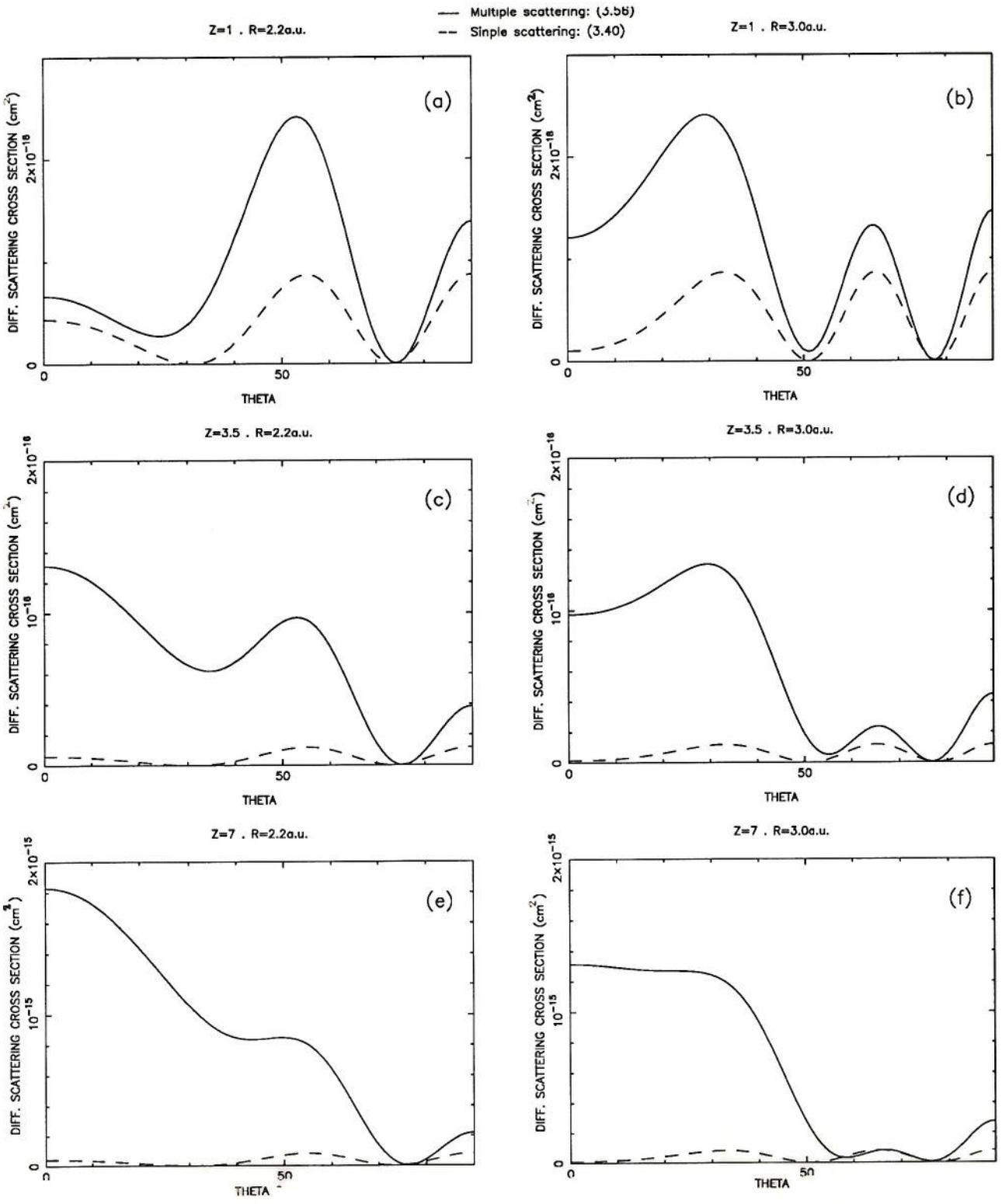


Fig. 3.5. Differential scattering cross sections deduced from eq. (3.40) (dashed curves) and eq. (3.56) (solid curves), as a function of the orientation of bombarding diclusters moving with velocity v = 2.5a.u., when k_i and k_f are taken to be -v and v, and different values of the charge and internuclear distance are considered: Z = 1, R = 2.2a.u.(fig. 3.5a), Z = 1, R = 3.0a.u. (fig. 3.5b), Z = 3.5, R = 2.2a.u. (fig. 3.5c), Z = 3.5, R = 3.0a.u. (fig. 3.5d), Z = 7 , R = 2.2a.u. (fig. 3.5e) and Z = 7, R = 3.0a.u. (fig. 3.5f).

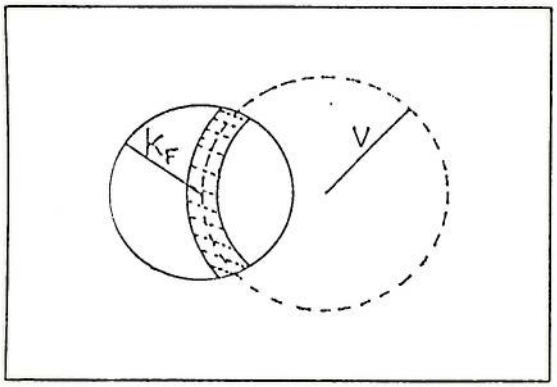
Figs. 3.4 and 3.5 also show that as a result of including multiple scattering by means of the first order multiple scattering amplitude f' of eq. (3.58) the electron yield decreases as θ increases, in qualitative agreement with experiment, especially for high values of Z where multiple scattering becomes more important.

Initial momentum distribution of target valence electrons

When bombarding diclusters penetrate condensed matter, the different contributions to the emission yield coming from all allowed initial states must be taken into account. In particular, if electrons emitted at 0° with respect to the beam axis in a velocity region of $\lambda_1 v \leq k_f \leq \lambda_2 v$ are considered, the only contributions to the emission yield come from initial target electrons having in the laboratory system some momentum confined to the dashed region of k-space represented in fig. 3.6, whenever $v - k_F \leq \lambda_1 v$ and $\lambda_2 v \leq v + k_F$, k_F being the Fermi momentum of the target

$$k_F = \frac{(9\pi/4)^{1/3}}{r_s}, \tag{3.62}$$

and the quantities λ_1 and λ_2 representing positive constants.



3.6 irudia. Initial momentum distribution of target valence electrons having non-zero probability of being emitted at 0° with respect to the beam axis in a velocity region of $\lambda_1 v \leq k_f \leq \lambda_2 v$. Assuming that $v - k_F \leq \lambda_1 v \leq v$ and $v \leq \lambda_2 v \leq v + k_F$, this distribution can be represented by the region of k-space delimited by the Fermi sphere of radius k_F and the spherical surfaces of radii $\lambda_1 v$ and $\lambda_2 v$.

The differential scattering cross section per target valence electron of knock-on electrons emitted at 0° in a velocity region of $\lambda_1 v \le k_f \le \lambda_2 v$ can be calculated just by integrating over all allowed initial states and dividing by the valence electron density of the target. Choosing the z-axis along the direction of -$\mathbf{v}$, we find

$$\frac{d\sigma}{d\Omega} = \frac{3}{4\pi k_F^3 v} \int_{k_{min}}^{k_{max}} dk\, k^3 \int_{\mu_{min}}^{1} d\mu \int_0^{2\pi} d\varphi\, |f(k, \mu, \varphi)|^2 \quad , \tag{3.63}$$

where k, μ and φ are polar coordinates of $\mathbf{k}_i$. In this expression we have

$$k_{min} = \max (v - k_F, \lambda_1 v) \quad , \tag{3.64}$$

$$k_{max} = \min (v + k_F, \lambda_2 v) \quad , \tag{3.65}$$

$$\mu_{min} = \frac{k^2 + v^2 - k_F^2}{2 k v} \quad , \tag{3.66}$$

and $f(k, \mu, \varphi)$ is the scattering amplitude of electrons having initial momentum $\mathbf{k}_i(k, \mu, \varphi)$, i.e.

$$f(k, \mu, \varphi) = \left\{ 1 + e^{-ikR\left[(1+\mu)\cos\theta - \sqrt{1-\mu^2}\cos\varphi \sin\theta\right]} \right\} f^0(k, \mu, \varphi) + f'(k, \mu, \varphi) \quad , \tag{3.67}$$

where

$$f^0(k, \mu, \varphi) = \frac{1}{k} \sum_{l=0}^{\infty} (2l+1) \frac{e^{2i\delta_l} - 1}{2i} P_l(-\mu) \tag{3.68}$$

and

$$f'(k, \mu, \varphi) = \frac{2Z^2}{\pi^2} \left[\int_0^{\infty} PP \frac{g(q, \mu, \varphi)}{q^2 - k^2} dq + i\pi \frac{g(k, \mu, \varphi)}{2k} \right] . \tag{3.69}$$

In these expressions the quantities δ_l are the phase shifts accounting for the interaction with a single ion of the dicluster, which are computed solving numerically the radial Schrödinger equation. We have also

$$g(q, \mu, \varphi) = q^2 \int_{-1}^{1} dv \int_0^{2\pi} d\varphi' \frac{e^{-i\xi_1 R} + e^{i\xi_2 R}}{A} \quad , \tag{3.70}$$

$$\xi_1 = (qv - k)\cos\theta + q(1 - v^2)^{1/2} \cos\varphi' \sin\theta \quad , \tag{3.71}$$

$$\xi_2 = (k \mu + q \nu) \cos \theta + \left[k (1 - \mu^2)^{1/2} \cos \varphi - q (1 - \nu^2)^{1/2} \cos \varphi' \right] \sin \theta , \quad (3.72)$$

$$A = (\alpha^2 + q^2 + k^2)^2 - 2 k q (\alpha^2 + q^2 + k^2) (\nu + B) + 4 k^2 q^2 \nu B \quad (3.73)$$

and

$$B = - \mu \nu + (1 - \mu^2)^{1/2} (1 - \nu^2)^{1/2} \cos(\varphi - \varphi') . \quad (3.74)$$

In particular, if we assume that all non-zero emission probabilities of target valence electrons are equal to the emission probability of electrons having zero velocity in the laboratory system, we find

$$\frac{d\sigma}{d\Omega} = \frac{3}{4 \pi k_F^3} V_k \left| \left(1 + e^{-2 i \nu R \cos \theta}\right) f^0(\nu , 1) + f'(\nu , 1) \right|^2 , \quad (3.75)$$

where $f^0(\nu,1)$ and $f'(\nu,1)$ are given by eqs. (3.68) and (3.69), respectively, for $k = \nu$, $\mu = 1$ and any value of φ, and V_k is, assuming that $\nu - k_F \leq \lambda_1 \nu$ and $\lambda_2 \nu \leq \nu + k_F$, the volume of the dashed region of k-space represented in fig. 3.6, i.e.

$$V_k = \pi \nu \left[\frac{(k_F^2 - \nu^2) (\lambda_2^2 - \lambda_1^2)}{2} + \frac{2 \nu^2 (\lambda_2^3 - \lambda_1^3)}{3} - \frac{\nu^2 (\lambda_2^4 - \lambda_1^4)}{4} \right] . \quad (3.76)$$

Yamazaki and coworkers[28] have measured the yield of 0° knock-on electrons emitted from thin carbon foils in the velocity region of $1.95\nu \leq k_f \leq 2.15\nu$ under bombardment of 4.5MeV dinitrogen molecular ions. Therefore, the velocity of bombarding diclusters is v ≈ 2.5a.u., and the charge and internuclear distance of the pair of ions are Z = 1 and R ≈ 2a.u., respectively, before entering the target; however, as they penetrate the target, some of the binding electrons are lost and the resulting fragment ions undergo a Coulomb explosion, so that the effective charge and internuclear distance both change during the experiment and depend on the velocity of diclusters and the thickness of the target.

When swift ions pass through matter their charge state is modified due to successive electron capture and loss processes[51-53], thus becoming, in a short time, an equilibrium charge state. Betz has proposed an empirical formula to give the mean equilibrium charge in the form[51]

$$Z = Z_1 \left[1 - \exp (- \nu Z_1^{-\gamma}) \right] , \quad (3.77)$$

where Z_1 is the bare ion charge and $\gamma \approx 2/3$; hence, the mean charge of the ions constituting 4.5MeV dinitrogen projectiles can be assumed to be $Z \approx 3.5$.

For very thin targets ($d < 100$Å) the internuclear distance of the bombarding dinitrogen clusters can be assumed to be approximately equal to the interatomic distance of N_2 molecules; however, for thicker targets it increases very rapidly. Therefore, we have considered in our calculations different values of the internuclear distance of bombarding diclusters.

In fig 3.7 we plot, as a function of θ, the differential scattering cross section of target valence electrons to be emitted at 0° in he velocity region of $1.95v \leq k_f \leq 2.15v$ calculated from eqs. (3.63) and (3.75) for v= 2.5a.u, Z = 3.5a.u. and two different values of the internuclear distance R. Fig. 3.8 exhibits the experimental yield of 0° knock-on electrons emitted from a 2μg/cm^2 carbon foil ($d \approx 100$Å) under 4.5MeV N_2^+ bombardment measured by Yamazaki[28].

As a result of the contribution from all allowed initial states, the oscillations appearing in the dependence of 0° knock-on electron emission on the orientation of projectiles get less pronounced; this is due to the fact that the value of the angle θ making the emission probability maximum or minimum depends not only on the velocity and internuclear distance of the projectile but also on the momentum of the initial target valence electron, thus becoming different for the different contributions to the total yield. On the other hand, fig. 7 shows that the integrated differential scattering cross section is a decreasing function of θ, which is a consequence of multiple scattering effects, as also shown in figs. 3.4 and 3.5.

The experimental results qualitatively agree with the calculations shown in fig. 3.7: the yield of knock-on electrons emitted in the forward direction has been found to be a decreasing function of θ, and a small peak appears at $\theta \approx 60°$, in agreement with our theoretical calculation obtained for R = 2.2a.u. ; notice that the position of this peak should appear at larger values of θ as R increases, thus depending on the thickness of the target. Nevertheless, the experimental results are not fitted quantitatively by our calculations, since the experimentally observed enhancement of the yield produced by the longitudinally aligned projectiles is not as large as the one predicted by our theoretical results; the discrepancy between our theoretical results and the experimental curve may be a consequence of having

included in our calculations only the first order multiple scattering for projectiles with high effective charge.

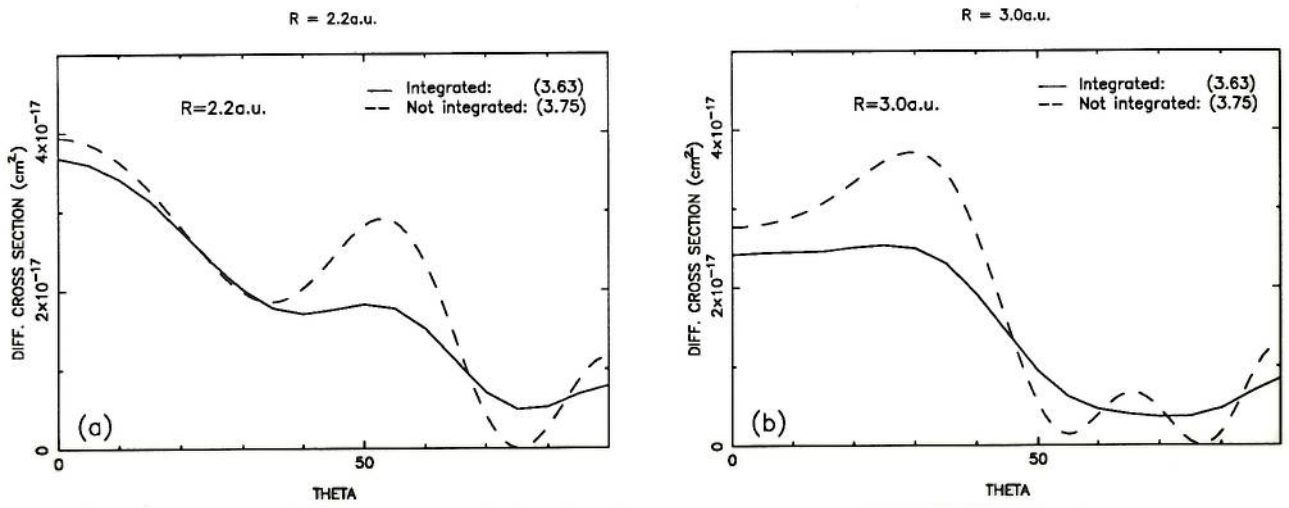


Fig. 3.7. Differential scattering cross section of target valence electrons to be emitted at 0° in the velocity region of of $1.95v \leq k_f \leq 2.15v$ calculated from eqs. (3.63) and (3.75) for $v = 2.5$a.u, $Z = 3.5$a.u. and two different values of the internuclear distance: $R = 2.2$a.u. (fig. 3.7a) and $R = 3.0$a.u. (fig. 3.7b). The electron density parameter $r_s = 1.53$a.u. of carbon has been considered.

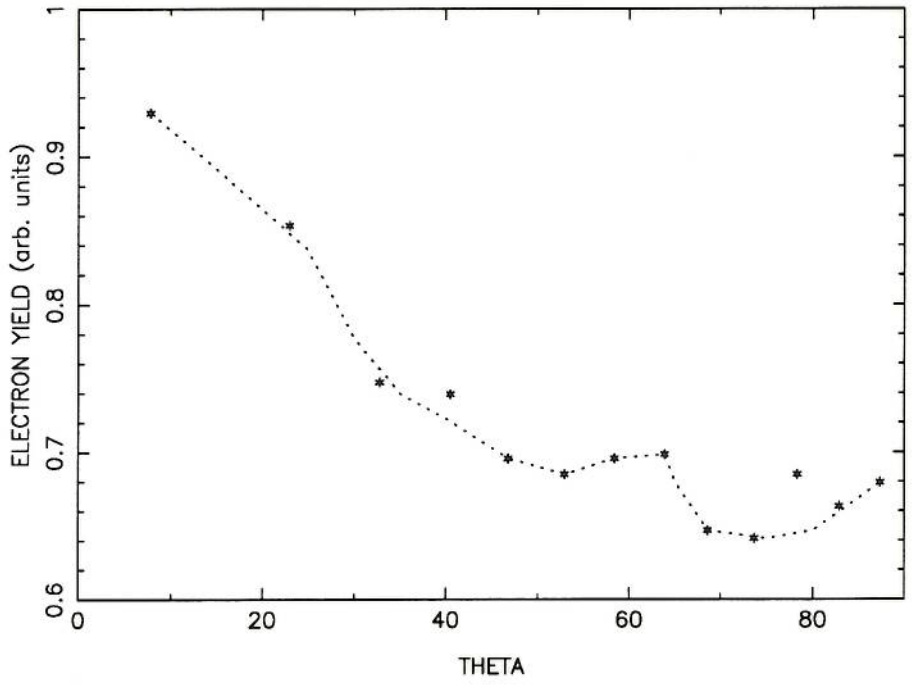


Fig. 3.8. The knock-on electron yield measured by Yamazaki[28] at 0° in the velocity region of $1.95v \leq k_f \leq 2.15v$ as a function of the orientation of 4.5MeV N_2^+ diclusters passing through a 2μg/cm^2 carbon foil.

3.4. Scattering of electrons by swift diclusters penetrating matter: non-perturbative approach

With the aim of studying in detail the total contribution of multiple scattering and its dependence on the orientation of the molecular axis of the projectiles, in this section we combine scattering theory with methods developed in the theory of low energy electron difraction (LEED).

If scattering were sufficiently weak for multiple scattering to be neglected, the incident electronic wave on each ion would be a plane wave, which can be expanded about the *j*th ion of the dicluster as shown in eq. (3.24). This equation may be rewritten as

$$\varphi_{k_i}(r) = \frac{1}{\sqrt{V}} \sum_{l=0}^{\infty} \sum_{m=-l}^{m=l} A^0_{l\,m_j}\, j_l(k\,|r - r_j|)\, Y_{l\,m}(s_j) \quad , \tag{3.78}$$

where

$$A^0_{l\,m_j} = e^{i\,k_i r_j}\, 4\,\pi\, i^l\, Y^*_{l\,m}(k_i / k) \, . \tag{3.79}$$

In these expressions k_i is the momentum of the incident electron with respect to the projectile, k represents the momentum modulus of the incident electron, which keeps constant as far as scattering is elastic, and s_j is given by eq. (3.25). Hence, out of the range of the potential created by the moving ions the scattered wave functions would be given by eq. (3.35), i.e.

$$\Psi^{(s)}_{k_i}(r) = \frac{1}{\sqrt{V}} \sum_{l=0}^{\infty} \sum_{m=-l}^{m=l} A^0_{l\,m_j}\, \frac{e^{2\,i\,\delta_l} - 1}{2}\, h^{(1)}_l(k\,|r - r_j|)\, Y_{l\,m}(s_j) \quad , \tag{3.80}$$

where the quantities δ_l are the phase shifts displaying the influence of the interaction with each ion; then the differential scattering cross section of target valence electrons upon interaction of the bombarding diclusters would be given by eq. (3.40), $\boldsymbol{R}$ being the position vector of the leading ion of the projectile with respect to the trailing ion.

When scattering is strong enough, the incident electronic wave on each ion cannot be approximated by a plane wave, because of the contribution from the electronic flux scattered by the other ion, as pointed out in the preceding section. The total incident electronic wave on the *j*th ion can be written as[54-56]

$$\Psi_{k_i}(\boldsymbol{r}) = \frac{1}{\sqrt{V}} \sum_{l=0}^{\infty} \sum_{m=-l}^{m=l} A_{l m_j} j_l(k\,|\boldsymbol{r} - \boldsymbol{r}_j|)\, Y_{l m}(\boldsymbol{s}_j) \ , \tag{3.81}$$

where $A_{lm\,j}$ is the total amplitude. Thus, out of the range of the potential the scattered wave function can be found as

$$\Psi^{(s)}_{k_i}(\boldsymbol{r}) = \frac{1}{\sqrt{V}} \sum_{l=0}^{\infty} \sum_{m=-l}^{m=l} A_{l m_j} \frac{e^{2 i \delta_l} - 1}{2} h_l^{(1)}(k\,|\boldsymbol{r} - \boldsymbol{r}_j|)\, Y_{l m}(\boldsymbol{s}_j). \tag{3.82}$$

Consequently, as the total incident wave on each ion is the superposition of the unscattered wave and the scattered wave resulting from a multiple scattering process, one finds for the total incident wave on the jth ion

$$\Psi_{k_i}(\boldsymbol{r}) = \frac{1}{\sqrt{V}} \sum_{l=0}^{\infty} \sum_{m=-l}^{m=l} A^0_{l m_j} j_l(k\,|\boldsymbol{r} - \boldsymbol{r}_j|)\, Y_{l m}(\boldsymbol{s}_j)$$

$$+ \frac{1}{\sqrt{V}} \sum_{l=0}^{\infty} \sum_{m=-l}^{m=l} A_{l m_k} \frac{e^{2 i \delta_l} - 1}{2} h_l^{(1)}(k\,|\boldsymbol{r} - \boldsymbol{r}_k|)\, Y^*_{l m}(\boldsymbol{k}_i / k)\, Y_{l m}(\boldsymbol{s}_k) \ , \tag{3.83}$$

where $\boldsymbol{r}_j$ and $\boldsymbol{r}_k$ represent the position vectors of ions j and k, with $j \neq k$. Moreover, there are convenient formulas to transfer spherical waves about the kth site to spherical waves about the jth site[57]:

$$h_l^{(1)}(k\,|\boldsymbol{r} - \boldsymbol{r}_k|)\, Y_{l m}(\boldsymbol{s}_k) = \sum_{l' m'} G_{l m\,, l' m'}(\boldsymbol{r}_j - \boldsymbol{r}_k)\, j_{l'}(k\,|\boldsymbol{r} - \boldsymbol{r}_j|)\, Y_{l' m'}(\boldsymbol{s}_j) \ , \tag{3.84}$$

where

$$G_{l m\,, l' m'}(\boldsymbol{r}_j - \boldsymbol{r}_k) = \sum_{l'' m''} 4\pi i^{l - l' - l''} (-1)^{m' + m''} h_{l''}^{(1)}(k\,|\boldsymbol{r}_j - \boldsymbol{r}_k|)\, Y_{l'' -m''}(\boldsymbol{s}_{jk})\, B^l(l'' m'', l' -m') \tag{3.85}$$

and

$$\boldsymbol{s}_{j k} = \frac{\boldsymbol{r}_j - \boldsymbol{r}_k}{|\boldsymbol{r}_j - \boldsymbol{r}_k|} \ ; \tag{3.86}$$

$B^l(l''m'', l'\text{-}m')$ represents the integral of the product of three spherical harmonics, i.e.

$$B^{\,l}(l'' m'',\ l' \text{-} m') = \int Y_{l m}(\Omega)\, Y_{l'' m''}(\Omega)\, Y_{l'\ -m'}(\Omega)\, d\Omega \ . \tag{3.87}$$

Therefore, substituting eq. (3.84) into expression (3.83) and comparing with eq. (3.81) one finds

$$A_{l\,m_j} = A^0_{l\,m_j} + \sum_{l'm'} A_{l'm'_k}\, X_{l'm',\,l\,m}(\boldsymbol{r}_j - \boldsymbol{r}_k)\ , \tag{3.88}$$

where

$$X_{l'\,m',\,l\,m}(\boldsymbol{r}_j - \boldsymbol{r}_k) = \sum_{l''m''} C^{l'}(l''m'',\ l\ m)\ \mathrm{h}^{(1)}_{l''}(k\,|\boldsymbol{r}_j - \boldsymbol{r}_k|)\ \frac{e^{2\,i\,\delta_l} - 1}{2} \tag{3.89}$$

and

$$C^{l'}(l''m'',\ l\ m) = 4\,\pi\,(-1)^{(l' - l'' - l)}\ \ (-1)^{m'' + m}\ Y_{l''\,-m''}(s_{jk})\ B^{l'}(l''m'',\ l\ -m). \tag{3.90}$$

Thus the total wave amplitudes incident on each ion of the dicluster can be obtained in the following way

$$(A_1\ ,\ A_2) = \left(A^0_1\ ,\ A^0_2\right)\begin{pmatrix} 1 & -X(\boldsymbol{R}) \\ -X(-\boldsymbol{R}) & 1 \end{pmatrix}^{-1}\ , \tag{3.91}$$

where A_1, A_2, A°_1 and A°_2 are line matrices of dimension $(l_{\max} + 1)^2$, and $X(\boldsymbol{R})$ and $X(-\boldsymbol{R})$ are square matrices of dimension $(l_{\max} + 1)^2 \times (l_{\max} + 1)^2$; $l_{\max}$ is the maximum value of l considered in expansions (3.81) and (3.82).

For large r the scattered wave of eq. (3.82) can be written as

$$\Psi^{(s)}_{\boldsymbol{k}_i}(\boldsymbol{r}) \underset{r\to\infty}{=} \frac{1}{\sqrt{V}}\, e^{-i\,\boldsymbol{k}_f \boldsymbol{r}_j}\, f_j(\boldsymbol{k}_i\ ,\ \boldsymbol{k}_f)\ \frac{e^{i k r}}{r}\ \ , \tag{3.92}$$

where

$$f_j(\boldsymbol{k}_i\ ,\ \boldsymbol{k}_f) = \frac{1}{k}\sum_{l=0}^{\infty}\sum_{m=-l}^{m=l} A_{l m_j}\ \frac{e^{2\,i\,\delta_l} - 1}{2}\ i^{-(l+1)}\ Y_{l\,m}(\boldsymbol{k}_f / k)\ , \tag{3.93}$$

$A_{lm\,j}$ being given by eq. (3.91). Consequently, the differential scattering cross section of target valence electrons is found to be

$$\frac{d\sigma}{d\Omega} = \left| f_1(\boldsymbol{k}_i\ ,\ \boldsymbol{k}_f) + e^{-i\,\boldsymbol{k}_f\,.\,\boldsymbol{R}}\ f_2(\boldsymbol{k}_i\ ,\ \boldsymbol{k}_f)\right|^2\ , \tag{3.94}$$

where $j = 1$ represents the trailing ion, and $j = 2$ the leading ion.

The differential scattering cross section of electrons having zero velocity in the laboratory frame to be emitted at 0° with respect to the beam axis calculated from eq. (3.94) is plotted in fig. 3.9, as a function of orientation of the projectiles, for Z =1, v = 1.5a.u. and R = 2.2a.u., together with the simple differential scattering cross section of eq. (3.40) which neglects

multiple scattering; in these calculations the phase shifts of the velocity dependent Yukawa potential of eq. (3.48) have been computed numerically, and in the expansion of eq. (3.93) for the scattering amplitude l_{max} has been taken to be 7.

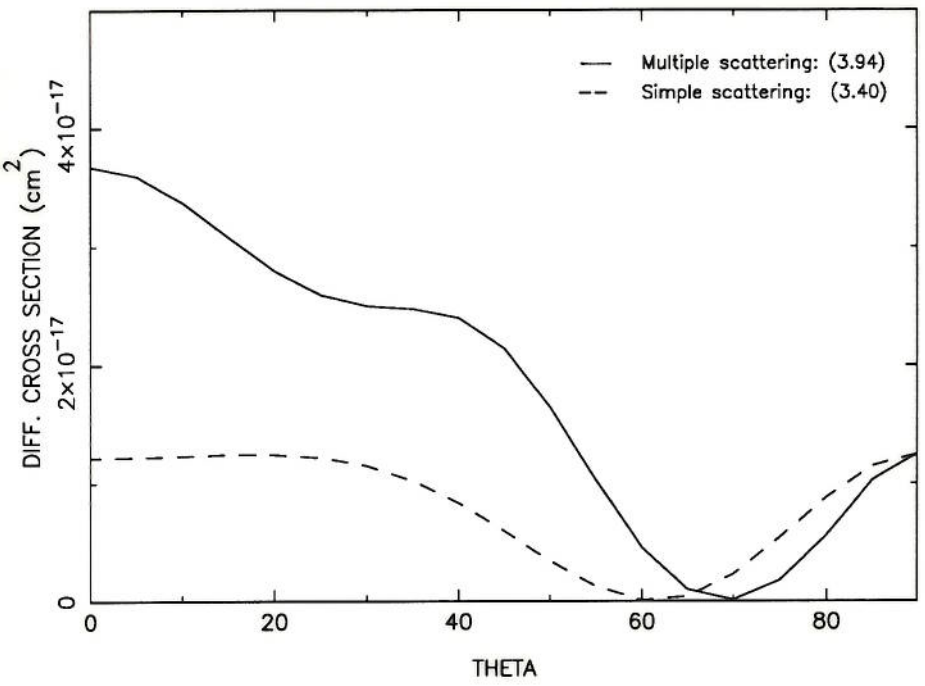


Fig. 3.9. Differential scattering cross section of electrons having zero velocity in the laboratory system to be emitted at 0° with respect to the beam axis ($k_i = -v$ and $k_f = v$) calculated from eq. (3.94) (solid curve), versus angle θ, for $Z = 1$, $v = 1.5$a.u., $R = 2.2$a.u. and $l_{max} = 7$. For comparison, the simple differential scattering cross section of eq. (3.40) is also given (dashed curve).

The results presented in fig. 3.9 are consistent with the results obtained in the second Born approximation outlined in the preceding section: in addition to the oscillations also appearing when multiple scattering is neglected, as a result of multiple scattering effects the intensity of scattered electrons is enhanced for the longitudinal orientation of the bombarding diclusters. However, the results presented here are preliminary ones, since for the charges and velocities of interest it is necessary to take greater values of the angular momentum in the expansion (3.93), thus turning the numerical approach into a very long and tedious calculation; on the other hand, the scattered wave function can be expressed as eq. (3.82) only for positions out of the range of the potential, so that this approximation cannot be made unless

$$\frac{v}{\omega_p} < R \ , \tag{3.95}$$

where ω_p is the plasmon frequency of eq. (3.6).

Hence, this approximation may be a useful method of calculating the multiple scattering for intermediate velocities ($v < 2.5$a.u.); in future work we shall investigate the nonlinearity appearing for high values of Z, considering larger values of the angular momentum, and we shall calculate the differential cross section integrated over all allowed initial states. For higher values of the velocity, second or even third order perturbation theory may be applied.

Measurements of the knock-on electron yield emitted upon bombardment of swift diclusters seem to be very sensitive to multiple scattering effects and to the mean charge state of the bombarding ions, so that new experiments performed for different charges and velocities would be very useful in order to investigate the applicability of linear theories and capture and loss theories, and also to study the effect of electron density fluctuations.

Appendix: Second order scattering amplitude for the potential (3.48) of a point charge Z

Substituting the potential (3.48) into eq. (3.46), one finds eq. (3.50) with the second Born scattering amplitude of electrons in the potential created by a single ion given by

$$f^{0}_{B_2} = \frac{2Z}{\Delta^2 + \alpha^2} + \frac{2Z^2}{\pi^2} I_{1,1}(\alpha\,,\,\alpha\,;\,\boldsymbol{k}_i\,,\,\boldsymbol{k}_f\,;\,k)\,, \tag{A3.1}$$

where $I_{1,1}$ are Dalitz integrals[58,59] of the type

$$I_{1,1}(\alpha\,,\,\alpha\,;\,\boldsymbol{k}_i\,,\,\boldsymbol{k}_f\,;\,k) = \int \frac{d\boldsymbol{q}}{q^2 - k^2 - i0^+} \frac{1}{\left(\alpha^2 + |\boldsymbol{q} - \boldsymbol{k}_i|^2\right)\left(\alpha^2 + |\boldsymbol{q} - \boldsymbol{k}_f|^2\right)}\,. \tag{A3.2}$$

This expression can be rewritten as

$$I_{1,1}(\alpha\,,\,\alpha\,;\,\boldsymbol{k}_i\,,\,\boldsymbol{k}_f\,;\,k) = \pi^2 \int_0^1 \frac{dt}{\gamma\,(\alpha^2 - 2\,i\,k\,\gamma)}\,, \tag{A3.3}$$

where

$$\gamma = \left[\alpha^2 + t\,(1-t)\,|\boldsymbol{k}_i - \boldsymbol{k}_f|^2\right]^{1/2}\,. \tag{A3.4}$$

Thus changing the integration variable in the integral of eq. (A3.3) leads

$$I_{1,1}(\alpha\,,\,\alpha\,;\,\boldsymbol{k}_i\,,\,\boldsymbol{k}_f\,;\,k) = \pi^2 \int_{\alpha}^{\sqrt{\alpha^2 + k^2 \sin^2(\theta/2)}} \frac{d\gamma}{\sqrt{\alpha^2 + k^2 \sin^2(\theta/2) - \gamma^2}\; k \sin(\theta/2)\,(\alpha^2 - 2\,i\,k\,\gamma)}\,, \tag{A3.5}$$

where θ is the angle between $\boldsymbol{k}_i$ and $\boldsymbol{k}_f$.

Finally, doing the integral of eq. (A3.5)[60] leads to eq. (3.51), once the quantities Δ and Γ are defined by eqs. (3.37) and (3.52), respectively.

References

1. N. Bohr, *The penetration of atomic particles through matter,* Dans. Vidensk. Selsk. Mat.-fys. Medd., **18** no.8 (1948).
2. J. Neufeld & R.H. Ritchie, *Passage of charged particles through plasma*, Phys. Rev. **98** 1632 (1955).
3. J. Neufeld & R.H. Ritchie, *Density effect in ionization energy loss of charged particles through plasma,* Phys. Rev. **99** 1125 (1955).
4. R.H. Ritchie, *On the interaction of charged particles with plasma*, Ph. D. thesis, University of Tennessee, Knoxville, Tennessee (1959).
5. D. Bohm & D. Pines, *A collective description of electron interactions: I. Magnetic interactions*, Phys. Rev. **82** 625 (1951).
6. D. Pines & D. Bohm, *A collective description of electron interactions, II. Collective vs. individual particle aspects of the interactions,* Phys. Rev. **85** 338 (1952).
7. D. Bhom & D. Pines, *A collective description of electron interactions: III. Coulomb interactions in a degenerate electron gas*, Phys. Rev. **92** 609 (1953).
8. D. Pines, *A collective description of electron interactions: IV. Electron interaction in metals*, Phys. Rev. **92** 626 (1953). See also D. Pines, *Elementary excitations in solids* (W.A. Benjamin Inc., New York, Amsterdam, 1963).
9. J. Lindhard, *On the propierties of a gas of charged particles*, Dans. Vidensk. Selsk. Mat.-fys. Medd. **28** no. 8 (1954).
10. See, e.g., D. Pines and P. Nozièrs, *Theory of quantum liquids* (Benjamin, New York, 1966).
11. V.N. Neelavathi, R.H. Ritchie & W. Brandt, *Bound electron states in the wake of swift ions in solids*, Phys. Rev. Lett. **33** 302 (1974); **33** 670E (1974); **34** 560E (1975).
12. M.H. Day, *Effect of dispersion on wake-bound electron states in metals*, Phys. Rev.B **12** 514 (1975).
13. V. N. Neelavathi & R.K. Kher, *Bound-electron state in the wake of a swift ion in solids*, Phys. Rev. B **14** 4229 (1976).

14. Z. Vager & D.S. Gemmell, *Polarization induced in a solid by the passage of fast charged particles*, Phys. Rev. Lett. **37** 1352 (1976).

15. R.H. Ritchie, W. Brandt & P.M. Echenique, *Wake potential of swift ions in solids*, Phys. Rev. B **14** 4808 (1976).

16. D.H. Jakubassa, *Dynamic screening of ions passing through solids*, J. Phys. C **10** 4491 (1977).

17. M. Day & M. Ebel, *Wake-bound states: Dispersive & surface effects*, Phys. Rev. B **19**, 3434 (1979).

18. P.M. Echenique, R.H. Ritchie & W. Brandt, *Spatial excitation patterns induced by swift ions in condensed matter*, Phys. Rev. B **20**, 2567 (1979).

19. J. Tejada, P.M. Echenique, O.H. Crawford & R.H. Ritchie, *Wake shifts in electron states on swift ions passing through solids*, Nucl. Instr. and Meth. **170**, 249 (1980).

20. P.M. Echenique & R.H. Ritchie, *Wake-binding energies in the random-phase approximation*, Phys. Rev. B **21** 5854 (1980).

21. F. Guinea, F. Flores & P.M. Echenique, *Charge states for protons moving in an electron gas*, Phys. Rev. Lett. **47** 604 (1981); F. Guinea, F. Flores & P.M. Echenique, *Charge states for H and He moving in an electron gas*, Phys. Rev. B **25** 6109 (1982).

22. R.H. Ritchie & P.M. Echenique, *The wake of charged particles in condensed matter*, Philos. Mag. **45** 347 (1982).

23. A. Mazarro, P.M. Echenique & R.H. Ritchie, *Charged-particle wake in the random-phase approximation*, Phys. Rev. B **27** 4117 (1983).

24. W. Brandt, A. Ratowski & R.H. Ritchie, *Energy loss of swift proton clusters in solids*, Phys. Rev. Lett. **33** 1325 (1974); E **25** 130 (1975).

25. D.S. Gemmell, J. Remilleux, J. C. Poizat, M. J. Gaillard, R.E. Holland & Z. Vager, *Evidence for an aligment effect in the motion of swift ion clusters through solids*, Phy. Rev. Lett. **34** 1420 (1975).

26. S. Datz, C. D. Moak, O.H. Crawford, M.F. Krouse, P. F. Dittner, J. Gómez del Campo, J.A. Biggerstaff, P.F. Miller, P. Huelpund & H. Knudsen, *Resonant coherent excitation of channeled ions*, Phys. Rev. Lett. **40** 843 (1978).

27. F. Bell, H.D. Betz, H. Pank & W. Stehling, *Evidence for dynamical screening of projectile ions passing through solids*, J. Phys. B **9** L443 (1976).

28. Y. Yamazaki, *Wakes, Dynamic screening*, Proc. NATO Meeting: Interaction of charged particles with solids and surfaces, Alacant (Spain), May 7-18 (1990).

29. J.M. Pitarke, P.M. Echenique & R.H. Ritchie, *Electron density fluctuactions induced by ion clusters in condensed matter*, Nucl. Instrum. Methods B **40/41** 333 (1989).

30. J.M. Pitarke, P.M. Echenique & R.H. Ritchie, *Dependence of knock-on collision electron emission on the orientation of swift diclusters in solids*, to be published.

31. J.M. Pitarke & P.M. Echenique, *Multiple scattering effects on electron emission by swift diclusters in solids*, to be published.

32. B.I. Lundqvist, *Single-particle spectrum of degenerate electron gas: II. Numerical results for electrons coupled to atoms, **6*** 206 (1967). See also L. Hedin & S. Lundquist, *Effects of electron-electron and electron-phonon interactions on the one-electron states of solids*, Solid State Physics, Vol. 23 (H. Ehrenreich & D. Turbull eds., Academic Press, New York, 1969), p. 1.

33. J.C. Inkson, *Many body theory of solids: An introduction* (Plenium Press, New York, London, 1984), p. 81, chapter 9.

34. P.M. Echenique, F. Flores & R.H. Ritchie, *Dynamic screening of ions in condensed matter*, Solid State Physics, Vol 43 (H. Ehrenreich & D. Turbull, eds., Academic Press, New York, 1969), p. 229.

35. P.M. Echenique, *Aspectos de estela en la interacción de partículas cargadas con medios materiales*, Ph.D. thesis, Universidad Autónoma de Barcelona, 1977.

36. P.M. Echenique & R.H. Ritchie, *Ioi lasterren wake-potentziala egoera solidoan*, Elhuyar **7** 1 (1979).

37. A.W. Overhauser, *Simplified theory of electron correlations in metals*, Phys. Rev. B **3** 1888 (1971).

38. L.D. Landau & E. M. Lifshitz, *Course of Theoretical Physics. Volume 3: Quantum mechanics (non relativistic theory)* (3rd. ed, Oxford, England: Pergamon Press, 1977), p. 113.

39. M. Abramowitz & I.A. Stegun, *Handbook of mathematical functions*, Dover, New York (1965).

40. M.C. Li, *Scattering by a nonspherical potential*, J.Math. Phys. **12** 936 (1971).

41. M.C. Li, *Scattering by two charged centers*, J.Math. Phys. **13** 1381 (1972)

42. D.I. Abramov & L.V. Komarov, *Method of phase shifts for scattering by potentials admitting separation of variables in spheroidal coordinates*, Theor. Mat. Fiz. **13** 209 (1972).

43. M.C. Li, *Scattering by a spin-dependent spheroidal potential* **14** 1358 (1973).

44. M.C. Li, *Spheroidal analysis of Coulomb scattering*, J.Math. Phys. **15** 570 (1974).

45. L.I. Ponomarev & L.N. Somov, T*he wave functions of continuum for the two-center problem in Quantum Mechanics*, Journal of Comp. Phys. **20** 183 (1976).

46. N.F. Mott & H.S.W. Massey, *The theory of atomic collisions* (Oxford University Press).

47. C.J. Joachain, *Quantum Collision Theory* (North-Holland Publishing Company, Amsterdam, 1975), p. 68.

48. B.A. Lippman & J. Schwinger, *Variational principles for scattering processes*, Phys. Rev. **79** 469 (1950).

49. L.I. Shiff, *Quantum Mechanics* (Mc Graw-Hill, New York, 1955), chapter 8.

50. See 47, p. 177.

51. H. Betz, *Charge states and charge-changing cross sections of fast heavy ions penetrating through gaseosus and solid media*, Rev. Mod. Phys. **44** 465 (1972).

52. R. Shakeshaft & L. Spruch, *Mechanisms for charge transfer (or for the capture of any light particle) at asymptotically high impact velocities*, Rev. Mod. Phys. **51** 369 (1979).

53. Y. Ohtsuki, *Charged beams interaction with solids* (Taylor & Francis Ltd, London, New York, 1983), chapter 6.

54. J.B. Pendry, *Theory of averaged low energy electron diffraction*, J. Phys. C **5** 2567 (1972).

55. J.B. Pendry, *Low Energy Electron Diffraction* (Academic Press, London, 1974).

56. M. A. Van Hove & S.Y. Tong, *Surface crystallography by LEED* (Springer-Verlag,

Berlin Heidelberg New York, 1979).

57. See 55, p. 272.

58. P.M. Morse & H. Fesbach, *Methods of Theoretical Physics* (McGrawHill, New York, 1953), chapter 9.

59. See 47, p. 678.

60. I.S. Gradshtein & J.M. Ryzhik, *Table of integrals, series and products* (Academic Press, London, 1965).

4. RADIATIVE ELECTRON CAPTURE BY CHANNELED IONS IN SOLIDS

4.1.Introduction

It is well known that when ions pass through matter their charge state is modified by the exchange of electrons with the target[1,2]. Different mechanisms contribute significantly to the electron capture of swift ions: mechanical electron capture processes (MEC)[3] and radiative electron capture (REC)[4]. In the first mechanism bound electrons of the target are captured by the moving ion, not radiating at all. In the REC process target valence electrons can also be captured accompanied by the emission of a photon, thus allowing conservation of energy and momentum.

Radiative capture occurs with relatively small probabilities, so that the importance of radiative electron capture as a mechanism for charge transfer has been overlooked for years. In 1972 Schnopper et al[5] first measured the X-ray spectra produced by highly stripped sulphur, chlorine and bromine ions in collisions with various targets; since then, this radiative electron capture process has been the subject of much theoretical and experimental effort[6,12], since it can become a significant tool in the study of momentum distributions of target electrons.

On the other hand, the REC process contributes only in a very small way to the total production of radiation when swift ions cross matter, so that interpretation of REC experiments can be a difficult task. However, REC processes become more important and amenable to interpretation when the bombarding ions are channeled through the solid, as pointed out by Appleton et al[10-12].

In 1963 Robinson and Oen[13], performing computer simulations of the penetration of ions in solids, found that ions incident in a monocrystalline material with initial velocities lying close to a principal axis direction are localized within a channel, in such a way that close-encounter processes are sharply reduced and abnormally large penetration occurs; this effect is called channelling[14]. Hence, when the bombarding ions are channeled the yield of characteristic X-rays is very much smaller than that observed when the beam is incident on the crystal in a random direction, since in channelling conditions ions never approach closer that 0.1 or 0.2Å to target atoms. Furthermore, it has been shown that channeled ions in thin foils have frozen charge states, and although non-radiative electron capture is the dominant

mechanism for charge transfer, the inhibition of close collisions makes the radiative process relatively more important[15-17].

The purpose of this chapter is to extend previous theoretical approaches[4,12] for the REC process of channeled ions and to study the impact parameter dependence of the process as well as the effect of capture from inner shells of the solid, including the effect of the ion´s wake and using a statistical local density approach. An interpretation of recent experimental data which suggest that REC photon energies may be less than those expected from simple considerations of transitions from the valence band of the solid to hydrogenic states of the moving ion is also presented[18,19].

In this chapter swift, stripped sulphur ions channeling through a silicon target are considered, in order to make numerical comparisons of our calculated REC peak energy positions, widths and cross sections of the emitted radiation with the experimental data of Vane et al[16].

4.2. REC probabilities

Let us consider a solid through which a swift, stripped ion of charge Z_1 and velocity $\boldsymbol{v}$ passes with impact parameter $\boldsymbol{b}$ (see fig. 4.1), and assume that it captures an electron accompanied by the emission of a single photon.

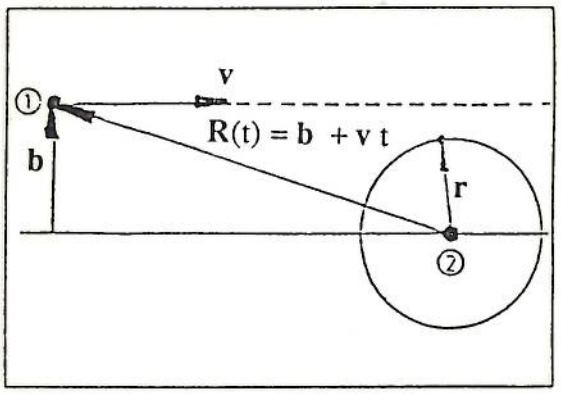


Fig. 4.1. An ion 1 moving in a straight line is incident on an atom 2 in the target, with impact parameter $\boldsymbol{b}$ (from ref. 4).

If the approximate initial and final wave functions describing the system are not orthogonal, the cross section for the system to undergo any radiative transition is not Galilean invariant in the nonrelativistic limit, and the correct result is only obtained in the frame where the centre of mass of the system is at rest[20]. Hence, treating the ion as infinitely massive and proceeding nonrelativistically, we work in the projectile frame.

Treating the electromagnetic field as a small perturbation and using first-order perturbation theory, the probability amplitude for the transition in which an electron is captured together with the emission of a photon can be written as

$$a_{if}^{(1)} = \frac{1}{\mathrm{i}} \int \mathrm{d}t \, \langle f | H' | i \rangle \, \mathrm{e}^{\mathrm{i}\,\omega t} \,, \tag{4.1}$$

where $|i\rangle$ and $|f\rangle$ represent the initial and final state of the system, respectively, and

$$\omega = E + E_f - E_i - \frac{1}{2} v^2 \,, \tag{4.2}$$

E_i and E_f being the initial and final stationary state energies of the captured electron, referred to

the target and to the ion, respectively, and $E = ck$ the energy of the emitted photon; $\boldsymbol{k}$ is the momentum of the emitted photon and c is the velocity of light. The Hamiltonian of the interaction between the electron and the free radiation field is[21],

$$H' = \frac{\mathrm{i}}{c} \boldsymbol{A} \cdot \boldsymbol{\nabla} \ , \tag{4.3}$$

where $\boldsymbol{A}$ is the vector potential of the electromagnetic field[22]

$$\boldsymbol{A}(\boldsymbol{r}, t) = \frac{1}{\mathrm{i}} \sum_{\boldsymbol{k}, \lambda} \left(\frac{2\pi c^2}{EV} \right)^{1/2} \boldsymbol{\lambda}_{\boldsymbol{k}} \, \mathrm{e}^{\mathrm{i}\, \boldsymbol{k} \cdot \boldsymbol{r}} \, (b^{+}_{-\boldsymbol{k}\,\lambda} - b_{\boldsymbol{k}\,\lambda}) \ , \tag{4.4}$$

and $\boldsymbol{\lambda}_{\boldsymbol{k}}$ is the polarization vector of a photon with wave vector $\boldsymbol{k}$ and polarization index λ, which in free space is perpendicular to the direction of propagation. V is the normalization volume of the electromagnetic field, and $b^{+}_{\boldsymbol{k}\,\lambda}$ and $b_{\boldsymbol{k}\,\lambda}$ are the creation and anhilation operators, respectively, of a photon with momentum $\boldsymbol{k}$ and polarization vector $\boldsymbol{\lambda}_{\boldsymbol{k}}$.

Substituting the vector potential (4.4) into eq. (4.3), one finds for the matrix element of the matter-radiation interaction

$$< f \mid H' \mid i > = \left(\frac{2\pi}{EV} \right)^{1/2} < \varphi_f(\boldsymbol{r}) \mid \mathrm{e}^{-\mathrm{i}\, \boldsymbol{k} \cdot \boldsymbol{r}} \, \boldsymbol{\lambda}_{\boldsymbol{k}} \cdot \boldsymbol{\nabla} \mid \varphi_i(\boldsymbol{r} + \boldsymbol{b} + \boldsymbol{v}\, t) \, \mathrm{e}^{-\mathrm{i}\, \boldsymbol{v} \cdot \boldsymbol{r}} > , \tag{4.5}$$

with respect to the ion frame, where $\varphi_i(\boldsymbol{r})$ and $\varphi_f(\boldsymbol{r})$ represent the initial and final stationary wave functions of the captured electron, referred to the target and to the ion, respectively. After a Fourier transformation of these wave functions to the momentum representation, one finds

$$< f \mid H' \mid i > = \mathrm{i} \left(\frac{2\pi}{EV} \right)^{1/2} \int \mathrm{d}\boldsymbol{q} \, \boldsymbol{\lambda}_{\boldsymbol{k}} \cdot (\boldsymbol{q} - \boldsymbol{v}) \, \widetilde{\varphi}^{*}_{f}(\boldsymbol{q} - \boldsymbol{v} - \boldsymbol{k}) \, \widetilde{\varphi}_i(\boldsymbol{q}) \, \mathrm{e}^{\mathrm{i}\, \boldsymbol{q} \cdot (\boldsymbol{b} + \boldsymbol{v}\, t)} , \tag{4.6}$$

where

$$\widetilde{\varphi}_{i,f}(\boldsymbol{q}) = (2\pi)^{-3/2} \int \mathrm{d}\boldsymbol{r} \, \mathrm{e}^{-\mathrm{i}\, \boldsymbol{q} \cdot \boldsymbol{r}} \, \varphi_{i,f}(\boldsymbol{r}) \ . \tag{4.7}$$

Thus substituting the matrix element (4.6) into eq. (4.1) leads

$$a^{(1)}_{if} = \frac{(2\pi)^{3/2}}{(EV)^{1/2}} \int \mathrm{d}\boldsymbol{q} \, \delta(\omega + \boldsymbol{q} \cdot \boldsymbol{v}) \, \boldsymbol{\lambda}_{\boldsymbol{k}} \cdot (\boldsymbol{q} - \mathrm{v}) \, \mathrm{e}^{\mathrm{i}\, \boldsymbol{q} \cdot \boldsymbol{b}} \, \widetilde{\varphi}^{*}_{f}(\boldsymbol{q} - \mathrm{v} - \boldsymbol{k}) \, \widetilde{\varphi}_i(\boldsymbol{q}) \ . \tag{4.8}$$

Consequently, the probability per unit energy and unit solid angle for capturing a target electron from the initial state represented by $\varphi_i(\boldsymbol{r})$ into the final state represented by $\varphi_f(\boldsymbol{r})$ in a

collision at impact parameter $\boldsymbol{b}$ with emission of a photon of propagation vector $\boldsymbol{k}$ and polarization vector $\boldsymbol{\lambda}_k$ is found to be

$$\left(\frac{d^3\gamma}{dE\,d\Omega}\right)_{b,\lambda} = \frac{E^2}{c^3}|f|^2 \ , \tag{4.9}$$

where

$$f = E^{-1/2}\int dq\ \delta(\omega + q\ .\ v)\ \lambda_k\ .\ (q - v)\ e^{i\,q\,.\,b}\ \tilde{\varphi}_f^*(q - v - k)\ \varphi_i(q)\ . \tag{4.10}$$

In particular, when the initial stationary state is represented by plane or coulombic waves of the continuum with momentum $\boldsymbol{q}$, the probability per unit energy and unit solid angle for capturing a target electron together with the emission of a photon of propagation vector $\boldsymbol{k}$ and polarization vector $\boldsymbol{\lambda}_k$ can also be written in the following way

$$\left(\frac{d^3\gamma}{dE\,d\Omega}\right)_{\lambda} = \frac{E\,T}{2\,\pi\,c^3}\left|\int dr\ \varphi_f^*(r)\ e^{-i\,k\,.\,r}\ \lambda_k\ .\ \nabla\ \varphi_i'(r)\right|^2 \delta(\omega') \ , \tag{4.11}$$

where T is the interaction time, $\varphi_i'(r)$ is the initial stationary wave function of the captured electron referred to the ion position, i.e. a wave function of momentum $\boldsymbol{q}$ - $\boldsymbol{v}$, and

$$\omega' = E + E_f - E_i' \ , \tag{4.12}$$

E_i' being the initial stationary state energy of the captured electron referred to the ion position; it is worth noting that the REC probability of eq. (4.11) is independent of the impact parameter.

If we specialize to the situation in which the electron is captured to the lowest state, that is, to a K-shell orbital of the bare ion, we have[23]

$$\varphi_f(r) = \left(\alpha^3/\pi\right)^{1/2} e^{-\alpha r} \ , \tag{4.13}$$

where

$$\alpha = \left(-2\,E_f\right)^{1/2} . \tag{4.14}$$

It is of great interest here to notice that the enhancement of the mean electron density of the polarized medium induces a potential at the site of the projectile given, in the linear approximation by[24,25]

$$\lim_{r \to 0} \left[\Phi(r) - \frac{Z_1}{r} \right] = - \frac{\pi Z_1 \omega_p}{2 v} \quad , \tag{4.15}$$

where $\Phi(r)$ is the total wake potential of the projectile moving in the medium, and ω_p is the plasmon frequency

$$\omega_p = \left(3 / r_s^3 \right)^{1/2} \quad , \tag{4.16}$$

r_s being the equivalent one-electron radius of the electron gas. Consequently, the energy eigenvalue for the lowest state of the hydrogen-like moving stripped ion should be

$$E_f = - \frac{1}{2} Z_1^2 + \frac{\pi Z_1 \omega_p}{2 v} \quad . \tag{4.17}$$

4.2. Capture of an electron from a bound state in the solid

Electrons in the solid and near the centre of a channel can be represented, on very general grounds, by the orbital

$$\varphi_i(\boldsymbol{r}) = \left(\beta^3 / \pi\right)^{1/2} e^{-\beta r} , \tag{4.18}$$

where

$$\beta = \left(-2 E_i\right)^{1/2} \tag{4.19}$$

E_i being the binding energy of the electron in the lattice, which may be taken to be of a few electronvolts, and r being the distance from a lattice atom to the ion. This is a very schematic form of the wave function in the solid that will be improved lare on.

The Fourier transforms of the wave functions (4.13) and (4.18) are

$$\widetilde{\varphi}_f(\boldsymbol{q}) = (2\pi)^{3/2} \frac{(\alpha/\pi)^{5/2}}{\left(\alpha^2 + q^2\right)^2} \tag{4.20}$$

and

$$\widetilde{\varphi}_i(\boldsymbol{q}) = (2\pi)^{3/2} \frac{(\beta/\pi)^{5/2}}{\left(\beta^2 + q^2\right)^2} . \tag{4.21}$$

Hence, introducing eqs. (4.20) and (4.21) into eq. (4.10), and then substituting the amplitude (4.10) into eq. (4.9) we find

$$\left(\frac{d^3\gamma}{dE\, d\Omega}\right)_{b,\lambda} = \frac{2^6 (\alpha\beta)^5 E}{\pi^4 c^3} \left| \int d\boldsymbol{q}\, \delta(\omega + \boldsymbol{q} \cdot \boldsymbol{v}) \frac{\boldsymbol{\lambda}_k \cdot (\boldsymbol{q} - \boldsymbol{v})\, e^{i\boldsymbol{q}\cdot\boldsymbol{b}}}{\left(\alpha^2 + q'^2\right)^2 \left(\beta^2 + q^2\right)^2} \right|^2 , \tag{4.22}$$

where

$$\boldsymbol{q}' = \boldsymbol{q} - \boldsymbol{v} - \boldsymbol{k} . \tag{4.23}$$

Choosing the z-axis in the direction of $\boldsymbol{v}$, taking $\boldsymbol{q} = (\boldsymbol{Q}, q_z)$, and summing over polarization index, we find the following expression for the probability per unit energy and unit solid angle for capturing a bound electron in the solid to a K-shell orbital of the projectile together with the emission of a photon of momentum $\boldsymbol{k}$[19]:

$$\left(\frac{d^3\gamma}{dE\,d\Omega}\right)_b = \frac{2^6(\alpha\beta)^5 E}{\pi^4 c^3 v^2}\sum_\lambda \left| \int dQ \frac{\lambda_k \cdot \left(Q - v - (\omega/v^2)\,v\right) e^{iQ\cdot b}}{\left[\alpha^2 + \left(Q' - (\omega/v^2)\,v\right)^2\right]^2 \left[\beta^2 + Q^2 + \omega^2/v^2\right]^2} \right|^2 , \quad (4.24)$$

where

$$Q' = Q - v - k \ . \quad (4.25)$$

Now integrating eq. (2.24) over all impact parameters and using[26]

$$\sum_\lambda \left|\lambda_k \cdot \left(Q - v - (\omega/v^2)\,v\right)\right|^2 = \left|k \wedge \left(Q - v - (\omega/v^2)\,v\right)\right|^2 / k^2 \ , \quad (4.26)$$

we find

$$\frac{d^3\gamma}{dE\,d\Omega} = \frac{2^8(\alpha\beta)^5 E}{\pi^2 c^3 v^2} \int dQ \frac{\left|k \wedge \left(Q - v - (\omega/v^2)\,v\right)\right|^2 / k^2}{\left[\alpha^2 + \left(Q' - (\omega/v^2)\,v\right)^2\right]^4 \left[\beta^2 + Q^2 + \omega^2/v^2\right]^4} \ . \quad (4.27)$$

Dipole approximation

If the dipole approximation is made, thus neglecting k in comparison with v, eq. (4.24) can be rewritten, transferring to the laboratory frame, in the following way

$$\left(\frac{d^3\gamma}{dE\,d\Omega}\right)_b = \frac{2^6(\alpha\beta)^5 E}{\pi^4 c^3 v^2}\sum_\lambda \left| \int dQ \frac{\lambda_k \cdot (Q + Q_\alpha)\, e^{iQ\cdot b}}{\left(\alpha^2 + Q^2 + Q_\alpha^2\right)^2 \left(\beta^2 + Q^2 + Q_\beta^2\right)^2} \right|^2 , \quad (4.28)$$

where

$$Q_\alpha = \frac{1}{v^2}\left[-E_f + E_i - \frac{1}{2}v^2 - E\,(1 - v\cos\theta/c)\right] v \quad (4.29)$$

and

$$Q_\beta = \frac{1}{v^2}\left[-E_f + E_i + \frac{1}{2}v^2 - E\,(1 - v\cos\theta/c)\right] v \ . \quad (4.30)$$

In particular, for emission of a photon of wave vector k parallel with v we have

$$\left(\frac{d^3\gamma}{dE\,d\Omega}\right)_b(\theta=0)=\frac{2^8(\alpha\beta)^5E}{\pi^2c^3v^2}\left|\int_0^\infty dQ\frac{Q^2J_0(Qb)}{\left(\alpha^2+Q^2+Q_\alpha^2\right)^2\left(\beta^2+Q^2+Q_\beta^2\right)^2}\right|^2, \quad (4.31)$$

where θ is the angle between $\boldsymbol{k}$ and $\boldsymbol{v}$, and J_0 is the zero order Bessel function of the first kind[27]. Instead, for emission of radiation at $\theta >> 1$ the main contribution to the integral of eq. (4.24) comes from $Q \approx 0$, so that one may write

$$\left(\frac{d^3\gamma}{dE\,d\Omega}\right)_b(\theta>>1)\approx\frac{2^8(\alpha\beta)^5E\sin^2\theta}{\pi^2c^3}\left|\int_0^\infty dQ\frac{QJ_0(Qb)}{\left(\alpha^2+Q^2+Q_\alpha^2\right)^2\left(\beta^2+Q^2+Q_\beta^2\right)^2}\right|^2. \quad (4.32)$$

In fig. 4.2 we give the REC spectrum calculated from eq. (4.32) for 160MeV bombarding bare sulphur ions, b = 1.5Å and θ = 46.5° as in the experiment of ref. 19. In this calculation, the final stationary state energy has been corrected according to eq. (4.17) using the equivalent one-electron radius of an electron gas of valence electron density equal to the total electron density in the centre of the channel ($b \approx$ 1.5Å), i.e. $r_s \approx$ 2.15a.u. (see fig. 4.5).

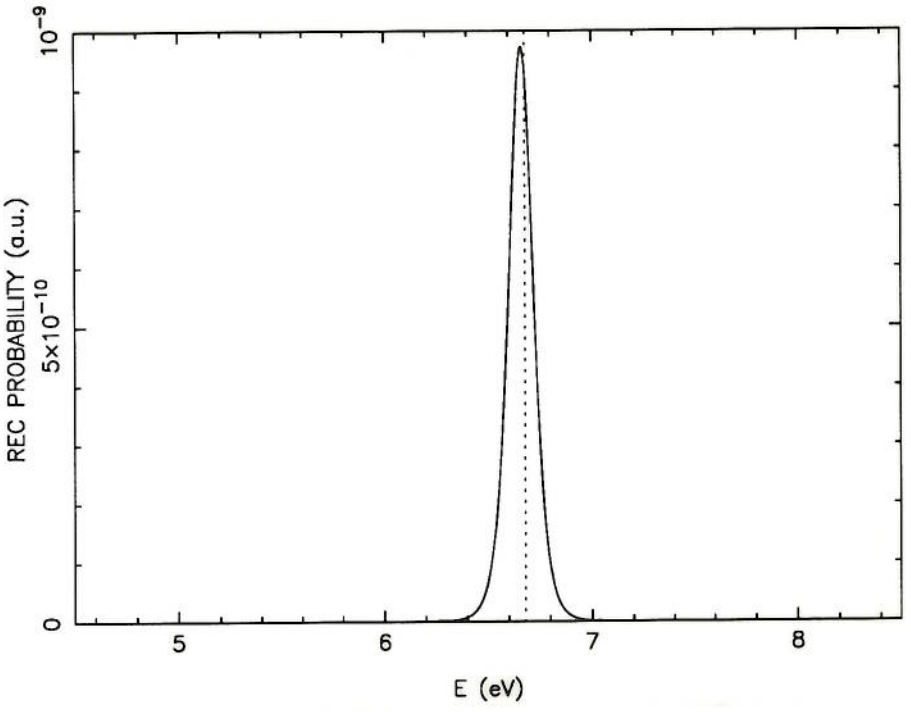


Fig. 4.2. REC probability per unit energy and unit solid angle calculated from eq. (4.32) for 160MeV bombarding bare sulphur ions, as a function of photon energy, when capture is assumed to occur of electrons at 1.5Å from the nearest atom in the solid (b = 1.5Å); the vertical dotted line refers to the REC energy of eq. (4.33). θ and r_s have been taken to be 46.5° and 2.15a.u., respectively.

If we neglect the difference between the vacuum energy and the actual energy of electrons in the target, as well as the wake correction in the binding energy of an electron to the projectile due to the polarization of the medium, the REC energy is given by

$$E_{\mathrm{REC}} = \frac{1}{2} v^2 + \frac{1}{2} Z_1^2 \ , \tag{4.33}$$

as shown in fig. 4.3. Fig. 4.2 shows that the peak energy closely approximates the REC energy of eq. (4.33), though it is slightly smaller due to the wake correction in the centre of the channel; on the other hand, non-zero REC probabilities are obtained for smaller and greater energies than the peak energy, as a consequence of the momentum distribution of target electrons.

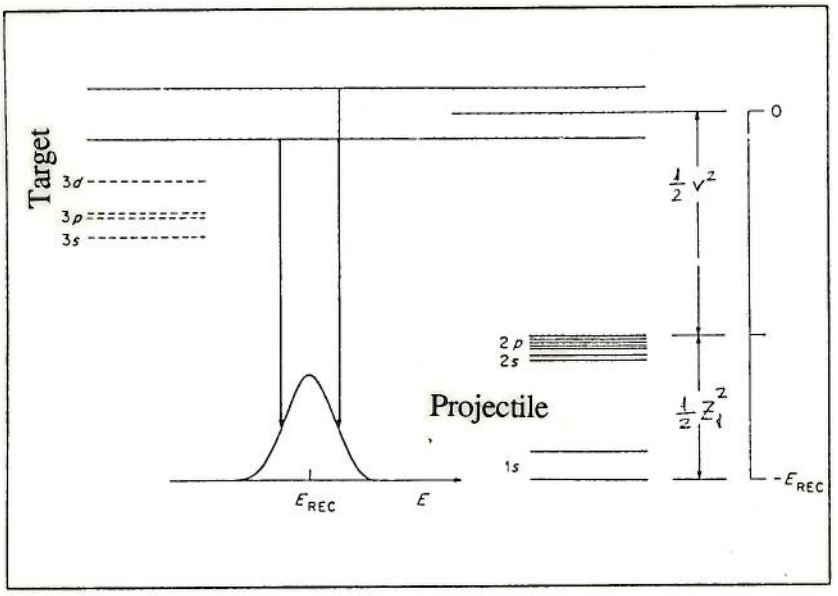


Fig. 4.3. Schematic representation of the radiative electron capture process viewed from the rest frame of the projectile ion (from ref. 12).

The full widths at half maximum of the REC spectra calculated from eq. (4.32) are plotted, as a function of impact parameter, in fig. 4.4, for the same conditions as in fig. 4.2 and several energies of the incident ions. This figure shows that the photon energy distribution broadens as the impact parameter decreases; this is consistent with the use of a local density approximation, whereby the initial momentum distribution of target electrons may be expected to be wider as the impact parameter decreases.

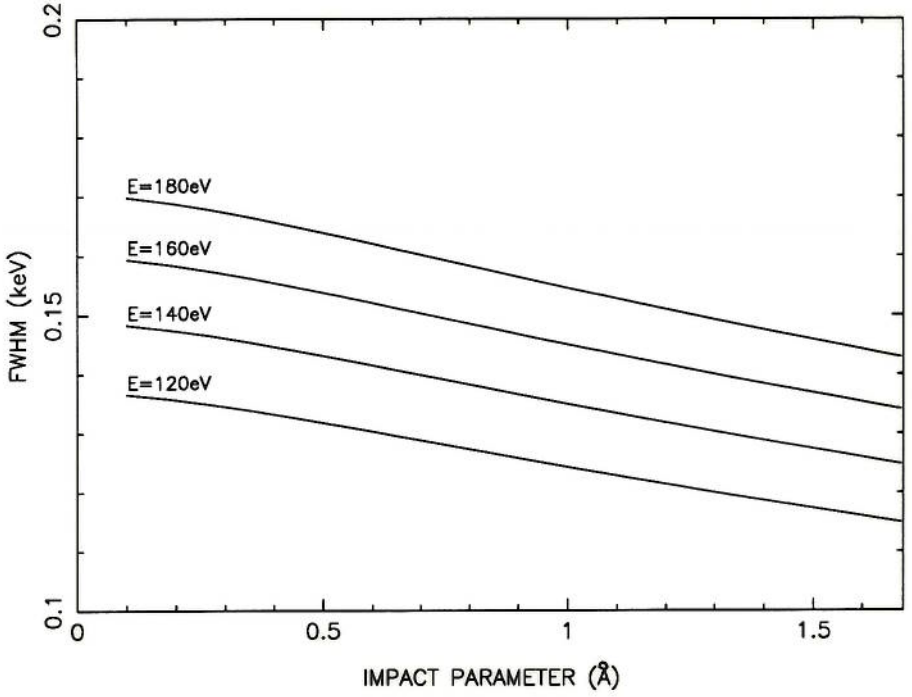


Fig. 4.4. Full widths at half maximum (FWHM) of the REC spectra calculated from eq. (4.32), as a function of impact parameter, for incident ion energies from 120 to 180MeV. θ has been taken to be 46.5°.

4.3. Capture in the local density approximation

The electron structures of crystalline solids of interest in REC experiments are intricate and tedious to calculate by numerical methods. Even if known, the representation of such structures in terms of orbitals such as in the simple example displayed in the preceding section would be difficult and time-consuming.

Here we simplify REC calculations considerably by using the local density approximation; we assume that each volume element of the solid encountered by the ion in the channelling trajectory constitutes an independent electron gas at the total local electron density there, thus defining the local parameters $r_s(\boldsymbol{r})$ and $E_F(\boldsymbol{r})$ as

$$r_s(\boldsymbol{r}) = \left[\frac{3}{4\,\pi\, n(\boldsymbol{r})}\right]^{1/3}, \tag{4.34}$$

where $n(\boldsymbol{r})$ is the total electron density at $\boldsymbol{r}$, and

$$E_F(\boldsymbol{r}) = \frac{(9\,\pi/4)^{2/3}}{2\,r_s^2(\boldsymbol{r})} \approx \frac{1.84}{r_s^2(\boldsymbol{r})}\,. \tag{4.35}$$

Then we average the local REC probability over all possible channelling trajectories of the ion.

In order to calculate the local REC probabilities in the local density approximation, first of all we assume that electrons undergoing capture can be represented by plane waves, and then we represent them by coulombic wave functions.

Plane waves

At asymptotically high incident energies it can be assumed in the local density approximation that target electrons undergoing capture are initially free, thus representing them by plane waves

$$\varphi_i(\boldsymbol{r}) = \frac{1}{\sqrt{V}}\, e^{i\,\boldsymbol{q}\cdot\boldsymbol{r}}\,, \tag{4.36}$$

where $\boldsymbol{q}$ represents the initial momentum of the target electron in the laboratory frame, with

modulus

$$q = \left[2\,(E_i + E_F)\right]^{1/2}, \tag{4.37}$$

E_i being the energy of the electron referenced to the vacuum level if the work function of the target is neglected (typical work functions are of a few electronvolts), and E_F representing the local Fermi energy of eq. (4.35).

The Fourier transform of the wave function (4.36) is

$$\varphi_i(\boldsymbol{q}') = \frac{(2\pi)^{3/2}}{\sqrt{V}}\,\delta(\boldsymbol{q}' - \boldsymbol{q}) \ . \tag{4.38}$$

Now introducing (4.20) and (4.38) into (4.10), substituting the amplitude (4.10) into eq. (4.9), and summing over polarization index and over initial states of target electrons, we find

$$\frac{\mathrm{d}^3\gamma}{\mathrm{d}E\,\mathrm{d}\Omega} = \frac{2^5\,\alpha^5\,E\,T}{c^3\,V}\sum_i \frac{|\boldsymbol{k}\wedge(\boldsymbol{q}-\boldsymbol{v})|^2/k^2}{\left[\alpha^2 + (\boldsymbol{q}-\boldsymbol{v}-\boldsymbol{k})^2\right]^4}\,\delta(\omega + \boldsymbol{q}\,.\,\boldsymbol{v}) \ , \tag{4.39}$$

where T represents the interaction time, and the argument of the Dirac delta function accounting for the conservation of energy is

$$\omega + \boldsymbol{q}\,.\,\boldsymbol{v} = E + E_f + E_F - \frac{1}{2}(\boldsymbol{q}-\boldsymbol{v})^2 . \tag{4.40}$$

Eq. (4.39) can be obtained, also, substituting the plane wave of the target electron referred to the moving ion

$$\varphi_i'(\boldsymbol{r}) = \frac{1}{\sqrt{V}}\,\mathrm{e}^{\,\mathrm{i}\,(\boldsymbol{q}-\boldsymbol{v})\,.\,\boldsymbol{r}} \tag{4.41}$$

and the final wave function (4.13) into eq. (4.11), and then summing over polarization index and over initial states of target electrons.

The local Fermi energy appearing in eq. (4.40) accounts for the fact that electrons at small r tend to be bound in the solid more strongly than those electrons at larger values of r, thus the corresponding local REC peak energies getting smaller as r decreses.

Dividing the probability per unit energy, unit solid angle and unit time for capturing a target electron together with the emission of a photon of momentum $\boldsymbol{k}$ by the velocity of the ion, one obtains the differential inverse mean free path (DIMFP) per unit energy and unit solid angle

$$\frac{d\mu}{dE\,d\Omega} = \frac{2^5\,\alpha^5\,E}{c^3\,v\,V} \sum_i \frac{|\boldsymbol{k} \wedge (\boldsymbol{q} - \boldsymbol{v})|^2 / k^2}{\left[\alpha^2 + (\boldsymbol{q} - \boldsymbol{v} - \boldsymbol{k})^2\right]^4} \delta(\omega + \boldsymbol{q} \cdot \boldsymbol{v}) \ . \tag{4.42}$$

Now transforming the sum over initial states of target electrons to an integral covering a Fermi sphere, incorporating a factor of 2 for the possible spin states, and transforming to the laboratory frame, we find, after some algebra, the following result for the DIMFP per unit energy and unit solid angle for emission of a photon with energy E at θ with respect to the incident beam[19]

$$\frac{d\mu}{dE\,d\Omega} = \frac{\alpha^5\,E}{2\pi^3\,c^3\,v^2} \int_{q_{min}}^{q_{max}} dq\,q \int_0^{2\pi} d\varphi \frac{\left[(q\,\mu - v)\sin\theta - q\,v\cos\theta\cos\varphi\right]^2 + v^2\,q^2\sin^2\varphi}{\left[E_F + E'\left(1 - \frac{q}{c}\rho + \frac{v}{c}\cos\theta + \frac{E'}{2c^2}\right)\right]^4} \ , \tag{4.43}$$

when

$$E_1 - E_f - 2\sqrt{E_1 E_F} \le E' \le E_1 - E_f + 2\sqrt{E_1 E_F} \ , \tag{4.44}$$

and zero, otherwise. In these expressions,

$$E_1 = \frac{1}{2} v^2 \ , \tag{4.45}$$

$$q_{min} = \sqrt{2\,(E_f + E_F + E')} - \sqrt{2\,E_1} \ , \tag{4.46}$$

$$q_{max} = \min\left(\sqrt{2E_F} \ , \sqrt{2(E_f + E_F + E')} + \sqrt{2E_1}\right) \ , \tag{4.47}$$

$$\mu = \frac{1}{q\,v}\left[\frac{1}{2} q^2 - (E_f + E_F + E') + E_1\right] \ , \tag{4.48}$$

$$v = (1 - \mu^2)^{1/2} \ , \tag{4.49}$$

$$\rho = \mu\cos\theta + v\sin\theta\cos\varphi \tag{4.50}$$

and

$$E' = E\,(1 - v\,\cos\theta / c) \ . \tag{4.51}$$

If the dipole approximation is made, thus neglecting $\boldsymbol{k}$ in comparison with $\boldsymbol{q}$ and $\boldsymbol{v}$, one obtains

$$\frac{d\mu}{dE\,d\Omega} = \frac{\alpha^5\,E}{4\pi^2\,c^3} \frac{C_1\,(E_{max} - E_{min}) + C_2\,(E_{max}^2 - E_{min}^2) + C_3\,(E_{max}^3 - E_{min}^3)}{E_1\,(E_F + E')^4} \ , \tag{4.52}$$

where

$$C_1 = \frac{(E_f + E_F + E' - E_1)^2}{2E_1}(\sin^2\theta - 2\cos^2\theta) + 4\,(E_f + E_F + E')\,\sin^2\theta \ , \tag{4.53}$$

$$C_2 = -\frac{E_f + E_F + E' + E_1}{2E_1}(\sin^2\theta - 2\cos^2\theta) \ , \tag{4.54}$$

$$C_3 = \frac{1}{6E_1}(\sin^2\theta - 2\cos^2\theta) \ , \tag{4.55}$$

$$E_{min} = \frac{1}{2}q_{min}^2 \tag{4.56}$$

and

$$E_{max} = \frac{1}{2}q_{max}^2 \ . \tag{4.57}$$

Integrating eq. (4.43) over all directions of photon emission, one finds the DIMFP per unit energy for emission of a photon with energy E as

$$\frac{d\mu}{dE} = \frac{2^4\,\alpha^5\,E}{3\,\pi\,c^3\,v^2}\,\frac{(E_f + E_F + E)\,(E_{max} - E_{min})}{(E_F + E)^4} \ . \tag{4.58}$$

In particular, setting the Fermi energy equal to zero, thus the only contribution to the sum in eq. (4.42) coming from $q = 0$, and integrating over all directions and energies of photon emission, we find the well known total cross section for radiative recombination

$$\sigma = \frac{2^6}{3}\frac{1}{c^2}\frac{2\pi}{c}\frac{(-v_f)^{5/2}\,(v + v_f)^{1/2}}{v^3} \ , \tag{4.59}$$

where v_f and v represent the frequency of the captured electron and the emitted radiation, respectively, $1/c^2$ is the classical electron radius, and $2\pi/c$ is the Compton wave length of the electron.

Coulombic waves

Now we assume in the local density approximation that each electron undergoing capture from the solid experiences the full Coulomb field of the projectile, so that target electrons are in

a continuum hydrogenic state of the bare bombarding ion. The wave function representing a continuum hydrogenic state can be expanded in partial waves [28] (see Appendix) as

$$\varphi_i(r) = \frac{1}{\sqrt{V}} \frac{1}{q\,r} \sum_{l=0}^{\infty} (2l+1)\, \mathrm{i}^{l}\, \mathrm{e}^{\mathrm{i}\delta_l} F_l(q\,, r)\, P_l(\cos\theta) \quad , \tag{4.60}$$

or, with respect to the moving ion,

$$\varphi_i(r) = \frac{1}{\sqrt{V}} \frac{1}{q'\,r} \sum_{l=0}^{\infty} (2l+1)\, \mathrm{i}^{l}\, \mathrm{e}^{\mathrm{i}\delta_l} F_l(q', r)\, P_l(\cos\theta'), \tag{4.61}$$

where the quantities δ_l are the Coulomb phase shifts, F_l are the regular spherical Coulomb functions, P_l are the Legendre polynomials, θ and θ' represent the angles between $\boldsymbol{q}$ and $\boldsymbol{r}$ and $\boldsymbol{q}'$ and $\boldsymbol{r}$, respectively, and

$$\boldsymbol{q}' = \boldsymbol{q} - \boldsymbol{v} \quad . \tag{4.62}$$

If the dipole approximation is made, we can make use of the fact that in this approximation only those continuum eigenfunctions with $l = 1$ contribute, and then summing over polarization index and over initial states of target electrons, we find the following result for the probability per unit energy and unit solid angle of a target electron to be captured together with the emission of a photon with momentum $\boldsymbol{k}$ (see Appendix)

$$\frac{\mathrm{d}^3\gamma}{\mathrm{d}E\,\mathrm{d}\Omega} = \frac{2^6\,\pi\,\alpha^6\,E\,T}{c^3\,V} \sum_i \frac{|\boldsymbol{k} \wedge (\boldsymbol{q} - \boldsymbol{v})|^2 f\left(\sqrt{-E_{\mathrm{f}}/(E_{\mathrm{f}} + E_{\mathrm{F}} + E)}\right)/k^2}{(\boldsymbol{q} - \boldsymbol{v})^3 \left[\alpha^2 + (\boldsymbol{q} - \boldsymbol{v})^2\right]^3}\, \delta(\omega'), \tag{4.63}$$

where ω' is given by eq. (4.12), and

$$f(x) = \frac{\mathrm{e}^{-4x\tan^{-1}(1/x)}}{1 - \mathrm{e}^{-2\pi x}} \quad . \tag{4.64}$$

Now transforming the sum over initial states to an integral covering a Fermi sphere of target electrons, incorporating a factor of 2 for the possible spin states, and transforming to the laboratory frame, one may write the DIMFP per unit energy and unit solid angle for emission of a photon of energy E at θ with respect to the beam direction as[19]

$$\frac{\mathrm{d}\mu}{\mathrm{d}E\,\mathrm{d}\Omega} = \frac{\alpha^6\,E}{2^{3/2}\,\pi\,c^3} \frac{C_1(E_{\max} - E_{\min}) + C_2(E_{\max}^2 - E_{\min}^2) + C_3(E_{\max}^3 - E_{\min}^3)}{E_1(E_f + E_{\mathrm{F}} + E')^{3/2}(E_{\mathrm{F}} + E')^3} f\left(\sqrt{-E_f/(E_f + E_{\mathrm{F}} + E')}\right), \tag{4.65}$$

where C_1, C_2, C_3, $E_{\min}$ and $E_{\max}$ are given by eqs. (4.53), (4.54), (4.55), (4.56) and (4.57),

respectively, and $E'$is the energy of the emitted radiation referred to the ion frame, which is given by eq. (4.51).

Integrating eq. (4.65) over all directions of the emitted radiation, we find

$$\frac{d\mu}{dE}=\frac{2^{7/2}\,\alpha^6\,E}{3\,c^3}\,\frac{(E_{max}-E_{min})\,f\left(\sqrt{-E_f/(E_f+E_F+E)}\right)}{E_1\,(E_f+E_F+E)^{1/2}\,(E_F+E)^3}\,. \tag{4.66}$$

In particular, setting the Fermi energy equal to zero, thus the only contribution to the sum in eq. (4.42) coming from $q = 0$, and integrating over all directions and energies of the emitted radiation yields the Bethe-Salpeter cross section for radiative recombination[29,30]

$$\sigma=\frac{2^7\,\pi}{3}\,\frac{1}{c^2}\,\frac{2\,\pi}{c}\,\frac{(-\nu_f)^3}{(\nu+\nu_f)\,\nu^2}\,f\left(\sqrt{-\nu_f/(\nu+\nu_f)}\right)\,, \tag{4.67}$$

where ν_f and ν represent the frequency of the captured electron and the emitted radiation, respectively.

Statistical model for REC from channeled ions

With the aim of interpreting the available experimental data, we are interested in the dependence of REC probabilities on photon energy for a given direction of emission. Therefore, we consider expressions (4.43), (4.52) or (4.65) to calculate the local DIMFP per unit energy and unit solid angle for capturing an electron in a given part of the solid together with the emission of radiation, and then we employ a statistical approximation.

Assuming that capture from an infinitesimal volume element of the solid can be calculated by atributing the local Fermy energy of eq. (4.35) to electrons in that volume element and that channeled ions sample on straight-line trajectories all portions of the Wigner-Seitz sphere corresponding to impact parameters greater than a given b_{min}, we compute the statistical average as[12,18,19]

$$\left\langle\frac{d\mu}{dE\,d\Omega}\right\rangle=\frac{3}{r_{ws}^3}\int_{b_{min}}^{r_{ws}}dr\,r\,(r-b_{min})\,\frac{d\mu}{dE\,d\Omega}\left[E_F(r)\right]\,, \tag{4.68}$$

where r_{ws} is the Wigner-Seitz radius; the local DIMFP per unit energy and unit solid angle appearing in this expression is given by eqs. (4.43), (4.52) or (4.65), depending on weather the dipole approximation is made and on weather plane waves or coulombic waves of target electrons are used. The total density of electrons at $\boldsymbol{r}$ in the channel is computed from a relativistic Hartree-Fock program using the Wigner-Seitz boundary condition[31], thus obtaining the local parameters $r_s(\boldsymbol{r})$ and $E_F(\boldsymbol{r})$ from eqs. (4.34) and (4.35), respectively. Fig. 4.5 shows a plot against r of the local equivalent one-electron radius computed from this program for silicon.

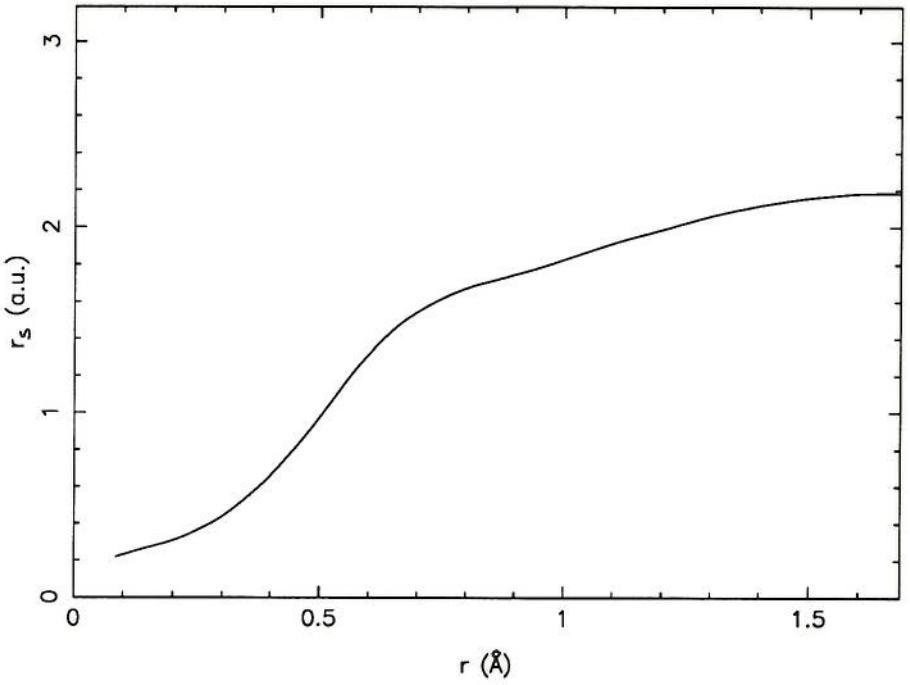


Fig. 4.5. The equivalent one-electron radius $r_s(r)$ plotted versus position in the Wigner-Seitz cell for silicon.

In the following sections 100-200MeV S^{16+} ions channeling through a silicon target are considered, and REC spectra, peak energy positions, full widths at half maximum and differential cross sections are calculated in this statistical model, when photons emitted at 46.5° with respect to the beam direction are considered. Comparisons of our results with the experimental data of Vane et al[16] are also presented.

REC peak energies: energy deficit

First of all we give in fig. 4.6 the local REC spectra calculated from eqs. (4.43), (4.52) and (4.65) for 160MeV bombarding bare sulphur ions, using the local electron density of fig. 4.5 corresponding to capture of electrons approximately in the middle of the channel (r = 1.5Å). The solid and dotted curves have been obtained representing target electrons by plane waves when the dipole approximation is made and when it is not made, respectively; notice that making use of the dipole approximation leads esentially the same dependence of REC probabilities on photon energy, although the result differs somewhat in magnitude. The dashed curve has been obtained employing coulombic waves; assuming colulombic waves rather than plane waves for the initial states gives somewhat relatively greater REC probabilities for small photon energies, thus the peak energy being slightly smaller, and this effect happens to be more important as capture occurs of electrons closer to the nucleus.

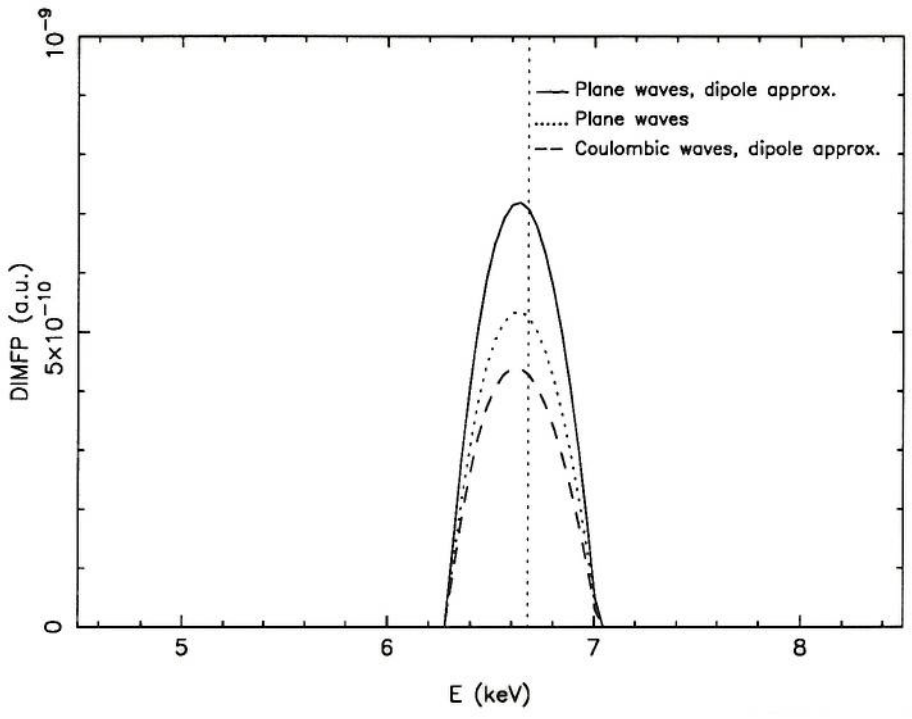


Fig. 4.6. Local DIMFP per unit energy and unit solid angle calculated from eqs. (4.43) (dotted curve), (4.52) (solid curve) and (4.65) (dashed curve), when capture occurs of electrons at 1.5Å from the nearest atom in the crystal; the parameter r_s has been taken to be the local parameter at r = 1.5Å, i.e. r_s = 2.15a.u.. The vertical dotted line refers to the REC energy of eq. (4.33)

It has been found that when capture occurs from electrons closer to the nearest atom in the crystal the DIMFP peak energy deviates sustantially from the REC energy of eq. (4.33); this effect is illustrated in fig. 4.7, where the DIMFP peak energies calculated from eqs. (4.43), (4.52) and (4.65) are plotted against the r distance to the nearest atom, together with the minimum and maximum allowed energies of emitted photons. This deviation is originated in two different ways: on the one hand, the wake correction to the binding energy of the captured electron gets more important as r decreases, and, on the other hand, inner shell electrons are more strongly bound to the solid. These results are favourably related to the experimentally observed REC deficit[16].

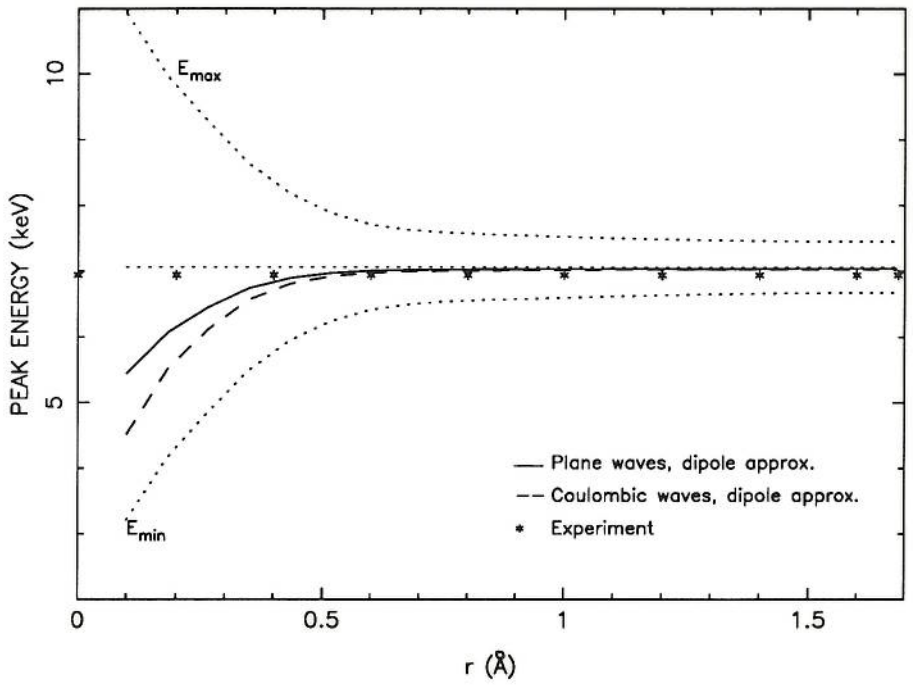


Fig. 4.7. Peak energy positions of the local DIMFP per unit energy and unit solid angle calculated from eqs. (4.52) (solid curve) and (4.65) (dashed curve), as a function of the distance to the nearest atom in the crystal, r_s being the distance dependent local parameter of fig. 4.5. Also shown are the REC energy of eq. (4.33) (dotted horizontal line), the experimental peak energy of ref. 16 (cross points) and the maximum and minimum allowed energies of emitted radiation (dotted curves).

If the wake correction in the binding energy of the captured electron were negligible, the energy distribution of the radiation emitted after capture of Fermi electrons would be centered, neglecting work functions, at the REC energy of eq. (4.33); however, when capture of less

energetic electrons occurs the corresponding energy distribution of the emitted radiation would be no longer centered at the REC energy of eq. (4.33), thus contributing to a deficit of the energy of the emitted radiation, especially at small distances from the nearest atom in the crystal. This effect is slightly enhanced as a result of the fact that emission probabilities get slightly greater as the energy decreases, especially when the initial Coulomb interaction between bombarding ions and target electrons is taken into account.

In order to compare our theoretical results with experiment, we compute the statistical average of the local DIMFP over all possible trajectories of the channeled ion by means of eq. (4.68). Fig. 4.8 exhibits plots of the average DIMFP per unit energy and unit solid angle when the minimum impact parameter is taken to be b_{min} = 0.1Å; the local DIMFPs have been calculated from eqs. (4.43), (4.52) and (4.65), with the distance dependent r_s parameter of fig. 4.5.

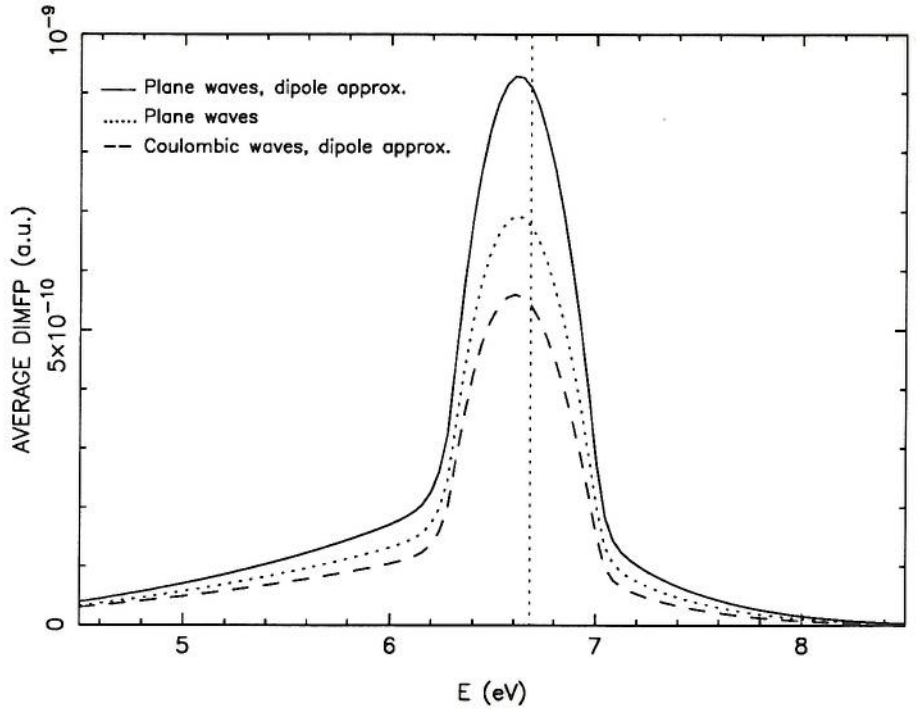


Fig. 4.8. Average DIMFP per unit energy and unit solid angle calculated from eq. (4.68) for b_{min} = 0.1Å and the distance dependent local DIMFP of eqs. (4.43) (dotted curve), (4.52) (solid curve) and (4.65) (dashed curve). The vertical dotted line refers to the REC energy of eq. (4.33), as in figs. 4.2 and 4.6.

Comparing figs. 4.6 and 4.8 one finds that the contribution from capture from inner shells gives rise to a small shift in the peak energy comparable to the experimentally observed

REC deficit. In order to illustrate this, the average DIMFP peak energies deduced from eq. (4.68) are plotted in fig.4.9 versus the energy of the incident ion, together with the REC energies of eq. (4.33) and the experimentally measured peak energies of ref. 16.

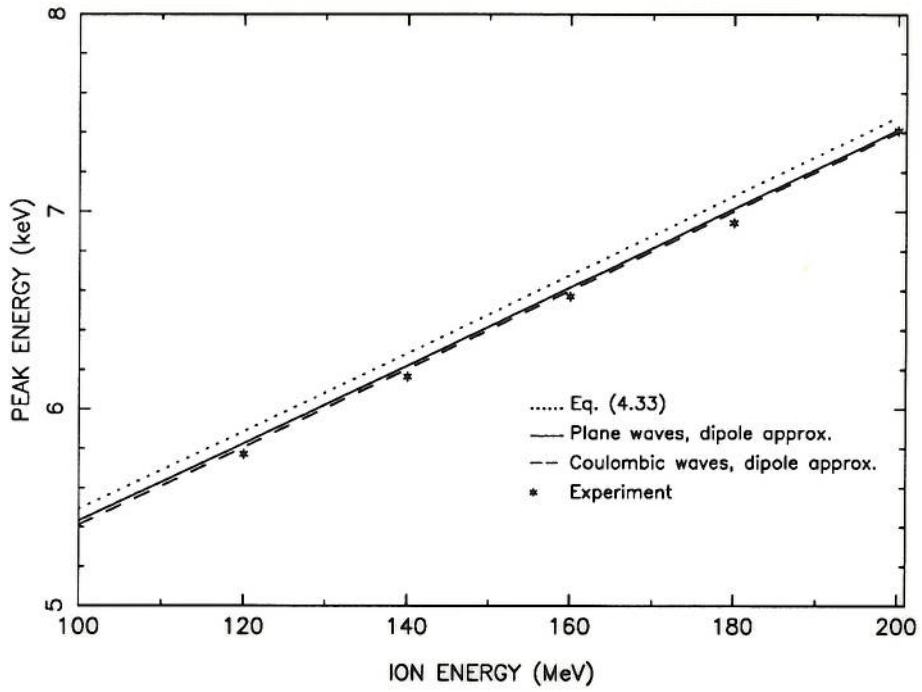


Fig. 4.9. Peak energy positions of the average DIMFP per unit energy and unit solid angle calculated from eq. (4.68), as a function of the energy of bombarding ions, for $b_{\min}$ = 0.1Å and the distance dependent local DIMFP of eqs. (4.52) (solid line) and (4.65) (dashed line). Also shown are the REC energies of eq. (4.33) (dotted line) and the experimentally measured peak energies of ref. 16 (cross points).

It appears from fig. 4.9 that the calculated peak energies are systematically smaller than the REC energies calculated from eq. (4.33) by about 80eV, in approximate agreement with the experimental results. Representing target electrons by coulombic wave functions gives rise to slightly smaller peak energies, as discussed above; this can be due to the fact that in this case the increase in the emission probability as the energy decreases becomes more important. On the other hand, it may be shown that making use of the dipole approximation does not affect appreciably the DIMFP peak energy positions.

The origin of the REC deficit is two-fold, as discussed above. As the impact parameter decreases, thus increasing the total electron density, the wake correction to the binding energy of the captured electron is enhanced, on the one hand, and the target electron momentum

distribution gets wider, on the other hand. These two contributions to the energy deficit are shown, separately, in fig. 4.10, as a function of the energy of projectiles, for $b_{min} = 0.1$Å.

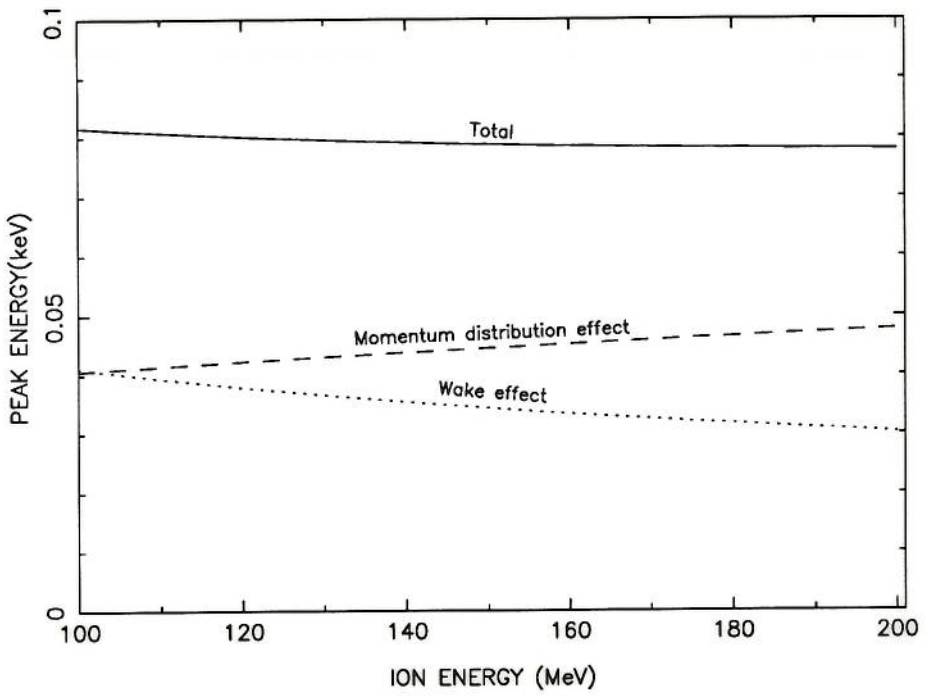


Fig. 4.10. Calculated REC energy deficit, as a function of energy of the bombarding ions (solid line). The dashed curve represents the contribution to the energy deficit from the broadening of the initial momentum distribution, and the dotted line represents the contribution from the wake corrections to the binding energy of the captured electron.

The contribution to the energy deficit from the wake correction to the binding energy of the captured electron gets less important as the velocity of the ion increases, which is obvious from eq. (4.17). The contribution due to the broadening of the mometum distribution does not depend appreciably on the velocity of the ion; however, as a result of Doppler shift corrections REC deficits are slightly enhanced as the ion´s velocity increases.

Full widths at half maximum and differential cross sections

Widths of the average REC distributions described by eq. (4.68) have been found to be larger as the minimum impact parameter decreases, as one might expect. We have calculated,

also, widths of these REC distributions as a function of the incident ion energy and plotted them in fig. 4.11 for different minimum impact parameters, together with the experimental results of ref. 16. The theoretical values are somewhat larger than the experimental ones, but the energy dependences are nearly the same. It is worth mentioning that representing target electrons by coulombic waves rather than plane waves does not affect appreciably tthe results obtained here.

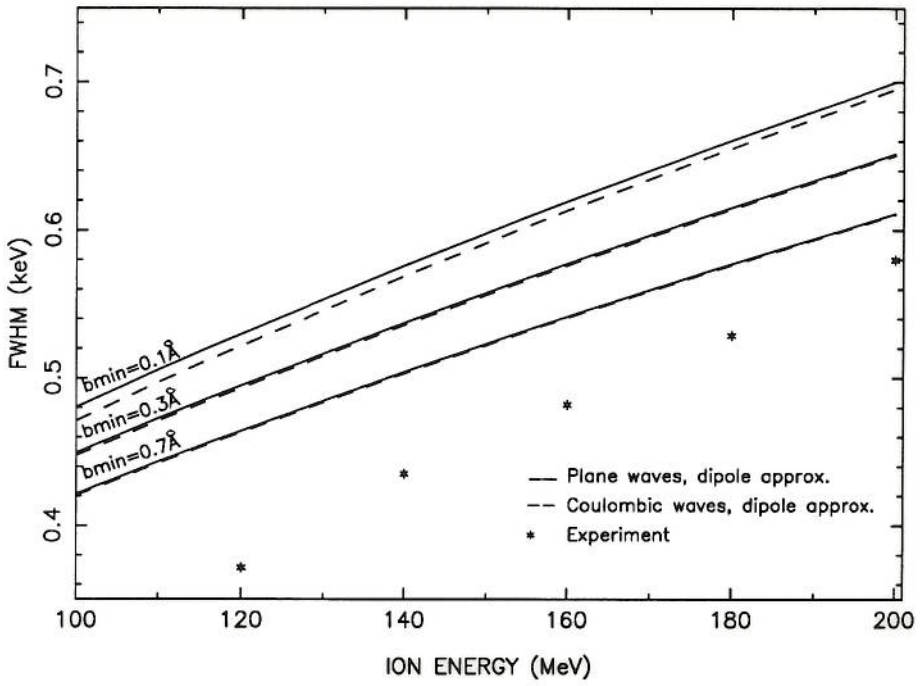


Fig. 4.11. Full widths at half maximum (FWHM) calculated from eq. (4.68), as a function of the incident ion energy, for minimum impact parameters from 0.1 to 0.7Å. The distance dependent local DIMFP has been calculated, as in fig. 4.9, from eqs. (4.52) (solid lines) and (4.65) (dashed lines). Also shown are the experimentally measured FWHM of ref. 16 (cross points).

Finally, we have calculated the REC differential cross sections per unit solid angle and target atom by integrating numerically the average DIMFP of eq. (4.68) over photon energy and dividing by the atomic density of the solid. Fig. 4.12 shows results from Vane et al´s measurements[16] of K-REC yield from bare sulphur ions channeled in silicon, together with our calculated differential cross sections per unit solid angle and target atom. It is obvious from this figure that emission probabilities are enhanced as the energy decreases, as pointed out above; hence, REC spectra are not completely symmetric and the REC peak energies gets

slightly smaller than the REC of eq. (4.33), even when contributions from wake corrections and from capture from inner shells are neglected; however, this effect happens to be almost negligible, though in the range of energies of interest in REC experiments it gets slightly more important when initial coulombic waves are employed.

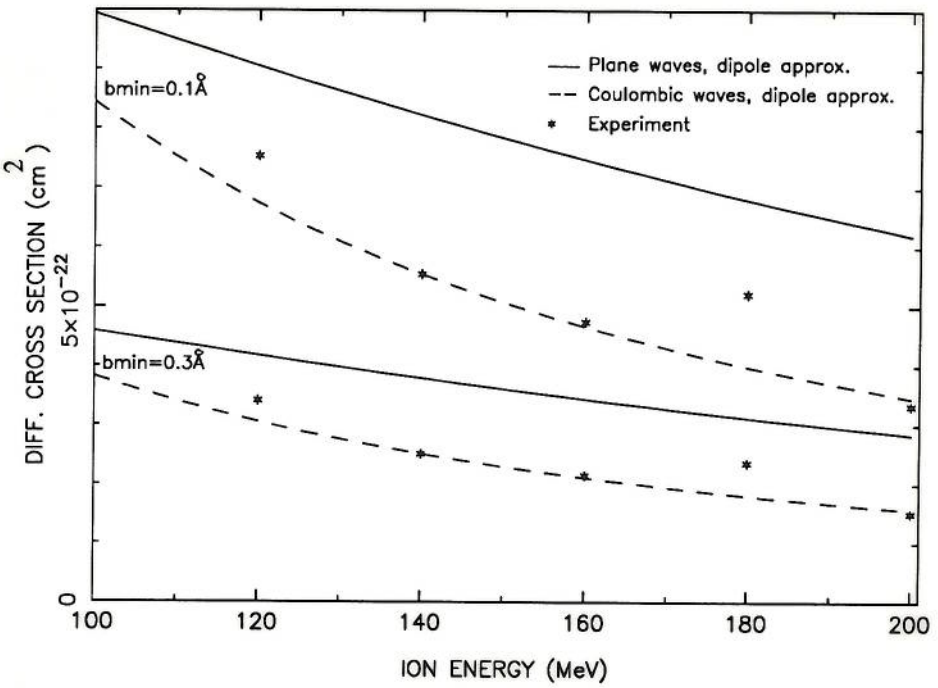


Fig. 4.12. REC differential cross sections per unit solid angle an unit target atom, as a function of incident ion energy, calculated by dividing eq. (4.68) by the atomic density of the target and integrating over photon energy. The distance dependent local DIMFP has been calculated from eqs. (4.52) (solid curves) and (4.65) (dashed curves), as in figs. (4.9) and (4.11). These results are compared with the experimental data of ref. 16 (cross points) normalized at 140MeV.

These differences between differential cross sections found when plane waves and when coulombic waves are used to represent target electrons also exist in the well known total cross sections for recombination given by eqs. (4.59) and (4.67), which are exhibited in fig. 4.13. Although at high energies the cross section can be determined approximately using the Born approximation, that is, assuming that target electrons are initially free, for energies of interest here introduction of the bare Coulomb potential gives rise to a faster decrease of the cross section as the photon energy is increased; this effect is more important for high values of the charge of the ions, but it is not appreciable for high velocities and small charges, as one might

expect.

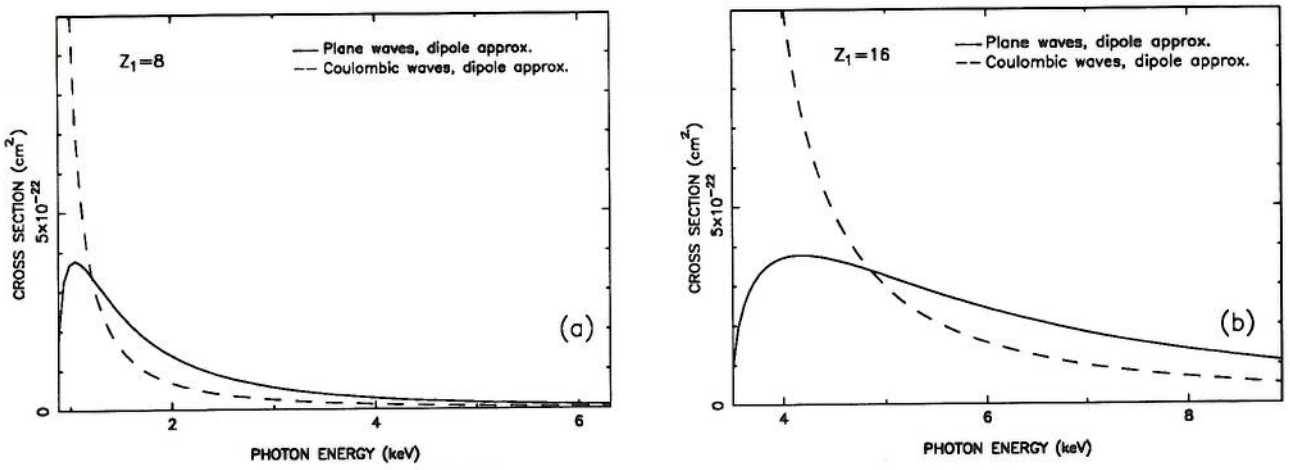


Fig. 4.13. Recombination cross sections calculated from eqs. (4.59) (solid curves) and (4.67) (dashed curves), as a function of emitted photon energy, for $Z_1 = 8$ (fig. 4.13a) and $Z_1 = 16$ (fig. 4.13b)

Appendix: Derivation of eqs. (4.60) and (4.63)

The wave function representing a continuum hydrogenic state of momentum $\boldsymbol{q}$, solution of the time-independent Schrödinger equation through the bare Coulomb potential, may be expanded in partial waves as

$$\varphi_i(\boldsymbol{r}) = \frac{1}{r} \sum_{l=0}^{\infty} C_l(q)\, F_l(q\,,\, r)\, P_l(\cos\,\theta) \quad , \tag{A4.1}$$

where the quantities P_l are the Legendre polynomials, θ being the angle between vectors $\boldsymbol{q}$ and $\boldsymbol{r}$, and the quantities F_l are the regular spherical Coulomb functions, which satisfy the Schrödinger radial equation:

$$F_l(q\,,\, r) = \frac{2^l\, e^{-\pi\gamma/2}\, |\Gamma(l+1+i\,\gamma)|}{(2\,l+1)!} e^{i\,q\,r}\, (q\,r)^{l+1}\, {}_1F_1(l+1+i\,\gamma\,;\, 2\,l+2\,;\, -2\,i\,q\,r) \,. \tag{A4.2}$$

with

$$\gamma = -\,\alpha / q \quad . \tag{A4.3}$$

In these expressions α is given by eq. (4.14) and ${}_1F_1$ is the confluent hypergeometric function, which is solution, regular at the origin, of the Kummer-Laplace differential equation.

Normalizing one finds[28]

$$C_l = \frac{1}{\sqrt{V}}\, q^{-1}\, (2\,l+1)\, i^l\, e^{i\,\delta_l} \quad , \tag{A4.4}$$

where the quantities δ_l are the Coulomb phase shifts

$$\delta_l = \arg\, \Gamma(l+1+i\,\gamma) \quad , \tag{A4.5}$$

and introducing eq. (A4.4) into eq. (A4.1) one obtains eq. (4.60).

Now choosing the z-axis along the direction of $\boldsymbol{q}$ and assuming that the initial and final stationary electronic wave functions are independent of the azimuthal angle, the integral in the right hand of eq. (4.11) can be expressed, in the dipole approximation, as

$$\int d\boldsymbol{r}\, \varphi_f^*(\boldsymbol{r})\, \boldsymbol{\lambda}_k \,.\, \nabla\, \varphi_i(\boldsymbol{r}) = 2\,\pi\,(E_i - E_f)\,(\boldsymbol{\lambda}_k \,.\, \hat{\boldsymbol{q}}) \int_0^{\infty} dr \int_0^{\pi} d\theta\, r^3\, \sin\theta\, \cos\theta\, \varphi_f^*(\boldsymbol{r})\, \varphi_i(\boldsymbol{r}) \,, \tag{A4.6}$$

since one may write[32]

$$<f|\boldsymbol{p}|i> = i\,(E_f - E_i)<f|\boldsymbol{r}|i> \ . \qquad \text{(A4.7)}$$

As the final wave function (4.13) is spherically symetric, only those partial waves of eq. (4.60) which have an angular dependence of the form $\cos\theta$ contribute to the integral of eq. (A4.6). Accordingly, only the part of the initial wave function (4.60) of the target electron which corresponds to $l = 1$ makes a contribution. Thus one finds

$$\int d\boldsymbol{r}\ \varphi_f^*(r)\ \boldsymbol{\lambda}_k \ .\ \nabla\ \varphi_i(r) = 2\,\pi\,(E_i - E_f)\,(\boldsymbol{\lambda}_k \ .\ \hat{\boldsymbol{q}})\,\frac{1}{\sqrt{V}}\,\frac{2\,i\,e^{i\,\delta_1}}{q\,r}\int_0^\infty dr\,r^3\ \varphi_f^*(r)\,F_1(q\ ,\ r)\ . \qquad \text{(A4.8)}$$

Now one may use the following property of gamma functions[33]

$$|\Gamma(l+1+i\,\gamma)| = \sqrt{-\pi\,\gamma}\ e^{\pi\gamma/2}\sqrt{2/\left(1-e^{2\pi\gamma}\right)}\ \prod_{s=1}^{l}\sqrt{s^2+\gamma^2}\ , \qquad \text{(A4.9)}$$

and the following integral representation of the confluent hypergeometric function[34]

$${}_1F_1(a\,;\,b\,;\,z) = \frac{(b-1)!}{2\,\pi i}\int_C d\xi\,(1 - z/\xi)^{-a}\,e^{\xi}\,\xi^{-b}\ , \qquad \text{(A4.10)}$$

where C is a closed path encircling the origin and the point $\xi = z$. After substituting $\xi = 2\,i\,q\,r\,(t + 1/2)$, one finds

$${}_1F_1(l+1+i\,\gamma;\,2\,l+2\,;-2\,i\,q\,r) = \frac{(2\,l+1)!}{2\,\pi i}\,(-2\,i\,q\,r)^{-2\,l-1}\,e^{-i\,q\,r}$$

$$\times\int_C dt\,(t-1/2)^{-i\,\gamma-l-1}\,(t+1/2)^{i\,\gamma-l-1}\,e^{-2\,i\,q\,r\,t}\ . \qquad \text{(A4.11)}$$

Thus introducing expressions (A4.9) and (A4.11) into eq. (A4.2) leads

$$F_1(q\ ,\ r) = \frac{\sqrt{-2\,\pi\,\gamma}}{\sqrt{1-e^{2\pi\gamma}}}\,\frac{\sqrt{1+\gamma^2}}{8\,\pi\,q\,r}\int_C dt\,(t+1/2)^{-i\,\gamma-2}\,(t-1/2)^{i\,\gamma-2}\,e^{2\,i\,q\,r\,t}\ . \qquad \text{(A4.12)}$$

Finally, introducing eq. (A4.12) into eq. (4.60), then eqs. (4.13) and (4.60) into (A4.6), and applying Cauchy´s theorem, we find

$$\int d\boldsymbol{r}\ \varphi_f^*(r)\ \boldsymbol{\lambda}_k \ .\ \nabla\ \varphi_i(r) = \frac{-i}{\sqrt{V}}\,(E_i - E_f)\,(\boldsymbol{\lambda}_k\ .\hat{\boldsymbol{q}})\,(\alpha^3\ \pi)^{1/2}\,\frac{\sqrt{-2\,\pi\,\gamma}}{\sqrt{1-e^{2\pi\gamma}}}\,\frac{2^4\,\gamma\,(1+\gamma^2)^{-5/2}}{q^4}$$

$$\times\left(\frac{-i\,\gamma-1}{-i\,\gamma+1}\right)^{i\,\gamma}\ e^{i\,\delta_l}\ . \qquad \text{(A4.13)}$$

Noticing also that

$$\left(\frac{-i\gamma-1}{-i\gamma+1}\right)^{-i\gamma} = e^{2\gamma\tan^{-1}(-1/\gamma)}\,, \tag{A4.14}$$

introducing eq. (A4.13) into (4.11), and substituting q by q' as defined in eq. (4.62), one finds eq. (4.63).

References

1. H. Betz, *Charge states and charge-changing cross sections of fast heavy ions penetrating through gaseous and solid media*, Rev. Mod. Phys. **44** 465 (1972).
2. R. Shakeshaft & L. Spruch, *Mechamisms for charge transfer (or for capture of any light particle) at asymptotically high impact velocities*, Rev. Mod. Phys. **51** 369 (1979).
3. D. Belkic, R. Gayet & A. Salin, *Electron capture in high-energy ion-atom collisions*, Phys. Rep. **56** 279 (1979).
4. J.S. Briggs & K. Dettman, *Radiative charge transfer from H atoms by fast ions*, Phys. Rev. Lett., **33** 1123 (1974).
5. H.W. Schnopper, H.D. Betz, J.P. Delvaille, K. Kalata, A. R. Sohual, K.W. Jones & M.E. Wesner, *Evidence for radiative electron capture by fast highly stripped heavy ions.* Phys. Rev. Lett. **29** 898 (1972).
6. P. Kienle, M. Klaber, B. Pouh, R.M. Diamond, F.S. Stevens, E. Grosse, M.R. Moier & B. Proctel, *Radiative capture and bremsstrahlung of bound electrons induced by heavy ions,* Phys. Rev. Lett. **31** 1099 (1973).
7. H.W. Schnopper, J.P. Delvaille, K. Kalata, A.R. Solival, M. Abdulwahab, K.W. Jones & H.E. Wegner, *X-ray fast measurements of bremsstrahlung and electron capture by fast positive ions*. Phys. Lett. A **47** 61 (1974).
8. H.W. Shnopper, H.D. Betz & J.P. Delvaille, *Radiative electron capture and bremsstrahlung*, in Atomic Collisions in Solids, edited by S. Datz, B.R. Appleton & C.D. Moak (Plenum, New York, 1975) Vol. II, p. 481.
9. J.E. Miraglia, *Radiative electron capture in proton-hydrogen collision*, Phys. Rev. A. **32** 2702 (1985).
10. B.R. Appleton, T.S. Noggle, C.D. Moak, J.A. Biggerstaff, S. Datz, H.F. Krause, & M.D. Brown, *Radiative electron capture by channeled ions*, see ref. 8, p. 499.
11. B.R. Appleton, R.H. Ritchie, J.A. Biggerstaff, T.S. Noggle, S. Datz, C.D. Moak & H.Verbeek, *Investigations of radiative electron capture by ion channeling techniques*, J. Nucl. Mater. **63** 513 (1976).

12. B.R. Appleton, R.H. Ritchie, J.A. Biggerstaff, T.S. Noggle, S. Datz, C.D. Moak, H. Verbeek, & V.N. Neelavathi, *Radiative electron capture by oxygen ions in single-crystal channels: Experiment and theory*, Phys. Rev. B **19** 4347 (1979).

13. M.T. Robinson & O.S. Oen, Appl. Phys. Lett. **2** 30 (1963).

14. J.K. Lindhard, K. Dans. Vidensk. Selsk. Mat.-fys. Medd. **34** no.14 (1965). See also D.S. Gemmell, *Channeling and related effects in the motion of charged particles through crystals*, Rev. Mod. Phys. **46** 129 (1974).

15. Andriamonje S., Chevallier M., Cohen C., Dural J., Gaillard M.J., Genre R., Hage Ali M., Kirsch R., L'Hoir A., Mazuy B., Mory J., Moulin J., Poizat J.C., Remillieux J., Schamaus D. & Toulemonde M., *Observation of radiative electron capture into K,L,M shells of 25-MeV/u Xe^{53+} ions channeled in silicon*, Phys. Rev. Lett. **59** 2271 (1987).

16. C.R. Vane, S. Datz, P. Dittner, J. Giese, J. Gómez del campo, N.Jones, H. Krause, P.D. Miker, H. Schone & M. Schulz, *Radiative electron capture* , Proceedings of the 11th Werner Brandt Workshop on Penetration Phenomena of Charged Particles in Matter, Oak Ridge, Tennessee, April 14-15, 1988.

17. J.E. Miraglia, R. Gayet & A. Salin, *Radiative electron capture by ions channeled in crystals*, Europhys. Lett. **6** 397 (1988).

18. J.M. Pitarke & R.H. Ritchie, *Radiative electron capture by channeled ions*, Proceeding of the 12th Werner Brandt Workshop on Penetration Phenomena of Charges Particles in Matter, Donostia, Basque Country, September 4-7 (1989).

19. J.M. Pitarke, R.H. Ritchie & P.M. Echenique, *Radiative electron capture by channeled ions* (accepted for publication in Phys. Rev. B).

20. R. Shakeshaft & L. Spruch, *Radiative capture and galilean invariance*, Phys. Rev. Lett. **38** 175 (1977).

21. P.A.M. Dirac, *The Principles of Quantum Mechanics* (Clarendon, Oxford, 4th edition), chapter 10.

22. J. C. Inkson, *Many-body theory of solids: An introduction*, (Plenium Press, New York and London, 1984), p. 81.

23. L.I. Shiff, *Quantum Mechanics* (Mc Graw-Hill, New York, 1968), chapter 4.

24. R.H. Ritchie, W. Brandt & P.M. Echenique,*Wake potential of swift ions in solids*, Phys. Rev. B **14** 4808 (1976).

25. P.M. Echenique, R.H. Ritchie & W. Brandt, *Spatial excitation patterns induced by swift ions in condensed matter*, Phys. Rev. B **20** 2567 (1979).

26. L.D. Landau & E.M. Lifshitz. *Course of Theoretical Physics*: *Quantum Electrodynamics* (Pergamon Press, 1982) Vol. 4, p. 165.

27. M. Abramonitz & I.A. Stegun, *Handbook of Mathematical Functions* (Dover, New York, 1965).

28. C.J. Joachain, *Quantum collision theory* (North-Holland publishing company, Amsterdam, Oxfordd, 1975), chapter 6.

29. H.A. Bethe & E.E. Salpeter, *Quantum Mechanics of one-and two-electron atoms* (Academic, New York, 1957), p. 322.

30. See 26, p. 211.

31. T.C. Tucker, L.D. Roberts, C. W. Nestor, T.A. Carlson & F.B. Malik, R*elativistic self-consistent-field calculation of the wave functions, eigenvalnes, isotope shifts, and the 6s Hyperfine-structure coupling constants as a function of pressure for metallic gold in the Wigner-Seitz Model,* Phys. Rev. **178** 998 (1965). We are grateful to Dr. C.W. Nestor for furnishing the data to us.

32. See 23, p. 404.

33. L.D. Landau & E.M. Lifshitz. *Course of Theoretical Physics: Quantum Mechanics*, (Pergamon Press, 1982) Vol. 3, p. 122.

34. N.F. Mott & H.S.W. Massey, *The theory of atomic collisions* (3rd edition, Oxford University, London, 1965), p. 58. See also 33, p. 657.

5. SUMMARY AND CONCLUSIONS

In this thesis some aspects of the interaction of charged particles with electrons in solids have been investigated.

1. In chapter 2, first of all the constant current mode distance-voltage, s–V_a, and conductance-voltage, dI/dV_a–V_a, tunneling characteristics experimentally measured by other workers with the Scanning Tunneling Microscope (STM) have been calculated theoretically, and an interpretation of the experimental results has been provided. A new one-dimensional model potential barrier which takes into account both local and non-local exchange and correlation effects and dynamic effects has been presented and studied in detail, and it has been shown that a reasonable fit to the interface potential can be made using this parametrized model potential, by a trial and error process to reproduce the experimentally determined tunneling characteristics, as a result of the resonance phenomena appearing in the field emission regime. Then a three-dimensional model has been presented, assuming a spherical tip and planar sample; the importance of taking into account the 3D tip-sample geometry, especially at high applied voltage ($V_a > 10$V), has been demonstrated, and it has been found that reproducing the experimentally measured tunneling characteristics allows the tip radius to be determined.

2. Also in chapter 2, an analysis of the apparent barrier height in STM, defined in terms of the rate of change of the logarithm of current or bias voltage with tip-sample separation, has been made. With this purpose, first of all the mean barrier approximation in calculating the tunneling current density, which is valid for large interelectrode separations ($s > 10$Å), has been considered and analytical expressions for the apparent barrier height have been derived for different model potentials. The existent controversy on the contribution of the image potential to measurements of the apparent barrier height has been clarified, and it has been demonstrated that the role that the image potential plays in lowering the apparent barrier height is important, even though it is over a long range of tip-sample separations approximately equal to the average work function. In order to illustrate the discussion made for large separations and extend it to smaller separations, exact calculations of the apparent barrier height have been made solving the Schrödinger equation for different model potentials and integrating over all

allowed energies; it has been found that the apparent barrier height calculated with the parametrized potential model proposed in the preceding sections is for short tip-sample separations in good agreement with previous calculations made by Lang not including non-local image effects, and it has been found, also, that at larger separations our potential yields the appropriate apparent barrier height associated with image effects.

3. In chapter 3, a theoretical analysis of the dependence of the yield of knock-on electrons emitted under bombardment of diatomic molecular ions on the orientation of bombarding diclusters has been presented, together with linear-response theory calculations of the electron density fluctuations induced at the position of the trailing ion by the leading ion of the bombarding dicluster. Differential scattering cross sections of knock-on electrons emitted at 0° with respect to the beam direction have been calculated, and it has been found that the dependence of electron emission on the orientation of the diclusters presents oscillations depending on the velocity and interatomic distance of the projectiles, and that the electron yield decreases as the bombarding diclusters get longitudinally aligned with respect to the beam direction, as a consequence of multiple scattering effects. First of all multiple scattering effects have been approximated within the second Born approximation, and it has been found that the exact scattering amplitude of electrons in the potential of a single ion must be considered for the charges and velocities of interest here; secondly, scattering theory has been combined with methods developed in the theory of low energy electron difraction (LEED), and it has been shown that this may become a useful method for low velocities of the projectiles(v < 2.5a.u.). The available experimental data have been obtained for rather large effective charges and intermediate velocities (v = 2.5a.u.); it has been shown that new experiments performed for different charges and velocities would be very useful in order to investigate the applicability of linear theories and capture and loss theories, and also to detect the effect of electron density fluctuations.

4. In chapter 4, the impact parameter dependence of radiative electron capture (REC) by channeled ions in solids has been investigated, including the effect of the ion´s wake and